



저작자표시-비영리-변경금지 2.0 대한민국

이용자는 아래의 조건을 따르는 경우에 한하여 자유롭게

- 이 저작물을 복제, 배포, 전송, 전시, 공연 및 방송할 수 있습니다.

다음과 같은 조건을 따라야 합니다:



저작자표시. 귀하는 원저작자를 표시하여야 합니다.



비영리. 귀하는 이 저작물을 영리 목적으로 이용할 수 없습니다.



변경금지. 귀하는 이 저작물을 개작, 변형 또는 가공할 수 없습니다.

- 귀하는, 이 저작물의 재이용이나 배포의 경우, 이 저작물에 적용된 이용허락조건을 명확하게 나타내어야 합니다.
- 저작권자로부터 별도의 허가를 받으면 이러한 조건들은 적용되지 않습니다.

저작권법에 따른 이용자의 권리는 위의 내용에 의하여 영향을 받지 않습니다.

이것은 [이용허락규약\(Legal Code\)](#)을 이해하기 쉽게 요약한 것입니다.

[Disclaimer](#)

Ph.D THESIS

**Strengthening and corrosion control of
pure magnesium and WE43 magnesium
alloy for biomedical applications**

Mathilde Diez

SEOUL NATIONAL UNIVERSITY
Department of Materials Science and Engineering

July 2015

Strengthening and corrosion control of pure magnesium and WE43 magnesium alloy for biomedical applications

Mathilde Diez

SEOUL NATIONAL UNIVERSITY

This thesis was certified and approved by the following committee members:

Signature

Seong Hyeon Hong

Professor at Seoul National University, Materials Science and Engineering
Chair of the committee

Hyun Ee Kim

Professor at Seoul National University, Materials Science and Engineering
Thesis Supervisor

Heung Nam Han

Professor at Seoul National University, Materials Science and Engineering

Young Hag Koh

Professor at Korea University, School of dentistry
External committee member

Jeong Ho Lee

Professor at Seoul National University, School of dentistry
External committee member

ABSTRACT

Strengthening and corrosion control of pure magnesium and WE43 magnesium alloy for biomedical applications

by Mathilde Diez

Department of Materials Science and Engineering

SEOUL NATIONAL UNIVERSITY

For the last decade magnesium and its alloys have received more and more attention as candidate materials for biomedical applications owing to their advantages over other metallic materials, especially with regard to their biocompatibility, biodegradability and low density. However these benefits are not matched by their high corrosion rate and low mechanical performance, which is an obvious obstacle to their use in biomedical applications.

In this thesis a thermo-mechanical treatment using a deformation process referred to as three-roll planetary milling (PSW) is proposed to improve the strength of magnesium implants. Compared to the well known equal channel angular pressing (ECAP) process this technique would be suitable for the fabrication of implants in industry scale production without promoting softening effect. An ageing treatment was combined with the PSW process to induce hardening precipitation and strengthen more magnesium. The corrosion rate of magnesium, and therefore its degradation rate, was controlled by coating its surface with a hydroxyapatite (HA) poly-L-lactid acid (PLLA) ceramic polymer composite. Although HA is known to have very good bioactivity due to its similar composition with that of the bone, its brittle behaviour reduces considerably its performance under strain. Therefore a flexible PLLA layer was coated in addition of HA to provide stability and strain resistance.

In the first study, PSW technique was used to trial its potential for enhancing the mechanical properties of magnesium. Pure magnesium was processed via this technique with a first pass conducted at 250°C and followed by 10 others passes with a scaling down of temperature to finally reach room temperature. A total true strain of 96% was obtained and it was shown that pure magnesium reached excellent yield strength of 146 MPa, comparable with the strength levels of magnesium alloys and with that of the cortical bone, allowing therefore its use for bone graft applications. A homogenization of the grain refinement through the sample was also found after 6 passes with a grain size of 5-6 microns, favorable to strengthen the material, together with a change of texture.

In the second study the attention was focused on a magnesium alloy, namely WE43 (4% Yttrium 3% Neodymium), which is believed to be suitable for biomedical applications owing to its good corrosion resistance and non-toxicity. The alloy was first solution treated at 525°C for 5h, subsequently deformed at 400°C (1 pass) using the PSW process and water quenched. It was then aged at 210°C for 16h. Although no significant grain refinement occurred in the rod sample after one pass of roll milling, a strength improvement was observed, more pronounced at the rim area of the billet, with maximum strength values of about 220 MPa, owing to the development of (110) texture. Further number of passes did not promote strengthening of the material. The formation of β' phase precipitates during the first period of ageing resulted in another increase of strength up to 300 MPa. However, a loss of mechanical properties was observed after a long ageing period (≥ 16 h) associated with a grain growth and the formation of β phase precipitates.

The third study aimed at fabricating a biocompatible and strain resistant coating for WE43 substrate in order to control its corrosion rate. After a first pre-treatment consisting in annealing the material at 525°C for 5h to reduce the second phase particles size and obtain a homogeneous microstructure for further treatment, HA was coated on WE43 by immersion in an aqueous solution containing calcium and phosphate sources. A 3 μ m thick layer of needle like shape HA crystals was uniformly formed on the substrate. PLLA layer was then deposited onto HA by dip coating technique using vacuum system. In order to mimic real cases and possible deformation during implantation, a 5% tensile strain was applied to the coated WE43 alloy. Compared with single HA coating and PLLA coating, dual HA-PLLA coating showed good stability and reduced remarkably the corrosion rate of WE43 tested under strain with no cracks formation or delamination, resulting in a constant pH value of simulated body fluid (SBF). After 10 days immersion into SBF, a good strength of 140 MPa was maintained in the stretched coated magnesium, almost the double than the one of WE43 without coating. Moreover the biological response, including cell attachment, proliferation and differentiation, of the composite coated alloy was enhanced and was found to be the best among all the compared samples. These results confirmed that HA-PLLA coated magnesium is a promising material for biomedical implant applications.

Keywords: magnesium, WE43, three roll planetary milling, mechanical properties, hydroxyapatite, poly-L-lactid acid, corrosion, biocompatibility.

Student number: 2012-30724

Contents

Strengthening and corrosion control	i
Abstract	ii
Acknowledgements	iv
List of Figures	viii
List of Tables	xii
Abbreviations	xiii
1 Introduction	1
1.1 Context	1
1.2 General framework for using magnesium as a biodegradable implant and statement of the problems	2
1.3 Outline of the thesis	3
2 Theoretical review	5
2.1 Magnesium as a structural implant substrate	5
2.1.1 Advantages of using magnesium as an implant substrate	5
2.1.2 Mechanical properties of magnesium	6
2.2 Deformation of hexagonal close packed structure and strengthening mechanisms	9
2.2.1 Crystal structure of hexagonal close-packed of magnesium	9
2.2.2 Strengthening of materials by SPD techniques	10
2.2.3 Precipitation hardening	13
2.3 Corrosion of magnesium and surface modification of implants	14
2.3.1 Corrosion mechanisms of magnesium and its alloys and consequences for the implant surrounding tissues	16
2.3.2 Corrosion behaviour of SPD processed magnesium	17
2.3.3 Coating of magnesium and its alloys	18
2.3.3.1 Calcium Phosphate based coating	19
2.3.3.2 Polymer coating	20
2.4 Conclusion	22
3 Improving the mechanical properties of pure magnesium by three roll planetary milling	23
3.1 Introduction	23
3.2 Methods	24
3.3 Results	26
3.3.1 Homogenization and microstructure analysis	26

3.3.2	Mechanical properties	30
3.3.3	Texture	33
3.4	Conclusion	36
4	Thermo-mechanical treatment of WE43 magnesium alloy to reach high strength for biomedical applications	38
4.1	Introduction	38
4.2	Methods	39
4.3	Results	41
4.3.1	Initial cast Mg-Y-Nd alloy	41
4.3.2	Mechanical properties	42
4.3.3	Influence of the number of passes	43
4.3.4	Microstructure evolution	46
4.3.4.1	Grain size evolution	46
4.3.4.2	Optical images	47
4.3.4.3	EBSD images	48
4.3.5	Texture	49
4.3.6	Ageing time and hardening precipitation	52
4.3.6.1	TEM observations	52
4.3.6.2	Microhardness measurement as a function of ageing time	54
4.3.7	Corrosion behaviour after thermo-mechanical treatment	57
4.4	Results and discussion	59
4.4.1	Microstructure, texture and improved mechanical properties	59
4.4.2	Increase of the number of passes of screw rolling and modification of the ageing time	60
4.4.3	Comparison of thermo-mechanical treated WE43 alloy with only thermal treated WE43 alloy	60
4.4.4	Corrosion of the processed WE43 magnesium alloy	61
4.5	Conclusion	62
5	Behaviour of dual HA-PLLA coated WE43 magnesium alloy under strain	63
5.1	Introduction	63
5.2	Methods	64
5.3	Results	67
5.3.1	Composition and adhesion strength of HA coating	67
5.3.2	Morphology of the composite coating	68
5.3.3	Coating morphologies after application of strain	71
5.3.4	Electrochemical response and potentiodynamic polarization curves	72
5.3.5	In vitro corrosion test	73
5.3.5.1	pH evolution	73
5.3.5.2	Hydrogen H ₂ gas release	74
5.3.5.3	Mg ions concentration	75
5.3.5.4	Surface morphology after 10 days into SBF	77
5.3.6	Mechanical stability	78
5.3.7	In-vitro cell responses	81
5.3.7.1	Cell attachment observed by optical microscope	81
5.3.7.2	Cell attachment observed by con-focal microscope	81
5.3.7.3	Cell proliferation	83
5.4	Discussion	83
5.5	Conclusion	87
6	Conclusion and future work	88
6.1	Conclusion	88

6.2	Future work	90
A	Complete ODF data obtained in chapter 3	92
A.1	As received pure magnesium	92
A.2	Processed pure magnesium after 1 pass of PSW	93
A.3	Processed pure magnesium after 6 passes of PSW	94
A.4	Processed pure magnesium after 11 passes of PSW	95
B	Theoretical diffraction pattern representation of magnesium	96
C	Complete ODF data obtained in chapter 4	98
	Bibliography	101

List of Figures

2.1	Schematic drawing of biodegradation process of an implant after its implantation into the body.	6
2.2	(a) Ultimate tensile strength of pure magnesium after 2, 4, 6, 8 and 12 weeks of implantation in rabbit tibial shafts (b) Optical pictures of the same pure magnesium specimens after 2, 4, 6, 8 and 12 weeks of implantation (c) Reconstructed μ CT-image of pure magnesium screw specimens after 6 weeks and (d) 12 weeks of implantation. Cited from [1].	8
2.3	Theoretically possible slip modes in magnesium ; colored surfaces represent each slip planes, arrows represent slip direction Burgers vectors (a) $\langle a \rangle$ type slip system (b) $\langle a + c \rangle$ type slip system [2].	10
2.4	(a) schematic of ECAP technique (b) grain refinement observed in the microstructure of pure magnesium in the extruded state and after 6 ECAP passes (c) (0002) and (10 $\bar{1}$ 0) pole figures of as extruded magnesium and ECAPed magnesium (d) strain-stress curves of as extruded magnesium and after 1, 2 and 6 ECAP passes. Cited from [3].	12
2.5	Vickers hardness for different temperatures as a function of ageing time [4].	14
2.6	TEM results obtained along the $\langle 0001 \rangle$ zone axis of (a) BF of sample aged at 150°C for 12 days (b) corresponding SADP (c) BF of sample aged at 210°C for 1 day (d) corresponding SADP (e) BF of sample aged at 210°C for 3 days (f) corresponding SADP (g) BF of sample aged at 210°C for 7 days (h) corresponding SADP (i) BF of sample aged at 250°C for 4 hours (j) corresponding SADP.	15
3.1	Schematic of the three roll planetary milling process (PSW) and the arrangement of the rollers.	24
3.2	Microstructure of the pure magnesium rod (a) in the as-received condition and after (b) 1 pass (250°C), (c) 6 passes (150°C), and (d) 11 passes of PSW (RT), taken at half the distance between the center and the rim.	26
3.3	(a), (b) TEM micrographs of pure Mg structure after 11 passes of PSW taken at two different locations of the billet	27
3.4	Grain size distribution along the diameter of the billet after 1, 6 and 11 passes of PSW.	27
3.5	The microhardness distribution versus the distance from the center of the specimens processed by PSW after one, three and six passes.	28
3.6	Color-coded contour maps showing the distribution of microhardness over the cross section of PSW-processed copper rods after (a) one, (b) three, and (c) six passes at room temperature. The color code shown in (c) corresponds to the microhardness levels of the rods.	30
3.7	Tensile stress-strain curves of pure magnesium in the as-received (AR) condition and after 1 (P1), 6 (P6) and 11 (P11) passes of PSW.	31
3.8	Summary of the values of the yield strength and strain to failure from tensile curves for as-received (AR) magnesium and after different numbers of PSW passes.	31
3.9	The Hall-Petch plot for Mg combining the $\sigma_{0.2}$ proof stress data for the as-received and the screw rolling processed samples.	32

3.10	The X-ray pole figures $\{00.4\}$, $\{10.0\}$, $\{10.1\}$, $\{10.2\}$, $\{10.3\}$ and $\{11.0\}$ of pure magnesium (a) in the as received condition and after (b) 1 pass (c) 6 passes and (d) 11 passes of screw rolling.	34
3.11	ODF sections for $\varphi_2=40^\circ$ of pure magnesium (a) in the as received condition and after (b) 1 pass (c) 6 passes and (d) 11 passes of screw rolling. (e) Schematic of the XRD technique with Euler angles convention used here. (f) Theoretical texture diagram for $\varphi_2=45^\circ$ was used to identify the obtained texture.	35
3.12	Stress strain curves of the cortical and trabecular bone as well as of pure magnesium acquired after 6 and 11 passes.	37
4.1	Schematic illustration of the experimental procedure used in this study.	40
4.2	Microstructure of the cast WE43 (a) at low magnification and (b) at high magnification using SEM technique to clearly reveal the second phase particles.	42
4.3	X-rays diffraction pattern of the cast WE43 and the phases associated with the peaks.	42
4.4	True stress-strain curves for magnesium WE43 alloy in the cast condition and after each step of the thermo-mechanical treatment. The scatter area refers to the non homogeneity of the samples.	44
4.5	Vickers hardness distribution versus the distance from the center of the cast, ST, ST PSW400°C and ST PSW400°C Aged WE43 specimens.	44
4.6	Modified version of the previous experimental procedure. In this section WE43 alloy was subjected to three passes of PSW process and aged in order to determine how far the strength of the material can be driven.	45
4.7	Tensile strain stress curves of WE43 magnesium alloy after 1, 2 and 3 passes of PSW at 400°C (a) without and (b) with subsequent ageing treatment at 210°C for 16h.	45
4.8	Hardness distribution in WE43 magnesium alloy after 1, 2 and 3 passes of PSW at 400°C (a) without and (b) with subsequent ageing treatment at 210°C for 16 hours.	46
4.9	Grain size evolution versus the distance from the center of the ST, ST PSW400°C and ST PSW400°C Aged WE43 specimens	47
4.10	Optical images of the microstructure of WE43 magnesium alloy after annealing, 1 pass of PSW and ageing taken at different location over the cross section area of the sample (a) in the central region (b) at half radius (c) at the periphery of the sample	48
4.11	(a) Microstructure, (b) EBSD map showing the boundaries distribution and (c) EBSD map showing the texture components of WE43 magnesium alloy after annealing and one pass of screw rolling (ST PSW400°C). The color-coded key as well as the sample geometry are indicated in (d). The boundaries distribution and texture components of WE43 alloy after ageing (ST PSW400°C Aged) are illustrated in (e) and (f), respectively.	50
4.12	XRD pattern for, from bottom to top, the WE43 alloy in the cast condition, after solution treatment at 525°C for 5 hours, after one pass of screw processing at 400°C and after ageing at 210° for 16 hours	51
4.13	ODF sections for $\varphi_2=50^\circ$ of (a) cast WE43, (b) solution treated, (c) Solution treated and processed by PSW at 400°C and (d) processed and aged WE43. The Euler convention used here was the same than in figure 3.11	52
4.14	TEM bright field images and corresponding selected area diffraction pattern (SADP) of processed WE43 alloy after (a) 16 hours ageing (zone axis $[01-10]$), (b) 3 days ageing (zone axis $[01-10]$) and (c) 7 days ageing (zone axis $[1-21-3]$).	55
4.15	Hardness evolution over the cross section of WE43 Mg samples after 0h, 2h, 16h and 7 days ageing (a) with and (b) without plastic deformation.	56

4.16	Vickers hardness as a function of ageing time for solution treated, processed and aged samples (ST PSW400°C Aged) and solution treated and aged samples (ST Aged) subjected to ageing at 210°C. As a way of comparison data from the literature of a WE43 alloy subjected to a solution treatment at 525°C for 8h followed by quenching and ageing at 210°C for different period of time (same conditions than our study) [4] were also added in the figure.	57
4.17	pH variation as a function of immersion time in SBF of extrude pure magnesium, cast WE43 and PSW-processed WE43.	58
4.18	Sample polarization curves for cast WE43, PSW-processed and aged WE43 and extruded pure magnesium in SBF solution.	59
4.19	True stress-strain curves for WE43 magnesium alloy in the cast conditions, after PSW processing and ageing, and after ageing.	61
5.1	(a) Experimental procedure of the two steps WE43 strain resistant coating. First HA was formed by conversion technique then PLLA was deposited by deposition technique. As it can be seen all sizes and shapes of specimens can be coated by this simple technique. (b) In this study four different specimens were studied. . .	66
5.2	Characterization of the different properties of the HA coating layer. (a) XRD diffraction patterns of calcium-phosphate coated WE43 Mg alloy before (bottom) and after (top) conversion treatment. (b) FE-SEM image of the HA coating layer formed on WE43 Mg alloy after conversion treatment for 2h, in a solution of a pH of 9.3. (c) Adhesion test curve performed on HA coated WE43. (d) Literature data [1, 5] juxtaposed with our result of adhesion strength.	68
5.3	SEM images of (a) the microstructure of WE43 magnesium alloy in the cast conditions, (b) after annealing at 525°C for 5h, (c) HA coated WE43, (d) PLLA coated WE43 and (e) dual HA-PLLA coated WE43.	69
5.4	Cross section views taken by FIB of the (a) HA coated WE43, (b) PLLA coated WE43 and (c) dual HA-PLLA coated WE43. (d) FE-SEM image of scraped-off dual HA-PLLA coating showing the good adhesion between HA and PLLA. . . .	70
5.5	SEM images of (a) polished cast WE43, (b) HA coated WE43, (c) PLLA coated WE43 and (d) dual HA-PLLA coated WE43 after application of 5% strain. . . .	71
5.6	Polarization curves for cast WE43, HA coated WE43, PLLA coated WE43 and HA-PLLA coated WE43 subjected to 5% strain, obtained in SBF solution with a pH of 7.4.	72
5.7	pH evolution as a function of immersion time in SBF of cast WE43, HA coated WE43, PLLA coated WE43 and HA-PLLA coated WE43 in the case of (a) before deformation and (b) after application of 5% tensile strain deformation.	74
5.8	Hydrogen gas evolution during immersion into SBF of cast WE43, HA coated WE43, PLLA coated WE43 and HA-PLLA coated WE43 (a) before deformation and (b) after application of 5% tensile strain deformation.	76
5.9	Magnesium ions concentration in SBF solution as a function of immersion time of cast WE43, HA coated WE43, PLLA coated WE43 and HA-PLLA coated WE43 in the case of (a) 0% tensile strain and (b) 5% tensile strain.	77
5.10	SEM images showing the surface morphology of (a) cast WE43, (b) HA coated WE43 at high magnification and (c) low magnification, (d) PLLA coated WE43 and (e) dual HA-PLLA coated WE43 at low magnification and (f) high magnification, after deformation and 10 days immersion into SBF.	79
5.11	Tensile toughness measured after 10 days immersion into SBF of cast WE43, HA coated WE43, PLLA coated WE43 and dual HA-PLLA coated WE43, before and after application of 5% strain deformation.	80
5.12	Tensile strength measured after 10 days immersion into SBF of cast WE43, HA coated WE43, PLLA coated WE43 and dual HA-PLLA coated WE43, before and after application of 5% strain deformation.	80

5.13	SEM images of the MC3T3 osteoblast cells that were cultured for 2 days on (a) cast WE43, (b) 5% strained cast WE43, (c) HA coated WE43, (d) 5% strained HA coated WE43, (e) PLLA coated WE43, (f) 5% strained PLLA coated WE43, (g) HA-PLLA coated WE43 and (h) 5% strained HA-PLLA coated WE43. . . .	82
5.14	CLSM images of the MC3T3 osteoblast cells that were cultured for 3 days on 5%strained (a) cast WE43, (b) HA coated WE43, (c) PLLA coated WE43 and (d) HA-PLLA coated WE43. High magnification of the filopodia in the case of PLLA coated WE43 and HA-PLLA coated WE43 can be seen in (e) and (f), respectively.	84
5.15	DNA levels of the MC3T3 osteoblast cells that were cultured for 3 days on the cast WE43, HA coated WE43, PLLA coated WE43 and HA-PLLA coated WE43 specimens, after and before application of 5% strain.	85
5.16	Cross section of HA-PLLA coated WE43 subjected to 5% strain (before immersion) when (a) PLLA acts as a protective layer, (b) when a crack propagation occurs from HA layer to PLLA layer. After immersion in SBF for several days, (c) the crack in PLLA has opened up and the damaged HA layer was exposed to the medium.	86
A.1	ODF sections of pure magnesium in the as received conditions for $\varphi_2=0^\circ$ to $\varphi_2=60^\circ$	92
A.2	ODF sections of pure magnesium after 1 pass of PSW for $\varphi_2=0^\circ$ to $\varphi_2=60^\circ$	93
A.3	ODF sections of pure magnesium after 6 passes of PSW for $\varphi_2=0^\circ$ to $\varphi_2=60^\circ$	94
A.4	ODF sections of pure magnesium after 11 passes of PSW for $\varphi_2=0^\circ$ to $\varphi_2=60^\circ$	95
C.1	ODF sections of cast WE43 magnesium alloy for $\varphi_1=0^\circ$ to $\varphi_1=90^\circ$	98
C.2	ODF sections of WE43 magnesium alloy after annealing at 525°C for 5h, for $\varphi_1=0^\circ$ to $\varphi_1=90^\circ$	99
C.3	ODF sections of WE43 magnesium alloy after 1 pass of PSW, for $\varphi_1=0^\circ$ to $\varphi_1=90^\circ$	99
C.4	ODF sections of WE43 magnesium alloy after processing and ageing treatment at 210°C for 16 hours, for $\varphi_1=0^\circ$ to $\varphi_1=90^\circ$	100

List of Tables

2.1	Summary of the physical and mechanical properties of various implant materials in comparison with natural bone [6–8].	7
2.2	Slip planes and directions of the different dislocation types in HCP crystals [9].	10
3.1	Summary of work on improving the mechanical properties of pure Mg by SPD processing.	32
3.2	The orientation factors for the different deformation systems in pure magnesium investigated.	34
3.3	Summary of results in terms of texture, average grain size, yield strength and tensile elongation of magnesium in the as received (AR) condition and after 1, 6 and 11 passes of three-roll planetary milling.	36
4.1	EDS results of as cast WE43 alloy of figure 4.2.	42
4.2	Details about precipitates in Mg-Y-Nd alloys	53
A.1	Summary of the ODF angles of processed pure magnesium after 1 pass of PSW.	93
A.2	Summary of the ODF angles of processed pure magnesium after 6 passes of PSW.	94
A.3	Summary of the ODF angles of processed pure magnesium after 11 passes of PSW.	95

Abbreviations

E	Elastic modulus (Young's modulus)
EBSD	Electron B ack S catter D iffraction
ECAP	Equal Channel Angular P ressing
FESEM	Field E mission S canning E lectron M icroscopy
FIB	Focused I on B eam
HA	Hydroxy- A patite
HAGB	High A nge G rain B oundary
HCP	Hexagonal C lose P acking
LAGB	Low A nge G rain B oundary
ODF	Orientation D istribution F unction
PCL	Poly C apro L actone
PGA	Poly- G lycolic A cid
PLA	Poly- L actic A cid
PLLA	Poly- L - L actid A cid
SADP	Selected A rea D iffraction P attern
SEM	Scanning E lectron M icroscopy
SBF	Simulated B ody F luid
SPD	Severe P lastic D eformation
TEM	Transmission E lectron M icroscopy
UFG	Ultra F ine G ained
UTS	Ultimate T ensile S trength
XRD	X - R ay D iffraction
YS	Yield S trength

Chapter 1

Introduction

1.1 Context

Metals have been used as biomaterials for a long time now as they can serve as structural pieces enable to support a lot of forces and stress. Nowadays titanium, but also cobalt-chrome and stainless steel, are widely employed for medical implants such as dental implants, hip and knee joints, bone plates, screws, etc. However, despite their excellent mechanical properties and inertness towards the human body, researchers are focusing more and more their attention on a new generation of biodegradable implants that could be naturally degraded in physiological conditions once the load could be safely transmitted to the healed bone. Working on this kind of degradable devices is of great interest when thinking about all the possibilities they offer; further surgeries to replace or remove implants would be avoided in that way, representing a considerable relief for the patients, associated with a loss of pain and a cost reduction.

In this configuration magnesium and its alloys seem to be a promising candidate materials owing to their advantages over other metallic materials, especially with regard to their biodegradability, biocompatibility and low density (meaning a better comfort for the patient). Magnesium is also naturally present in the human body in few quantities and is non-toxic. But, as any metallic biomaterial, magnesium should fulfill the requirements of a good biocompatibility and good mechanical properties. Magnesium has a similar elastic modulus than the bone (30-40 GPa) [6] but its mechanical performance is not good enough to be used as structural implant. Moreover, magnesium presents a high corrosion rate which is not conceivable for such field of application. Studies using magnesium as a biodegradable material for the fabrication of implants have shown promising results but a lot of work remains to be done. This thesis can be incorporated within the framework of this relatively new research for fabricating biodegradable implants.

1.2 General framework for using magnesium as a biodegradable implant and statement of the problems

This section aims at giving a general knowledge of biodegradable implants for load bearing application and stating the difficulties the research is currently facing. As a new generation of biodegradable implants, magnesium is used as a substrate and should therefore be able to support loads without any failure. Flexion, tension, shear, compression or torsion can eventually be transmitted to the structure during the surgery or during the implantation period, which explains the need for high levels of strength. Although magnesium has relatively good mechanical properties with a Young modulus (E) of 30-40 GPa, the risk of an implant failure cannot be tolerated in any way and therefore its mechanical properties must be improved. Consequently the scientific community is putting a lot of efforts to develop a magnesium-based structure able to be used for load bearing application. Moreover, making strong structures opens the range of possibilities for the design of implants by fabricating strong porous structures, working with complex shapes and narrow sections or simply reducing the size of the current implants.

In an attempt to improve the mechanical properties of a metal, scientists usually perform either a thermal treatment, commonly known as ageing, or a mechanical treatment which consists in introducing severe plastic deformation (SPD) into the material. The mechanisms occurring during these processes, such as grain refinement, change of texture and the formation of strengthening particles are nowadays well known and understood by the scientific community. The most famous severe plastic deformation process is known as equal channel angular pressing (ECAP). Very good results can be obtained with the ECAP process with a grain size refinement up to the nano-scale. However, ECAP is not well suited for an industry scale production as it is a batch process that requires multiple repetitive steps and as such is time- and labour-consuming. Also the resulting texture promotes dislocation glide on basal planes which is not favorable for the formability of magnesium [10]. Therefore a new technique suitable for the production of implants and that could provide such mechanical improvement is needed.

The high corrosion rate of magnesium is also another big issue to take into consideration. Although the disintegration of magnesium and the safe excretion of its resultant products by the kidney confer it its best advantage of being biodegradable, it also reduce dramatically its use as an implant substrate. Indeed, the fast corrosion rate of pure magnesium in physiological environment, 10.5 to 210 mm per year [11], generates a loss of its mechanical integrity within few days. Moreover it was stated that load bearing orthopedic implants should remain present in the body for a period of 12-18 weeks while the damaged bone tissue is healing. The degradation of magnesium is also accompanied by the release of hydrogen gas which can be harmful for the body due to the formation of a gas bubble under the skin and an increase of the alkaline pH in the vicinity of the corroded surface. Therefore a suitable degradation rate of magnesium is

determinant for the promising future of magnesium and its alloys as body implants. The implant should maintain its mechanical integrity long enough for the damaged bone tissue to heal, after what it could gradually be dissolved or absorbed in the human body. In order to increase the corrosion resistance of exposed magnesium, the most effective method consists in carrying out a surface modification so that the contact between the magnesium substrate and the physiological liquid can be avoided. Ceramic, metal, polymer or a combination of the three can be deposited on the surface of magnesium using several techniques involving ion implantation, chemical conversion treatment, anodic oxidation, spin coating, spraying, etc. However it is essential that the coating sustains protection under deformation due to the stress and strain transmitted to the implant during the patient activity. It has been shown that hydroxyapatite (HA) is particularly suitable for promoting cell attachment and accelerating bone growth [1] but its use for load bearing applications is limited due to its brittle behaviour. Despite the large amount of studies focusing on the subject, no magnesium-based implants have been developed for commercial use so far. Critical factors such as corrosion rate, surface chemistry, adhesion, coating morphology, thickness and stability are essential to evaluate the coating performance and must be checked simultaneously to fulfill all the requirements of an implant structure in terms of biocompatibility, mechanical properties and biodegradability.

1.3 Outline of the thesis

The goal of this thesis is to develop a system that responds to the two problems mentioned above, which are the low mechanical properties of magnesium as a substrate for load bearing applications and its high corrosion rate. From these objectives, the document is organized in four chapters that are now presented.

Chapter 2 contains a background theory of magnesium properties and the different surface modification technologies. The first section of this chapter starts with the deformation modes of HCP materials such as magnesium and the concepts of severe plastic deformation (SPD) as well as hardening precipitation in which second phase particles precipitate from the solid solution and hinder the movement of dislocation, resulting in enhanced mechanical properties. The second section of this chapter is related with the surface modification of magnesium and the different techniques that can be used to reduce its degradation rate. The review focuses on polymer and ceramic, particularly hydroxyapatite, coatings. Corrosion mechanisms are also explained.

Chapter 3 aims at using three roll planetary rolling (colloquially called screw rolling) as a new SPD technique for enhancing the mechanical properties of magnesium. Compared to ECAP, this process presents the advantages of the speed at which the material is deformed (few seconds), flexibility with regard to the workpiece dimensions and a broad range of possible process

parameters, including temperature and the rate of deformation, which makes it well suitable for mass production. However, publications on the use of this technique are rather scarce and more experimental data are needed to assess the potential of this process. In this chapter the study has been carried out with pure magnesium to make the case as simple as possible. Extruded pure magnesium rods have been processed 11 times with the first pass conducted at 250°C and with a scaling down of temperature for the following passes until reaching room temperature for the last pass. Microstructure, texture and mechanical properties analysis were performed after 1, 6 and 11 passes by the mean of optical images, transmission electron microscopy (TEM), X-ray diffraction (XRD) and tensile tests.

Chapter 4 is devoted to the strengthening of WE43 magnesium alloy (Mg-RE alloy with 4% Yttrium, 3% Neodymium) which is more and more used for biomedical applications due to its non toxicity and low corrosion rate. In a search for a process amenable to industry production and in a care of time processing optimisation, the number of passes of screw rolling was reduced to its minimum in this study. An ageing treatment was associated with the deformation of the material to induce hardening precipitation. Here, a WE43 rod was first annealed at 525°C for 8h, subsequently screw rolled at 400°C and quenched in water. In order to further improve its strength, the sample was aged at 210°C for 16h so the precipitation of the second phase from the solid solution could occur. Microstructure analysis, hardness distribution, texture evolution and tensile tests were evaluated after each step of the thermo-mechanical treatment. The phase, shape and composition of the hardening precipitates formed during ageing were assessed by TEM. In the second time of the study, and in order to provide a full characterization of the process, the number of passes was increased up to three and the ageing time set to different periods of time, ranging from 10 minutes to 7 days.

Chapter 5 focuses on the fabrication of a coating for WE43 able to reduce its corrosion rate, provide good biocompatibility and sustain protection under deformation. A first HA coating layer was formed by immersing the WE43 sample in an aqueous solution containing ethylenediaminetetraacetic acid calcium disodium salt hydrate (Ca-EDTA) and potassium dihydrogenphosphate (KH_2PO_4) with a pH of 9.3 for 2h. A poly-lactid-L acid PLLA (10%wt. dissolved into di-chloro-methane (DCM)) layer was then added by dip coating technique under vacuum at a speed of 300 mm/sec. The thickness and morphology of the composite coating were first characterized by the mean of field emission scanning electron microscopy (FESEM), focused ion beam (FIB) and by performing adhesion test to evaluate the bonding strength between HA and the substrate. Strain of 5% was then applied to the coated specimens and the corrosion behaviour was assessed by immersion into SBF at 37°C. The bioactivity and cell affinity were measured by cell attachment and proliferation test.

Finally, chapter 6 summarizes the conclusions of this thesis and proposes future research directions of the works described here.

Chapter 2

Theoretical review

2.1 Magnesium as a structural implant substrate

2.1.1 Advantages of using magnesium as an implant substrate

The idea of using magnesium for biomedical application was raised at the beginning of the 20th century with the first experiments of E. Huse and E. Payr (a full review of the history of biodegradable magnesium implants can be found in [12]). Nevertheless the research has really boomed in the last decades when the scientific community has become fully aware of the potential of magnesium as a biomaterial and the vast field to develop a new range of commercial products for a new generation of biodegradable implants. The advantages attributed to magnesium as a material for biomedical application are listed below:

- Magnesium is present as a natural ion in the human body with a total amount of 21-28g (about 1 mol) with 50-60% contained in the bones and most of the rest in soft tissues. Magnesium is also involved in many human metabolic and biological reactions including protein synthesis and blood pressure regulation and is non-toxic [13, 14].
- Magnesium is the easiest structural material to machine [15] which allows the fabrication of complex shapes. It represents a big advantage when one knows that implant structures must be tailored to fit the size and shape of the body of each patient.
- Magnesium is biodegradable. Its main drawback (a weak corrosion resistance) turns to be its main advantage. Unlike other materials currently used as implant substrates, magnesium could safely be degraded into the human body once the damaged bone has healed, avoiding therefore the need for a post-surgery to replace or remove the implant. By controlling the cell affinity and the degradation rate of the magnesium-based structure, optimal

performance could be reached. Figure 2.1 illustrates the concept of implant degradation throughout its lifetime in the body via cell colonization and bone growth and provides a conceptual idea of the use of biodegradable implants.

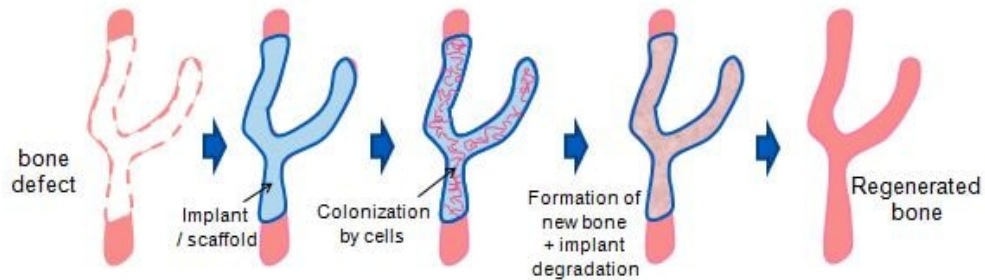


FIGURE 2.1: Schematic drawing of biodegradation process of an implant after its implantation into the body.

- Magnesium has a low density and can be found at a relatively low price. With a density of 1.7 g/cm^3 magnesium is very light and is assimilated with the bone ($1.2\text{-}1.6 \text{ g/cm}^3$) which makes it more comfortable for the patient. As a comparison, titanium and stainless steel have a density of 4.5 and 7.8 g/cm^3 respectively [6]. Moreover magnesium is 7 to 8 times cheaper than titanium [16].
- Magnesium could stimulate bone tissue growth. Few studies have demonstrated that magnesium has a good biocompatibility since the release of magnesium ions is not detrimental to the human body but rather helps the formation of biological apatite, the main bone mineral component [1, 17]. An in-vivo study conducted by Witte et al. [18] showed an osteoblastic response to the degrading magnesium alloys inserted into the guinea pig femur, with an increased bone mass around the specimens.

2.1.2 Mechanical properties of magnesium

When compared to other metallic implant materials, magnesium presents mechanical properties that seem well suited for the fabrication of medical implants. Its best attractive feature subsists in its elastic modulus of $30\text{-}45 \text{ GPa}$ that is very close to that of the bone ($5\text{-}20 \text{ GPa}$). A mismatch in the elastic moduli can lead to a stress shielding of the injured bone which consists in a reduction of its density as a result of the implant carrying a greater portion of the load due to its high modulus. It can lead to critical clinical issues, early implant loosening, damage to the healing process, skeletal thickening, etc [19]. Stress shielding effect happens to be very common with titanium based implants due to their high elastic modulus of $100\text{-}125 \text{ GPa}$ and their use for load bearing applications. Cobalt chrome and stainless steel are also too stiff with range of values of $200\text{-}250 \text{ GPa}$ and $190\text{-}200 \text{ GPa}$, respectively [6]. In that sense it is believed that magnesium based implants reduce the stress shielding effect and eliminate the risk of post-surgery problems.

Moreover magnesium has excellent damping capacity (ability to absorb energy) [13] which can be very important in the case of load bearing applications, where the shock and vibration have to be reduced and absorbed. Table 2.1 summarizes the mechanical properties of various implant materials compared to the one of natural bone [6–8].

TABLE 2.1: Summary of the physical and mechanical properties of various implant materials in comparison with natural bone [6–8].

Material	E (GPa)	σ_{YS} (MPa)	σ_{UTS} (MPa)	ϵ_f (%)	K_{IC} (MPa.m ^{1/2})	ρ (g/cm ³)
Natural bone	5-20	-	100-150	2-3	2-6	1.6-1.9
Stainless steel	190-200	200-350	500-800	40-50	50-200	7.9
Pure magnesium (cast)	30-45	20-40	80-90	3-6	15-40	1.738
Titanium alloys	100-125	700-900	800-1300	10-20	28-108	4.5
Co-Cr alloys	200-250	400-550	800-950	15-20	-	9.2

σ_{YS} : yield strength, σ_{UTS} : ultimate tensile strength, ϵ_f : elongation to failure, ρ : density

Although magnesium seems to be a good candidate material for use as a biomaterial, its mechanical properties remain relatively low, attributed to its hexagonal crystal structure. Its yield strength of 20 MPa and its ultimate tensile strength of 80 MPa certainly prevent any stress shielding effect but appear to be insufficient to carry high loads without failure. The mean load on a hip joint for example is up to 3 times the body weight, 3000 N, and can even reach 10 times the body weight, 10000 N, when jumping [20]. Therefore the mechanical behaviour of an implant structure should be high enough to fulfill the bearing functions during the implantation period. Erinc et al. [21] proposed specific mechanical and corrosion requirements for biomaterials used in bone-implant fixture applications. They suggested a strength higher than 200 MPa, an elongation greater than 10% and a corrosion rate less than 0.5 mm/year.

The fact that a biodegradable implant is designed to degrade also means that its shape and mechanical properties constantly change over its life in the human body, adding another degree of complexity in the forecast of its in-vivo behaviour. S.E. Henderson et al. [22] for example have studied the in-vivo degradation of pure magnesium by the mean of screws implanted in the craniofacial bone of rabbits for a period of 4, 8 and 12 weeks. A fast degradation of the screws was shown with a decrease of the volume fraction over the weeks. By 4 weeks the remaining volume fraction was of about 70% while more material seemed to be degraded after 8 weeks with a volume fraction of about 60%. After 12 weeks the mean volume fraction decreased up to about 35%. In the same way S. Kim et al. [1] have shown that severe in vivo biodegradation occurred in pure magnesium screws implanted in rabbit tibial shafts after 6 and 12 weeks. In the same study tensile specimens were also inserted into the bone-pericranium pouch of rats and the tensile strength measured over the implantation period. It was shown that the tensile strength of pure magnesium decreases from 200 MPa to 130 MPa and to 100 MPa after 4 and 12

weeks of implantation, respectively. The results are presented in figure 2.2. According to the fast degradation of pure magnesium in the physiological environment, it is clear that a magnesium implant cannot sustain its mechanical integrity during the bone healing period of 12-18 weeks. Increasing the strength of magnesium would allow to maintain its mechanical integrity for a longer period of time.

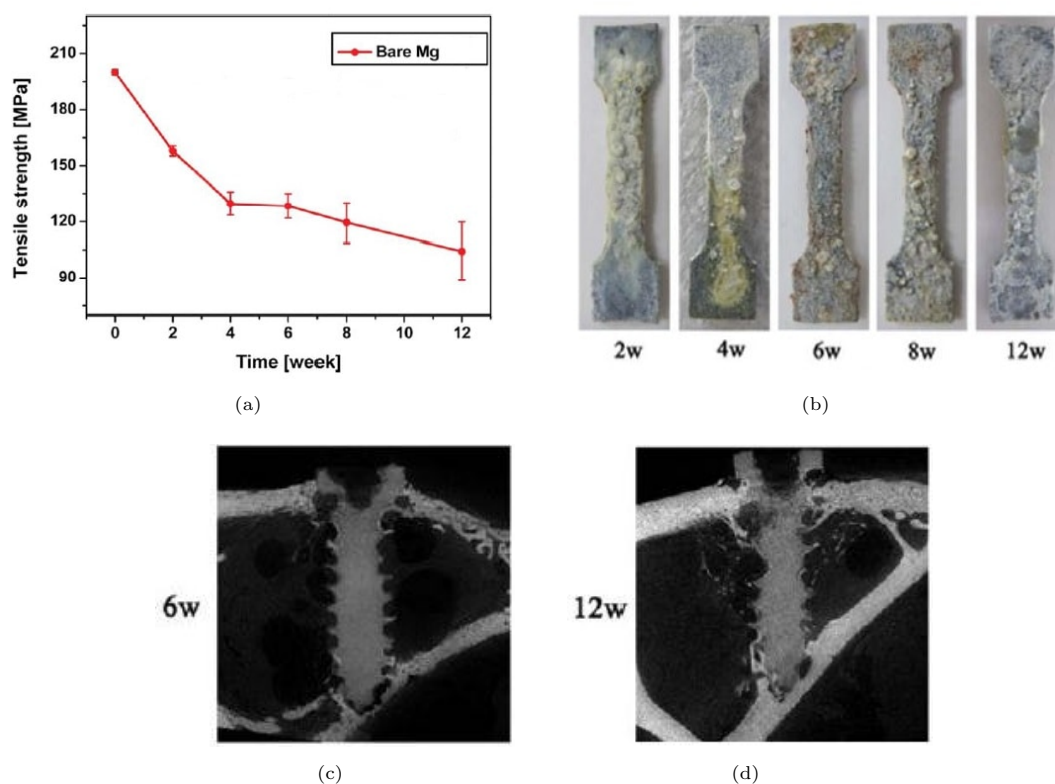


FIGURE 2.2: (a) Ultimate tensile strength of pure magnesium after 2, 4, 6, 8 and 12 weeks of implantation in rabbit tibial shafts (b) Optical pictures of the same pure magnesium specimens after 2, 4, 6, 8 and 12 weeks of implantation (c) Reconstructed μ CT-image of pure magnesium screw specimens after 6 weeks and (d) 12 weeks of implantation. Cited from [1].

Moreover, high strength materials could extend the scope of biomaterials by developing innovative products in agreement with the future challenges. For example, porous scaffolds with appropriate pore size has long been seen as the ideal bone-implant interface since they provide a biological anchorage for the surrounding bone tissue and facilitate the migration of osteoblast cells from surrounding bone into the implant site (osteoconductivity) [23]. However the presence of pores prevents the scaffold to reach high compressive strength which restricts their use in a lot of applications. It is therefore clear that using high strength materials as the scaffold matrix turns to be a necessary condition for the development of such structures.

2.2 Deformation of hexagonal close packed structure and strengthening mechanisms

As explained in the previous section, improving the mechanical properties of magnesium is a serious challenge for their use in biomedical applications. Introducing severe plastic deformation (SPD) is one of the most famous and efficient way to increase the strength of a material by a grain refinement and a change of texture. Precipitation hardening is also another technique to reach high levels of strength. However the hexagonal close packed (HCP) structure of magnesium makes its deformation more complicated than materials with a face centered cubic or body centered cubic crystal structure.

2.2.1 Crystal structure of hexagonal close-packed of magnesium

The deformation of magnesium and its alloys is quite complex since their formability at room temperature is very poor, which can be attributed to their HCP structure and their insufficient independent slip systems.

Basal slip has been identified as the predominant deformation mechanism in magnesium at room temperature as a uniform distribution has been observed all over the grains when subjected to tensile tests at 25°C [24, 25]. The critical resolved shear stress (CRSS) of basal slip system at room temperature is very low, in the order of 1 MPa, much lower than the one of non-basal slip systems such as prismatic and pyramidal slip systems. Prismatic $\langle a \rangle$ glide has been observed as the second deformation mode at low temperature but does not play a role as important as basal $\langle a \rangle$ system. Therefore the operative slip systems at ambient temperature consist of two independent basal slip systems (one plane and two Burgers vectors) and two semi-active independent prismatic slip systems (two planes and one Burgers vector) which is not sufficient to fulfill the Von Mises criterion that states that at least five independent slip systems are required for plastic deformation of polycrystalline materials [26]. This explains the poor formability of magnesium and its alloys at room temperature. Deformation twinning plays an important role in plastic deformation of magnesium by adding additional active deformation modes and thus improving its formability. The CRSS of magnesium alloys varies with temperature; particularly non basal slip systems are more sensitive to temperature and decrease with increasing temperature. Therefore at high temperature, prismatic $\langle a + c \rangle$ glide and pyramidal $\langle a + c \rangle$ glide contribute to the deformation of magnesium, allowing numerous active deformation modes. Table 2.2 summarizes all the independent modes of deformation in hcp structures while figure 2.3 gives a representation of the possible slip modes encountered in magnesium with the associated basal, prismatic and pyramidal slip systems [2, 9].

TABLE 2.2: Slip planes and directions of the different dislocation types in HCP crystals [9].

Deformation mode	Slip plane	Slip direction	Number of independent modes
basal slip $\langle a \rangle$	$\{0002\}$	$\langle 11\bar{2}0 \rangle$	2
prismatic slip $\langle a \rangle$	$\{1\bar{1}00\}$	$\langle 11\bar{2}0 \rangle$	2
pyramidal slip $\langle a \rangle$	$\{1\bar{1}0l\}$	$\langle 11\bar{2}0 \rangle$	4
$\langle c \rangle$	$\{hki0\}$	$\langle 0001 \rangle$	
pyramidal slip $\langle a + c \rangle$	$\{h\bar{k}il\}$	$\langle 11\bar{2}\bar{3} \rangle$	5

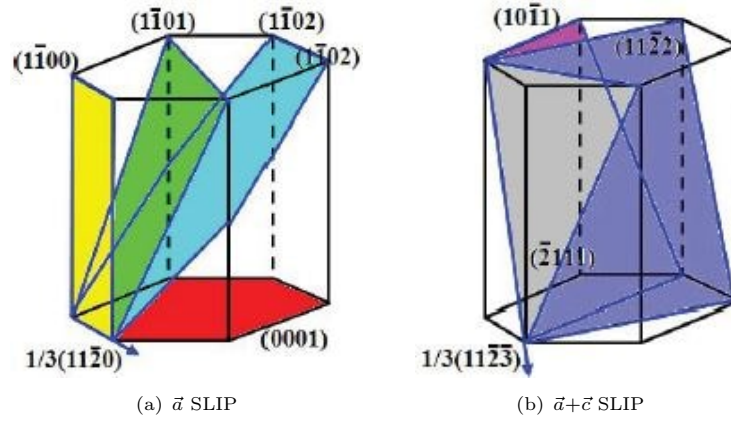


FIGURE 2.3: Theoretically possible slip modes in magnesium ; colored surfaces represent each slip planes, arrows represent slip direction Burgers vectors (a) $\langle a \rangle$ type slip system (b) $\langle a + c \rangle$ type slip system [2].

2.2.2 Strengthening of materials by SPD techniques

Recently it was shown that a change of grain size accompanied by a grain boundary sliding and/or grain rotation are important factors of the ductility and formability of magnesium and its alloys. A lot of studies [27, 28] have for example demonstrated that SPD techniques are quite effective in enhancing the ductility of materials by introducing high strain responsible of grain refinement and development of a crystallographic texture. G.D. Fan et al. [3] have processed extruded pure magnesium by equal channel angular pressing (ECAP) at 300°C for the first two passes using a die with a channel angle of 90°C and at 200°C for the following 3-6 passes using a 135°C die; results are shown in figure 2.4. A clear grain refinement was observed with a decrease in the grain size from 45 μm in the initial stage to 3-20 μm (bimodal grain size distribution) after 6 passes. Pole figures also revealed that the intensity of basal plane decreased with the number of ECAP passes, together with a gradual increase of Schmidt factor from 0.22 to 0.32 after 6 passes. As a result the yield strength decreased from 200 to 175 MPa and the elongation increased from 7 to 27%, indicating that the texture softening effect offsets the strengthening effect. Indeed, two mechanisms usually take place during SPD: a strengthening effect or a softening effect. Grain refinement by SPD generally leads to a strengthening of the material but the simultaneous development of a crystallographic texture also affects the mechanical properties

of the material. High strength and good ductility are often mutually exclusive and improving both at the same time is a challenging task.

The most accepted model for grain refinement during SPD is attributed to the introduction of high strains into the material and the formation of a high density of dislocations that re-arrange to form an ultrafine-grained (UFG) microstructure. To give an order of idea the dislocation density increases from 10^{10} dislocations/cm² in an annealed state to 10^{12} - 10^{16} dislocations/cm² after moderate rolling or heavily cold work. Grain fragmentation models are based on the notion that a dislocation cell structure transforms to a final fine grain structure via the accumulation of misorientation across the dislocation cell boundaries. Therefore, the materials produced in this way often include a large fraction of grain boundaries having high angles of misorientation (HAGB $\geq 15^\circ$) [10]. Low angle grain boundaries (LAGB) (misalignment $\leq 15^\circ$), on the other hand, are not effective in blocking the dislocations. The most famous models of grain fragmentation have been proposed by Kocks-Mecking [29], Prinz and Argon [30] and later by Estrin et al. [31] for example. As a consequence of the grain refinement, the mechanical properties are seen to be improved according to the famous Hall Petch relationship:

$$\sigma_Y = \sigma_0 + kd^{-1/2} \quad (2.1)$$

where σ_Y corresponds to the yield stress, σ_0 the so called friction stress representing the overall resistance of the crystal lattice to dislocation movement, k the locking parameter (a constant) and d and the average grain size. With decrease in grain size the mean distance of a dislocation can travel decreases as grain boundaries act as an obstacle to their motion. The dislocations start piling up against them and more strength is required to activate the dislocation movement. However for grains in the nano range size the Hall Petch relationship cannot be applied and other strengthening mechanisms have been proposed (not mentioned here). More recently Koike et al. [32] have demonstrated that decreasing the grain size can also improve the ductility of a material. They have shown that an ECAP fine grained AZ31 alloy exhibited excellent ductility with an elongation to failure of 47% when tested under tension with aligned basal planes. A high dislocation activity on non-basal slip systems was found in the deformed microstructure, attributed to stress concentrations at the grain boundary. Their model is based on the need of shear stresses on non-basal glide system in order to bond two deformed grains and prevent the fracture along grain boundaries. Therefore, following their hypothesis, it is possible to state that during deformation in a coarse grained structure twinning plays an important role while in a fine grained structure prismatic slip systems do, resulting in enhanced ductility.

Grain orientation is another important factor of SPD. When a polycrystal is plastically deformed a strong preferred orientation, or texture, develops due to the activation of slip or/and twin systems. The deformed grains tend therefore to align along the same direction and a high

anisotropy appears in the material, affecting its mechanical properties. The enhanced ductility observed in the study of G.D. Fan et al. [3] can be attributed to the orientation of the grains with their (0002) planes parallel to the extrusion direction (ED) and also located at about 35° from the normal direction (ND) towards ED and 15° from ND to TD. This texture, associated with the increase of the Schmidt factor, promotes dislocation glide on basal plane and lead to a ductility improvement.

In summary, ECAP technique is well known for producing fine grained structure with a grain refinement down to $1\ \mu\text{m}$ or even sub micron scale but the resulting texture tends to promote dislocation glide on basal plane which improves the tensile ductility but negates the strengthening effect of the grain refinement. Researchers are therefore working on other SPD techniques such as high pressure torsion (HPT), twist extrusion, roll bonding, etc. Details about these techniques can be found in the literature.

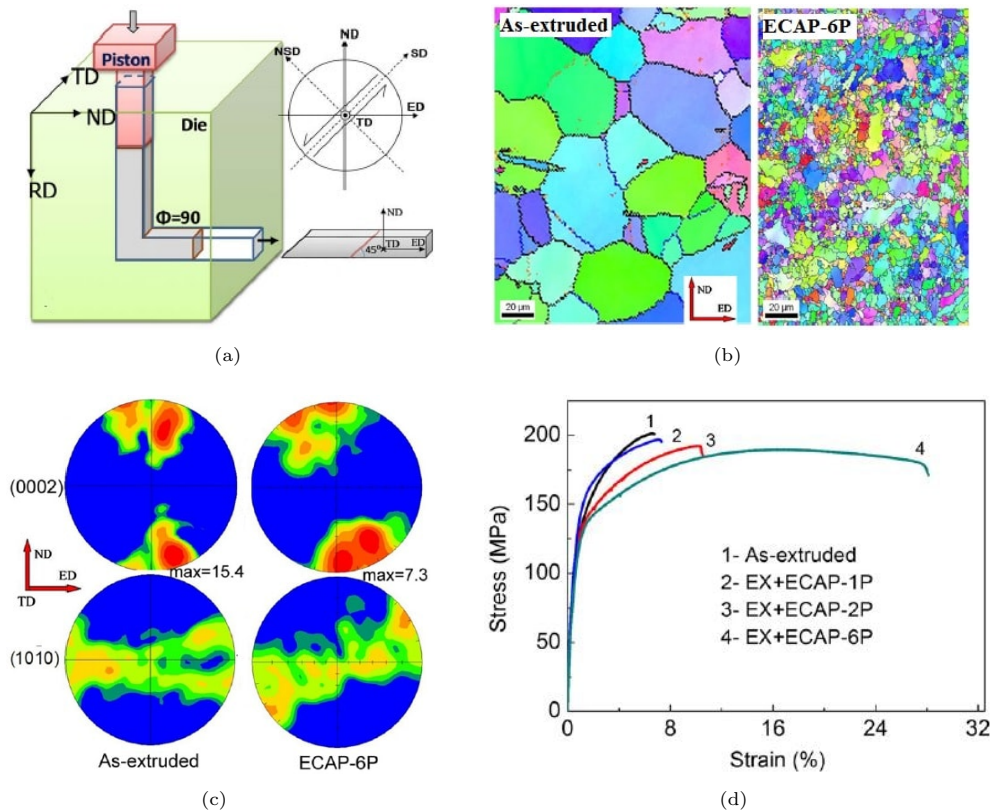


FIGURE 2.4: (a) schematic of ECAP technique (b) grain refinement observed in the microstructure of pure magnesium in the extruded state and after 6 ECAP passes (c) (0002) and (10 $\bar{1}0$) pole figures of as extruded magnesium and ECAPed magnesium (d) strain-stress curves of as extruded magnesium and after 1, 2 and 6 ECAP passes. Cited from [3].

2.2.3 Precipitation hardening

Precipitation hardening, also called age-hardening, is a versatile thermal method for obtaining high strength levels material. It relies on changes in solid solubility with temperature to reduce the size of the second phase particles of an alloy which impedes the movement of dislocations in the lattice. The size, shape and density (dispersion) of the particles precipitated from the super saturated solid solution (SSSS) at low temperature are key factors in improving the mechanical properties of a material. Strengthening a material using a combination of plastic deformation via SDP techniques and thermal treatment is not commonly encountered but represents a great potential to achieve very high mechanical properties. V.V. Latysh et al. [33] for example have managed to reach an excellent yield strength (YS) of 1100 MPa, an ultimate tensile strength (UTS) of 1230 MPa and an elongation to failure of 14% by ECAP processing and carrying a thermal treatment to pure titanium.

In the case of magnesium ageing turns also to be a very effective method for improving its mechanical properties. R. Xin et al. [34] have evaluated the increase of strength after a thermal treatment of a Y-Nd-Mg alloy by performing tensile tests. The extruded alloy was first solution treated at 525°C for 24h, quenched and finally aged at 210°C for 59h. It was observed that the aged alloy had a YS one third higher than the one of the initial extruded alloy with values of about 300 MPa and 200 MPa, respectively. It was shown that the final properties of the material strongly depend on the ageing temperature and holding time. As it is presented in figure 2.5 with data of WE43 alloy, microhardness increases with time with a maximum reached after 1×10^3 - 2×10^3 minutes (16h - 33h). Besides, Mengucci et al. [4] reported that an ageing temperature of 210°C would provide the highest hardening response of the WE43 alloy for ageing time higher than 4×10^2 minutes (6h).

The biocompatible magnesium - rare earth (Mg-RE) alloys precipitate from the solid solution according to the Polmear Guinier sequence of phases $\beta'' \rightarrow \beta' \rightarrow \beta$ [35]. Several studies have tried to follow the formation and evolution of hardening precipitates in Mg-RE alloys during artificial ageing between 150°C and 280°C by the mean of transmission electron microscopy (TEM) and small angle X-ray scattering (SAXS) in order to study the shape and analyze the crystallographic structure of the precipitates. In figure 2.6 are presented the TEM bright field images of WE43 alloy annealed at 525°C for 8h, water quenched and aged at different temperature of 150°C, 210°C, 250°C and 280°C for different periods of time [4]. From the latter results of Mengucci et al. and the ones of Antion et al. [35] and Barucca et al. [36] the following conclusions were reached and are now well accepted:

- The β'' phase is generally observed in the first stages of precipitation at low temperatures (150-200°C) and is expected to have a platelet shape. The commonly accepted composition

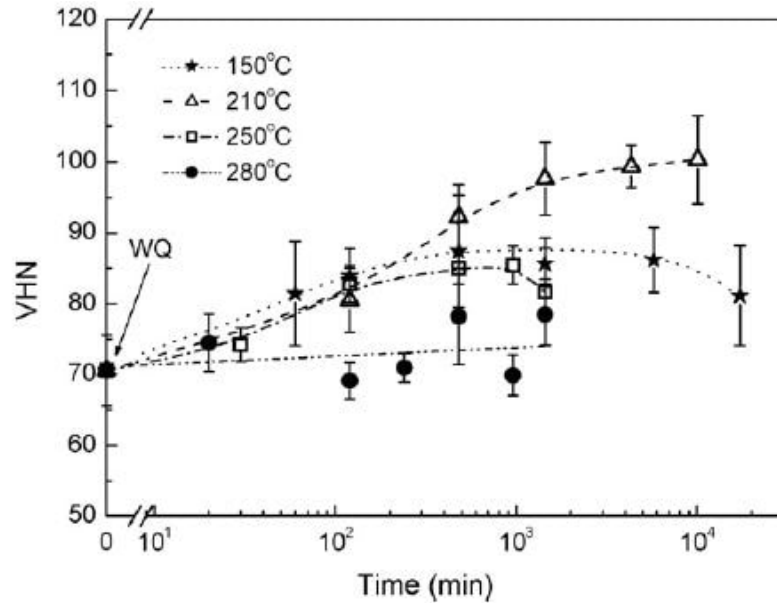


FIGURE 2.5: Vickers hardness for different temperatures as a function of ageing time [4].

of β'' phase is $\text{Mg}_3\text{Y}_{0.85}\text{Nd}_{0.15}$. The β'' phase is believed to be responsible of the hardness increase.

- The intermediate β' phase forms at slightly higher temperatures (200-250°C) and has been identified with as orthorhombic with a Mg_{12}YNd composition. The temperature at which β'' transforms into β' has not been clearly identified yet. The microstructure of WE43 aged at 210°C for 1 day revealed the presence of both phases while at longer ageing time (7 days at 210°C) the situation appeared different with the only presence of β' . Ageing the alloy at 250°C for 16h caused the precipitation of β' phase.
- The precipitation sequence ends with the formation of the equilibrium β phase that forms at temperatures of 250°C or higher. It has an face centered cubic structure and its composition is believed to be $\text{Mg}_{14}\text{Nd}_2\text{Y}$.

2.3 Corrosion of magnesium and surface modification of implants

As mentioned in the first chapter, corrosion of magnesium remains the main obstacle to its use for biomedical applications. The acceptance of an artificial implant by the body mainly lies into the implant and surrounding tissues contact, which allows the bone to biochemically recognize the graft as a natural bone and grow over it (guided tissue regeneration) to later resorb and replace it with the patient own native bone. The corrosion of magnesium alters the bone proliferation since bone cells are very sensitive to the chemical products generated during corrosion and the release

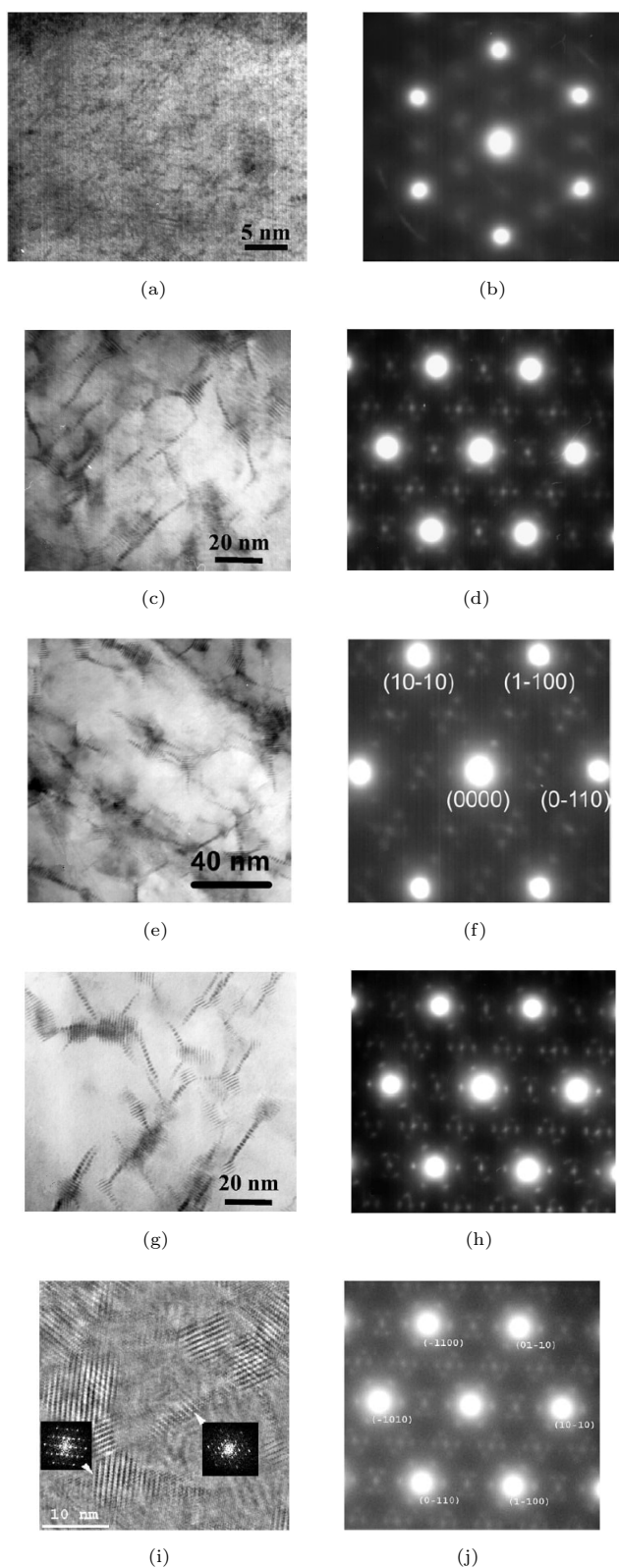


FIGURE 2.6: TEM results obtained along the $\langle 0001 \rangle$ zone axis of (a) BF of sample aged at 150°C for 12 days (b) corresponding SADP (c) BF of sample aged at 210°C for 1 day (d) corresponding SADP (e) BF of sample aged at 210°C for 3 days (f) corresponding SADP (g) BF of sample aged at 210°C for 7 days (h) corresponding SADP (i) BF of sample aged at 250°C for 4 hours (j) corresponding SADP.

of hydrogen gas that can be harmful for the surrounding tissues [6]. A surface modification of magnesium is therefore necessary to prevent its corrosion in the physiological liquid and make a good affinity with the bone cells. In a second time, the implant resorption rate must be controlled to allow the bone to heal over a period of 12-18 weeks.

2.3.1 Corrosion mechanisms of magnesium and its alloys and consequences for the implant surrounding tissues

Magnesium is a relatively reactive metal. Hence, when immersed into simulated body fluid (SBF), Hanks solution or physiological liquid, it reacts with water to form $\text{Mg}(\text{OH})_2$ on its surface and releases H_2 gas [37]. The too fast generation of by-products can cause serious problems for the patient health. Since the early stage of experiments conducted at the beginning of the 20th century, the formation of gas cavities after implantation of the magnesium implants has widely been reported in the literature. Recently many researchers have highlighted the gas bubble formation by the mean of advanced technology. P.R. Cha et al. [38] have for example studied the gas released from extruded Mg-5 wt% Ca implanted into the dorsal abdominal region of Sprague-Dawley rats. It was shown that a gas bubble was formed within the first week after surgery and persisted for the entire 12 weeks period. It is commonly admitted that the main gas component formed is hydrogen due to the magnesium corrosion reaction that lead to the formation of H_2 . Although it is generally stated that H_2 gas would be harmful for the tissues it has remained unclear in what circumstances it badly affects them and whether bone healing is negatively altered. To answer this question Witte et al. [39] have implanted four different magnesium alloys, AZ31, AZ91, WE43, LAE442, with a rod size of 20 mm length and 1.5 mm diameter into the guinea pig femora. All implants exhibited gas bubbles that appeared within one week after surgery but disappeared after 2-3 weeks. No adverse effects on the bone growth due to the gas bubbles were observed in the guinea pigs. Moreover, the same author has investigated the presence of hydrogen in the gas cavities formed after the implantation of mg-RE alloys under the skin of hairless mice. The H_2 concentration was measured using a H_2 microsensor as described in [40]. The results revealed that the gas cavities contained only a low concentration of hydrogen gas with values of 0.2 ± 0.1 vol.% after 1 day surgery and 1.15 ± 0.09 vol.% after 10 days surgery.

Unprotected magnesium exposed to aqueous physiological environment will also develop a hydroxide $\text{Mg}(\text{OH})_2$ layer on its surface due to the precipitation of Mg^{2+} and OH^- ions, both results of the cathodic and anodic partial reactions. The hydroxide layer accumulates and forms a protective corrosion layer that may slow down or provide some protection to the underlying magnesium substrate. It has also been observed that the corrosion layer, in direct contact with

the surrounding bone, contains calcium phosphate, a feature that may be exploited to improve osteoconductivity [6] due to its similar composition with the bone.

In spite of the few clinical successes like the one of Witte et al. where no gas bubble was observed after several weeks of implantation and the good osteoconductivity of the hydroxide layer, it remains that the corrosion rate of magnesium is too fast to deal with the host tissue and does not allow the implant to maintain its mechanical integrity and stability during the healing bone period. Kraus et al. [41] implanted cylindrical ZX50 implants into femoral bones of rats and monitored tomography images over the entire period of degradation. The initial implant volume of 15 mm^3 rapidly decreased to 4 mm^3 after only 8 weeks. Yang et al. [42] also showed the rapid degradation behaviour of AZ31 when immersed in NaCl solution. A mass loss of 23% was observed after 15 days of immersion. Moreover the degradation of magnesium is not homogeneous and an alkaline pH shift in the vicinity of the implant represents a concern for medical applications.

2.3.2 Corrosion behaviour of SPD processed magnesium

Recently, the effect of grain size on corrosion of magnesium and its alloys has also been investigated. Although it is hard to isolate the only effect of grain size because of the introduction of dislocations, segregation, texture and so on during SPD, it has demonstrated that microstructural changes occurring during deformation affect the corrosion behaviour of magnesium. Most of the studies support the idea that UFG materials present a superior corrosion resistance than coarse structure materials. In the case of magnesium it has been suggested that ECAP treatment simultaneously lower the anodic and cathodic kinetics, thus improving the quality of the oxide layer naturally present on the surface of magnesium by modifying its substrate. Indeed, in aqueous solutions with pH below 11 this oxide layer is not stable and easily cracks (geometrical mismatch with respect to the hexagonal magnesium lattice), resulting in very low electrode potential of magnesium. The introduction of a large volume fraction of grain boundaries in the bulk material may diminish the mismatch by creating a more stable and coherent oxide film on magnesium surface. Among scientists who defend this theory, Orlov et al. [43] showed a correlation between the improvement of corrosion resistance and both grain refinement and the redistribution of Zn and Zr solutes within the microstructure of an extruded and ECAPed ZK60. It appeared that grain refinement had the greatest effect upon anodic reaction kinetics while chemical effects (solute distribution) had a greater impact on cathodic reaction kinetics.

On the other hand, surface mechanical attrition treatments (SMAT) appears to lower the anodic kinetics and increase the cathodic kinetics as compared to the cast material, resulting in a high corrosion rate. Moreover, some studies have indicated that the increase of LAGB density occurring during this process and massive residual stresses can deteriorate the quality of the

oxide film via peening stress mechanisms, thus not offering a good protection to the magnesium substrate [44]. The results of Song et al. (2010) [45] are also in good agreement with the fact that SPD processed materials present higher corrosion rates than the non-processed ones. They found that the 6 passes ECAPed pure magnesium with a grain size of 50-100 μm displayed a lower corrosion resistance than the as-cast magnesium with grains of 800 1500 μm , resulting in more and deeper pits after in-situ corrosion, higher mass-loss rate immersed in NaCl solution, larger I_{CORR} values in polarization curves and lower fitted R_t values in impedance test plots. Although the cause of the decrease of corrosion resistance was not clearly demonstrated, the authors of the study concluded that strain induced grain refinement with more crystalline defects (HAGB and dislocations) and the change of β phase from fragments to refined and uniform dispersed particles may promote the corrosion propagation in the alpha matrix due to the lack of significant barrier. Although the cause of the decrease of corrosion resistance was not clearly demonstrated, the authors of the study concluded that strain induced grain refinement with more crystalline defects (HAGB and dislocations) and the change of β phase from fragments to refined and uniform dispersed particles may promote the corrosion propagation in the alpha matrix due to the lack of β particles barriers.

To summarize, there is no detailed understanding of how SPD processing impacts the corrosion behaviour of magnesium and its alloys. The inability to isolate the only effect of grain size has made an exact relationship between grain size and corrosion resistance difficult to generalize. Available publications on this subject reported conflicting findings of increased or decreased corrosion of magnesium depending on the type of deformation and environment. Also, studies reporting enhanced corrosion resistance were generally conducted in relatively non aggressive electrolytes as compared to studies that reported reduced corrosion resistance. The improvement of the protective oxide quality on materials with fine-grained microstructures might therefore fail in high chloride content electrolytes.

2.3.3 Coating of magnesium and its alloys

To tailor the corrosion rate of magnesium, two methods can be considered: the modification of the magnesium microstructure (texture, grain size, second phase particles, etc) and the treatment of the implant surface which mainly consists in performing a coating by using a non toxic and biocompatible material [46]. The second option is generally preferred as it shows better performance in decreasing the degradation rate of magnesium and improving its bioactivity, accompanied with a large choice of techniques and coating materials. A large number of surface treatments have been investigated but most of the studies focus their attention on ceramic and polymer as coating materials since metals are quite bio-inert and their main advantage lies in a good strength and wear resistance, which is already provided by the magnesium substrate.

2.3.3.1 Calcium Phosphate based coating

Ceramics have many appealing qualities for use as biomaterials since they are non-toxic, biocompatible and not recognized as a foreign material by the human body. Calcium phosphate based ceramics and cements have a similar composition and architecture to that of the mineral component of bones and teeth. As a result, they are often used as bone substitute that can exhibit bioactive behaviour and integrate into living tissue by the same processes that are active in remodeling healthy bone. This specific contact between the ceramic based implant surface and the living bone enhances the osseointegration and helps the adhesion and proliferation of osteoblast cells [17]. Li et al [47] have proposed a schematic model illustrating the role of a bone-like apatite interlayer between the implant and the bone. It shows that an implant in direct contact with the bone might degrade too fast and lead to the formation of gaps at the interface; therefore the role of the new formed bone might be limited. However, when a bioactive bone-like apatite coating layer is applied to the implant it helps to slow down the degradation rate of magnesium and enhance the biocompatibility of the implant by making a proper bond between the bone and the structure. Positive bone cells response to the presence of apatite results in the development of a mature new bone in direct contact with the implant.

Calcium phosphate based ceramics coatings have already shown good potential for biomedical applications. Hydroxyapatite (HA) coating, one of the most extensively used synthetic calcium phosphorus ceramics, has widely been studied in the last decade. Kim et al. [1] have for example coated pure magnesium with HA by aqueous solution technique and performed in vitro and in vivo tests to evaluate the corrosion resistance of the coated material as well as its biocompatibility. The results showed that the HA-coating layer remarkably reduced the corrosion rate of magnesium when immersed in SBF, with a very low pH increase after 120 hours immersion. Electrochemical polarization tests performed in SBF also showed that the HA coated magnesium sample had a much lower I_{corr} than the bare one, with values of $3.062 \mu\text{A}/\text{cm}^2$ and $6831 \mu\text{A}/\text{cm}^2$ respectively. Moreover the biological response, including cell attachment, proliferation and differentiation, of the HA-coated samples was enhanced considerably compared to samples without a coating layer. In vivo tests were quite promising since the HA coated screws implanted into the tibia of New Zealand white rabbits promoted bone implant interaction and led to a good contact with the bone. After 12 weeks implantation the HA coated sample showed a bone to implant contact of about 81% while bare magnesium showed a value of 69%.

Ravazi et al [48] have employed another technique to modify the surface of magnesium and the benefits of HA. A fluoridated hydroxyapatite (FHA) coating was applied on a micro-arc oxidation (MAO) AZ91 implant sample by electrophoretic deposition (EPD) which has been broadly used in the biomedical field. The existence of MgO pores facilitated the penetration and attachment of the bioactive ceramic to the implant. The results of the in vivo tests revealed a significant

enhancement in the biocompatibility of FHA/MAO coated implant compared to the uncoated one. The amount of weight loss and magnesium ion release in blood plasma decreased from 30 ppm to 17 ppm for bare AZ91 and coated one, respectively. Moreover, new bone was formed around the coated implant and less inflammation was observed, making the FHA/MAO coated implant a suitable candidate for future clinical orthopaedic applications.

Khanra et al [49] have also successfully fabricated a biodegradable Mg-HAp by incorporating HA powder to magnesium melt and by extruding the composite. Mechanical properties were assessed but no information about the corrosion resistance or biological response was given. Nevertheless, fabricating this kind of material has a lot of potential for the future since the need for coating magnesium would be removed and directly incorporated into the implant substrate. Besides the positive bone cells response to HA and its very good biocompatibility, it remains that calcium phosphates are ceramics with a brittle behaviour and a poor fatigue resistance which limit their use in load bearing applications. That is why, in biomedical applications, calcium phosphates are used primarily as fillers and bone graft substitute where no load is involved [17]. A combination of an aqueous environment with stress can result in cracks, delamination, accelerated dissolution of the HA coating and corrosion of the magnesium substrate through the infiltration of the aqueous solution into cracks, which can influence the long-term stability of the implants.

2.3.3.2 Polymer coating

Polymers appear as other promising candidates to functionalize biomaterial surfaces because of the large diversity of the chemical and physical properties they offer. Due to the infinite variability of polymers, chemical composition and structures, they have widely been used as biomaterials with a large range of functions such as contact lenses (hydrogels), catheters (silicone), breast implants (silicone), bone screws (poly-lactic acid), etc [50]. However, the major limitation of using polymers as biomaterials lies into their poor mechanical properties that limit their use in orthopedics or bone replacement where loads are generally transferred to the implant. The Young modulus and stress to failure of the synthetic PLLA (polylactic-L-acid) polymer are close to 3.5 GPa and 65 MPa for example, much less than that of the bone. Researchers have therefore focused their attention in polymer coatings so that their benefits in terms of biocompatibility, elasticity and biodegradability could still be used without considering the mechanical behaviour issue. Moreover, coating magnesium with biopolymers is a reasonable choice since the surface coating should not confer permanent protection to the implant substrate (in that case the implant cannot degrade). Widely used synthetic polymers like PGA (polyglycolic acid), PLA (polylactic acid), PLGA (lactic acid-co-glycolic acid) degrade by hydrolysis that involves a random breakage of the ester bonds in the polymer chain due to water intake. The hydrolysis, and therefore the bone tissue response, can be influenced by several factors like hydrophobicity, molecular weight, crystallinity or porosity of the polymer layer [51]. H. M. Wong et al [52] have

for example studied the in-vitro and in-vivo behaviour of a biodegradable PCL (PolyCaproLactone) coated AZ91 with a high porosity (pore size of about 350 μm) and low porosity (pore size of about 105 μm). The results first showed that the polymer coating layer helps to reduce the corrosion rate of magnesium and maintain its mechanical properties upon degradation. A good cytocompatibility of eGFP (Green Fluorescent Protein) and SaOS-2 osteoblasts was also found with the coated samples. The effect of the pore size in the PCL layer was barely noticeable in the in-vitro results but was clearly revealed in the results of the in-vivo study in where samples were implanted into the trochanter of New Zealand white rabbits. After 2 months of implantation, the high porosity polymer membrane corroded and a bone formation of 5.17 mm^3 was observed around the implant. The low porosity membrane, however, showed almost the double of bone formation with a value of 10.79 mm^3 and did not have any implant volume reduction.

The good performance of polymers as coating material has also been highlighted in the study of L. Xu et al [53] where PCL and PLLA were spin coated on a magnesium substrate. SaOS-2 cells showed significantly good attachment and high growth on the polymer-coated Mg, demonstrating that all the polymer films can significantly improve the cytocompatibility in the 7-day incubation. The pH measurement of the immersion medium and the quantification of released Mg^{2+} during the cell culture clearly indicated that the corrosion resistance of Mg substrate is improved by the polymer films to different extents, concluding that both PLLA and PCL were promising protective coatings for magnesium implants.

Recently PLA, PGA and their copolymers have also been combined with bioactive ceramics, such as bioglass or HA, to improve the biocompatibility of the composite material and stimulate even more the bone regeneration. A. Zomorodian et al. [54] have applied a composite coating containing polyether-imide (PEI, non degradable polymer) with different amount of DETA (diethylene triamine) and HA on an AZ31 substrate to provide simultaneous corrosion resistance and enhanced biocompatibility. It was shown that PEI coating alone resulted in a delay in the corrosion activity of the magnesium alloy for more than 8 weeks. When DETA and inorganic HA nanoparticles were added, it prolonged the corrosion to more than 12 weeks. However, a too high amount of HA (5%) provoked a particles agglomeration and the creation of hillocks that reduced the protective performance of the coating. Furthermore, the best cell response (adhesion and proliferation) was achieved with the coatings modified with the HA nanoparticles.

Combining calcium phosphorous ceramics and biopolymers seems therefore a good option to produce a biocompatible and biodegradable composite coating structure able to maintain the mechanical integrity of magnesium during the healing period, by using concurrently the good properties of each component. The flexibility, or elastic behaviour, of polymers is another of their great quality. Unfortunately, publications recognizing this property as useful for medical applications are rather scarce since the attention only focuses on the biocompatibility of the coating. Therefore, one can see here a great challenge and an opportunity to develop a strain resistant

composite coating in which the flexibility of polymers could counterbalance the brittleness of ceramics.

2.4 Conclusion

In this chapter the different approaches to overcome the drawbacks of magnesium as a biomaterial have been presented. The first approach is related to the HCP structure of magnesium that leads to severe limitations in their ductility, strength and creep resistance, and therefore to a raise of concerns about their use for load bearing applications. The yield strength of commercially used titanium based implants is three times higher than of magnesium for example. This inherent difficulty may be reasonably overcome by some special SPD processing, such as ECAP, that provide grain refinement and texture to the material. As a result and according to the famous Hall-Petch relationship the mechanical properties are seen to be enhanced. Although it has not been clearly established yet, processed magnesium with refined microstructure may favour the formation of a stable and protective oxide layer on its surface. The second approach consists in implementing a suitable coating on magnesium and its alloys that not only can serve to delay the initial degradation of the alloy, but that may also improve biocompatibility, enabling enhanced osseointegration between the coated implant and the surrounding tissues. Polymers and ceramics are often privileged as coating materials due to their advantages over metallic material, especially in terms of bioactivity and degradability. The biocompatibility of calcium phosphate ceramic HA is particularly high, with very good cell attachment and proliferation over the time and bone growth around the implant, owing to its similar composition to that of the native mineralized bone tissues. However its use for load bearing applications might be compromised due to its brittle behaviour, resulting in an early stage of corrosion due to cracks formation. The researchers attention is also focused on the deposition of a biodegradable polymer-based membrane, such as PLA, PGA and PCL, which provides flexibility, biocompatibility and non permanent protection to the implant substrate.

Chapter 3

Improving the mechanical properties of pure magnesium by three roll planetary milling

3.1 Introduction

One of the limitations of pure magnesium with regard to its use in medical implants is its low mechanical strength and poor ductility, attributed to its hexagonal crystal structure. For use in load bearing applications high strength is required. If one makes a conscious choice to employ pure magnesium in order to eliminate any potentially toxic elements, the only path to strengthening is through grain refinement and texture control. As mentioned in chapter 2, popular SPD techniques, such as ECAP, do lead to substantial grain refinement down to 1 μm , or even sub-micron scale, but the resulting texture promotes dislocation glide on basal planes. This texture is helpful in terms of improvement of tensile ductility of Mg, but it negates the strengthening effect of grain refinement produced by ECAP. In a search for an alternative process, which is more amenable to industry scale production of ultrafine-grained pure Mg, we trialed a deformation process referred to as three-roll planetary milling or (in German literature) Planetenschrgwalzen (PSW) [55, 56] or (in Russian literature) radial-shear rolling [57, 58]. Colloquially, the process is also called screw rolling. This technique has several advantages, such as high speed at which the material is processed, mass production ability, flexibility with regard to the workpiece dimensions, and a broad range of possible process parameters, including temperature and the rate of deformation [59]. Moreover, it was found that mechanical properties are substantially enhanced already after a single pass and no more passes would be needed in an industrial processing environment. The principal design of a three-roll milling machine includes three conical rolls

and a mandrel that drives the billet between the rolls (Fig. 1). The rolls are inclined to the central axis of the rod-shaped billet in such a way that their axes intercept the axis at a fixed offset angle. When passing through the mill, the billet is subjected to a screw deformation that reduces its diameter and increases its length. The final diameter of the billet can be adjusted by modifying the positions of the rolls. Multiple passes with progressively decreased diameter of the processed rod are possible, so that the cumulative strain imparted to the rod can be very large. Publications on the use of this technique are rather scarce [55–61] and to the best of our knowledge it has never been used for processing of pure magnesium.

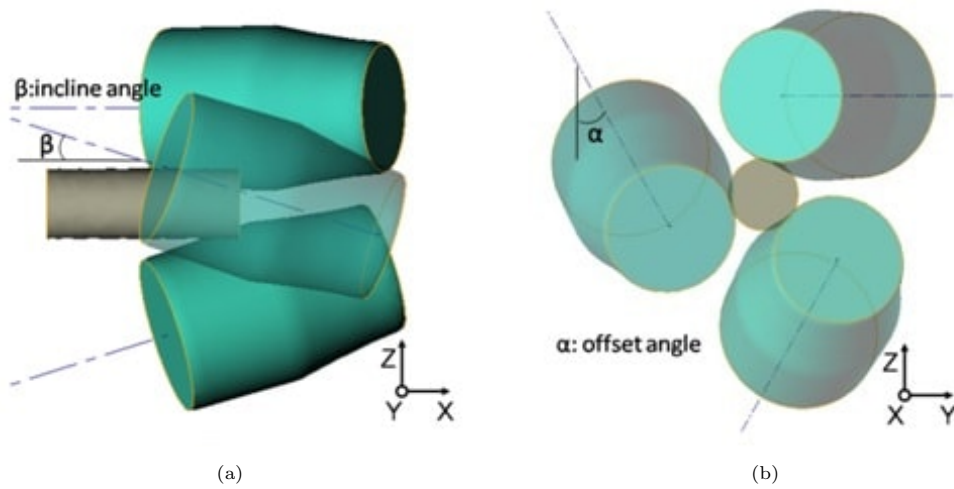


FIGURE 3.1: Schematic of the three roll planetary milling process (PSW) and the arrangement of the rollers.

3.2 Methods

The material used in the present study was extruded magnesium of commercial purity (99.9 wt.%) with minor contamination with Zn (0.011 wt.%) and Si (0.0108 wt.%) received from Yirium Company (China). The material was machined and used in the form of rods 21 mm in diameter and 140 mm in length in order to fit the dimensions of the three-roll mill. Prior to planetary milling, rods were heated in a furnace on air for 30 minutes and subsequently pressed through the three-roll planetary mill at a speed of 80 mm/s. No lubricant was used. The first pass was conducted at 250°C, and the rod diameter was reduced from 21 mm to 19.5 mm. The main objective here was to perform a first refinement of the microstructure so that the following passes would be able to be done at a lower temperature, thus producing cold working of the material. We targeted processing temperatures well below the recrystallization temperature, as deformation at or above the recrystallization temperature would not permit the desired grain refinement and associated enhancement of strength. As will be shown below, already the first pass produced a high degree of grain refinement and the concomitant strength increase. Further

passes were then conducted in order to show the potential of the process and to determine how far we can drive the strength of the material. A staggered reduction of the processing temperature for the consecutive passes (P1 to P11) was used according to the following schedule: P1 250°C, P2 230°C, P3 210°C, P4 190°C, P5 170°C, P6 150°C, P7 130°C, P8 110°C, P9 90°C, P10 50°C. The 11th pass, P11, was conducted at room temperature (RT). The final rod diameter obtained after 11 passes was 13 mm, corresponding to a total true strain of 0.96. After being pressed, the rods were air cooled.

For microstructure and texture characterization, specimens were cut from a rod normally to its axis. The microstructure and the texture were observed in this plane (yz). The sections were mounted in epoxy, polished following the ASTM standard [62] and finally etched with a picric acid solution (5 mL acetic acid, 6 g picric acid, 10 mL distilled water, 100 mL ethanol) [63] for 5-15 seconds. The microstructure was observed in an optical microscope Olympus BX51M (Japan) and the uniformity of the sample was checked in terms of the variation of the grain size in radial direction, measured in 1 mm steps by the standard Mean Lineal Intercept method following the ASTM standard E112-96 [64]. The grain size was also measured by means of TEM observations using a JEM-2100 transmission electron microscope. Thin foils for electron microscopy were prepared by ion polishing with a GATAN 600 unit.

Texture analysis was carried out using X-ray diffraction in a DRON-7 goniometer with the Cok radiation in the reflection mode. Six incomplete pole figures, {00.4}, {10.0}, {10.1}, {10.2}, {10.3}, {11.0} were obtained with a step of 5° in the radial angle α and the azimuth angle β on a pole figure (maximum inclination angle $\alpha_{\max}=70^\circ$). The orientation distribution function (ODF), $f(g)$, was calculated from the measured pole figures presented as a superposition of a large number (1,000) of standard distributions with equal small scatter. Quantitative texture analysis was carried out on this basis.

The mechanical properties were characterized by means of tensile tests performed on flat tensile specimens having a gauge length of 18 mm, thickness of 2 mm and width of 4.8 mm. The specimens were machined along x-direction; their middle plane was contained in a section aligned with x-direction and located at a distance of about half of the rod radius from the centerline. Tensile tests were carried out on an Instron 5565 testing system at room temperature at a cross-head velocity of 0.5 mm/min, which corresponds to a nominal strain rate of $5.2 \times 10^{-4} \text{ sec}^{-1}$. An extensometer with a 16 mm gauge length directly attached to the samples was used to measure strain during the tests.

3.3 Results

3.3.1 Homogenization and microstructure analysis

Figure 3.2 presents optical micrographs of as-received and processed magnesium after 1, 6 and 11 passes of screw rolling. The as-received material is seen to have a uniform microstructure with a grain size of $43\ \mu\text{m}$. Already after a first pass at 250°C , it exhibited a clear grain refinement, as the grain size dropped significantly. The grain size was found to be non-homogeneous through the cross section of the billet, but a 4-5 mm thick outer rim (corresponding to the zone where the deformation was the most severe) presented a rather uniform structure with a grain size of 8-15 μm . After 6 and 11 passes the grain size dropped even further and had values of 5-6 μm and 2-3 μm , respectively. This corresponds to an overall grain refinement by a factor of about 20 after completion of processing. Figure 3.3 shows TEM micrographs of the material after 11 passes, providing a better insight in the grain structure at this stage. Grains seen in the micrograph have the size in the range of 1 μm to 3 μm , which is consistent with the data from the optical images.

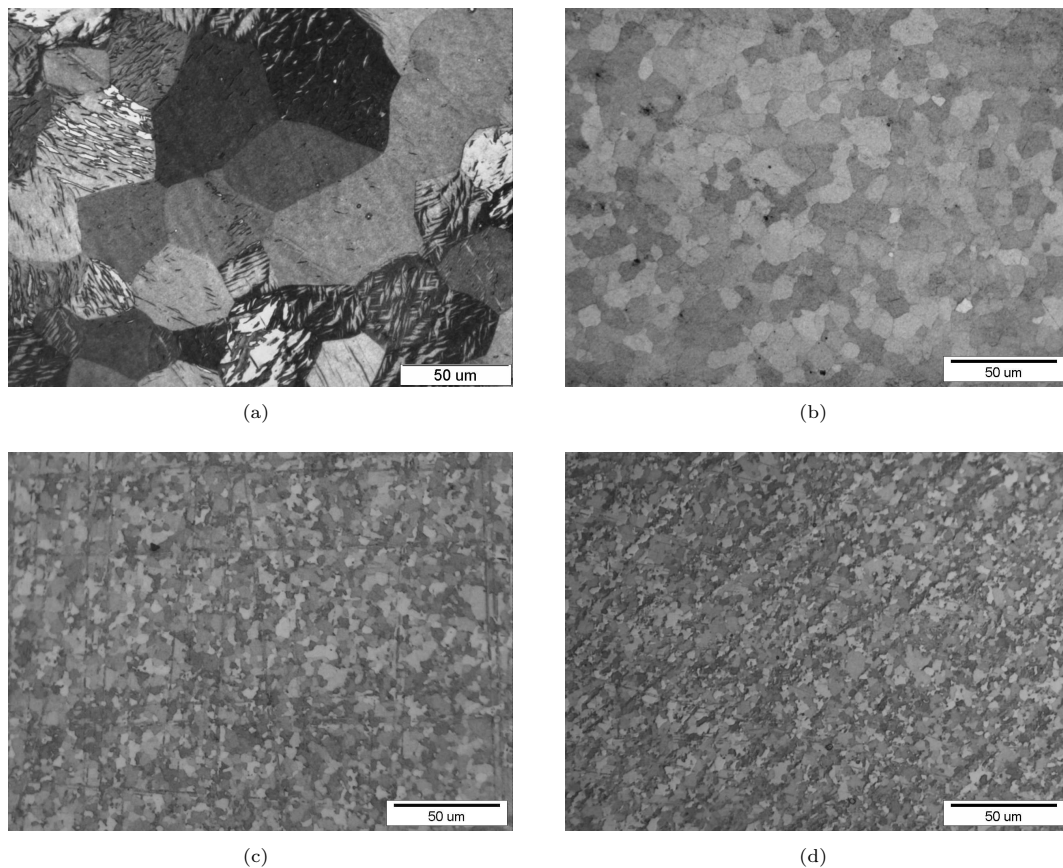


FIGURE 3.2: Microstructure of the pure magnesium rod (a) in the as-received condition and after (b) 1 pass (250°C), (c) 6 passes (150°C), and (d) 11 passes of PSW (RT), taken at half the distance between the center and the rim.

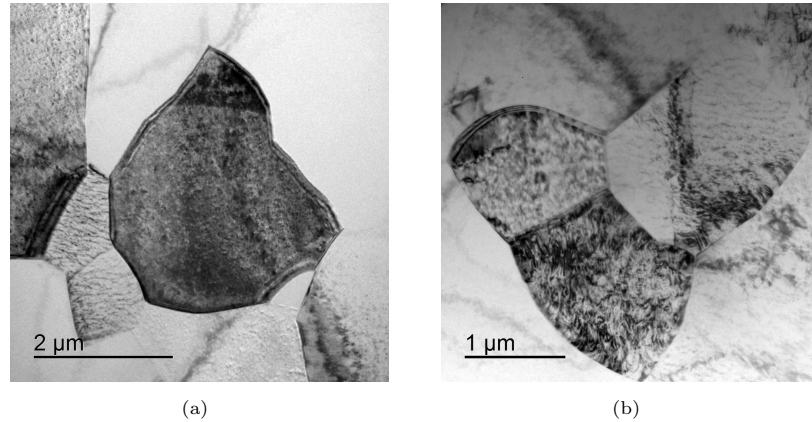


FIGURE 3.3: (a), (b) TEM micrographs of pure Mg structure after 11 passes of PSW taken at two different locations of the billet

The number of passes also affects the homogeneity of the billet. After one pass the microstructure, particularly the grain size, is rather non-uniform. The central part of the billet is less deformed than the outer regions, and a clear variation of the microstructure in the radial direction can be seen through the cross section from the central part to the periphery. Coarser grains are found in the middle part of the billet, while grains are more and more refined as the rim area of the sample is approached. However, with the increasing number of passes the microstructure is becoming increasingly homogeneous. Figure 3.4 shows the grain size distribution along the cross section of the billet after 1, 6 and 11 passes of screw rolling. A distinctly homogeneous structure can be seen after 6 and 11 passes.

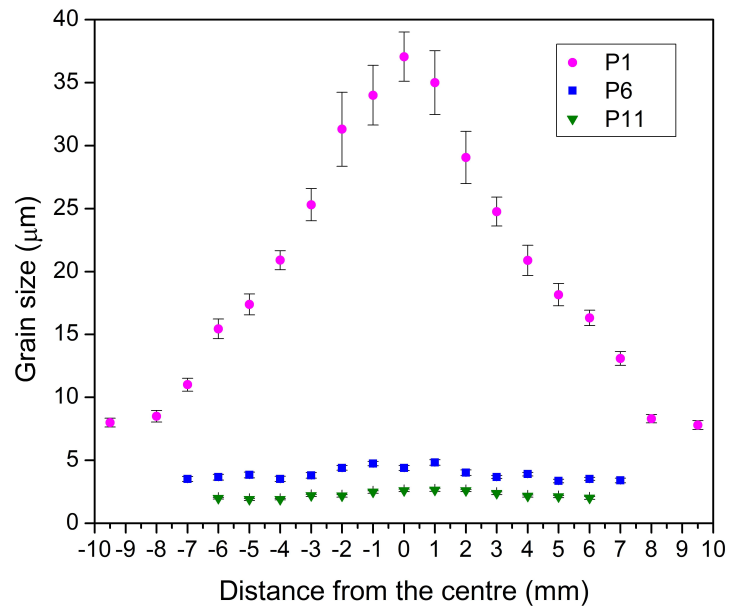


FIGURE 3.4: Grain size distribution along the diameter of the billet after 1, 6 and 11 passes of PSW.

The homogenization in the microstructure of materials processed by screw rolling has also been

highlighted in the case of pure copper and the rest of this paragraph is devoted to the study of copper. This work was done in collaboration with Monash University and all the results of this study can be found in [65]. Pure (99.9 wt%) Electrolytic Tough Pitch (ETP) copper rods with the diameter of 25.4 mm and the length of 150 mm annealed for two hours at 600°C were used in another study. Different numbers of passes of PSW were imposed on the billets at room temperature and micro-structural characterization and hardness measurements were carried out on these samples after 1, 3 and 6 passes. The microhardness distribution after one, three and six passes is shown in figure 3.5. The microhardness values were determined by averaging all the microhardness data at a certain distance from the center along the diameters of the samples and the error bars shown for each point correspond to the 95% confidence limits. Already after one pass a significant increase in microhardness was observed at the periphery of the sample. The value increased from $\approx 45.5 \text{ kgf/mm}^2$ for as received material to $\approx 115 \text{ kgf/mm}^2$ (not shown here) at the sample rim. In the central region of the sample the microhardness increment was lower, about 92 kgf/mm^2 . It should be noted that a stronger increase in microhardness was found in a region 4 mm away from the center. This significant increase in hardness is comparable to that reported for pure copper processed by two passes of Equal-Channel Angular Pressing (ECAP) [66]. These results indicated that further deformation of the sample did not affect the maximum microhardness, which remained the highest at the periphery of the sample, but did give rise to a further increase of the microhardness in the central region. Overall, it can be concluded that the microhardness rises with the number of PSW passes due to strain hardening and grain refinement strengthening until a saturation value of microhardness is reached.

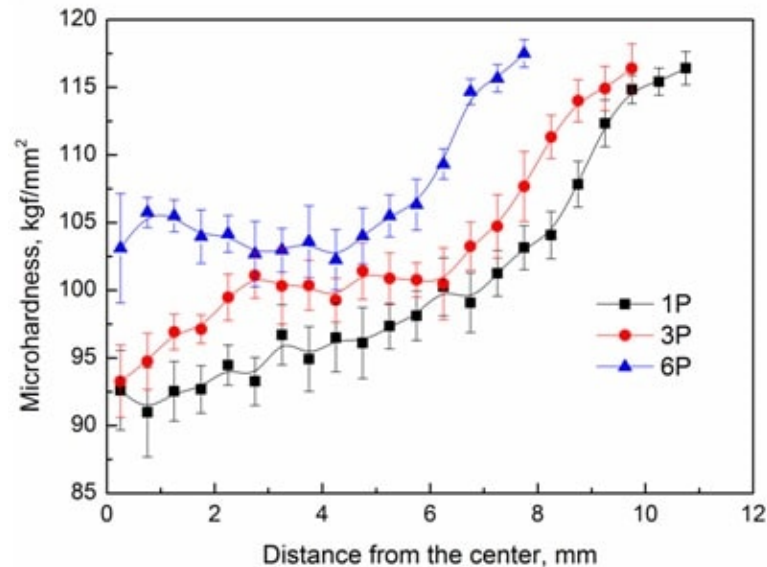


FIGURE 3.5: The microhardness distribution versus the distance from the center of the specimens processed by PSW after one, three and six passes.

The uniformity in the billet was also highlighted using numerical simulation of the PSW process

via finite elements. The processing of the copper rods was analyzed in that way and the distributions of the equivalent stress, the equivalent strain after processing, the hardness evolution and the temperature distribution in the billets were studied using the commercial software QFORM (QuantorForm). This package is specifically designed to simulate metal forming operations and uses an advanced approach which combines the advantages of Voronoi Cells and Finite-Element Methods. QFORM7 offers several benefits, such as the availability of automatic re-meshing and advanced algorithms for solving coupled mechanical and thermal problems, as well as an extensive database of industrial equipment and a materials database. The simulation of the PSW process of copper rod was set-up as a full 3D general forming simulation coupled with a thermal problem. The rollers were treated as non-deformable rigid bodies and were modeled as rotational drive with an axial speed of 120 rpm. The billet was pressed with a constant speed of 50 mm/s. The rollers and the billet were discretized using tetrahedral elements. The initial number of the elements of the billet was 3307, while each of the rollers was discretized with around 7000 elements. QFORM7 software utilizes automatic re-meshing algorithm which refined the mesh of the billet during the simulation in regions of higher deformation. After simulation of each pass, the deformation history was passed on to the subsequent simulation and the location of the rollers was adjusted to produce a reduction in diameter of the billet equivalent to the one obtained in the experiments. The simulations were conducted for room temperature conditions and it was assumed that the temperature history observed during one pass would not be passed on to the next pass, as adjustment of the rollers in the actual experiments allowed for cooling of the billet back to room temperature.

The hardness distribution over the cross section of PSW processed copper rods after 1, 3 and 6 passes is depicted in figure 3.6. After one PSW pass (Fig. 3.6(a)) a significant heterogeneity of microhardness distribution can be seen with the presence of a wide range of values, from 88 Hv in the centre of the billet and 120 Hv in the rim part. A careful inspection revealed three dark red colored sites corresponding to the maximum HV values, which were located nearly symmetrically about the axis of the rod at approximately 120° to each other. This arrangement is consistent with the contact between the rollers and the rod. These dark red colored zones with the maximum HV values expanded along the periphery of the sample with further straining of the sample (Fig. 3.6(b) and (c)). Application of additional two PSW passes resulted in the homogenization of the hardness distribution with most of the values included between 100 Hv and 108 Hv. The rim area gained no obvious expansion with increasing number of PSW passes, which is consistent with the variation in microhardness presented in figure 3.5. This confirms the mentioned trend to saturation in microstructure development and the concomitant saturation of HV values at the periphery of the sample. As can be seen, these color-coded maps are in good agreement with aforementioned radial distribution of microhardness shown in figure 3.5 and provide additional information about the evolution of the microstructure during the PSW process.

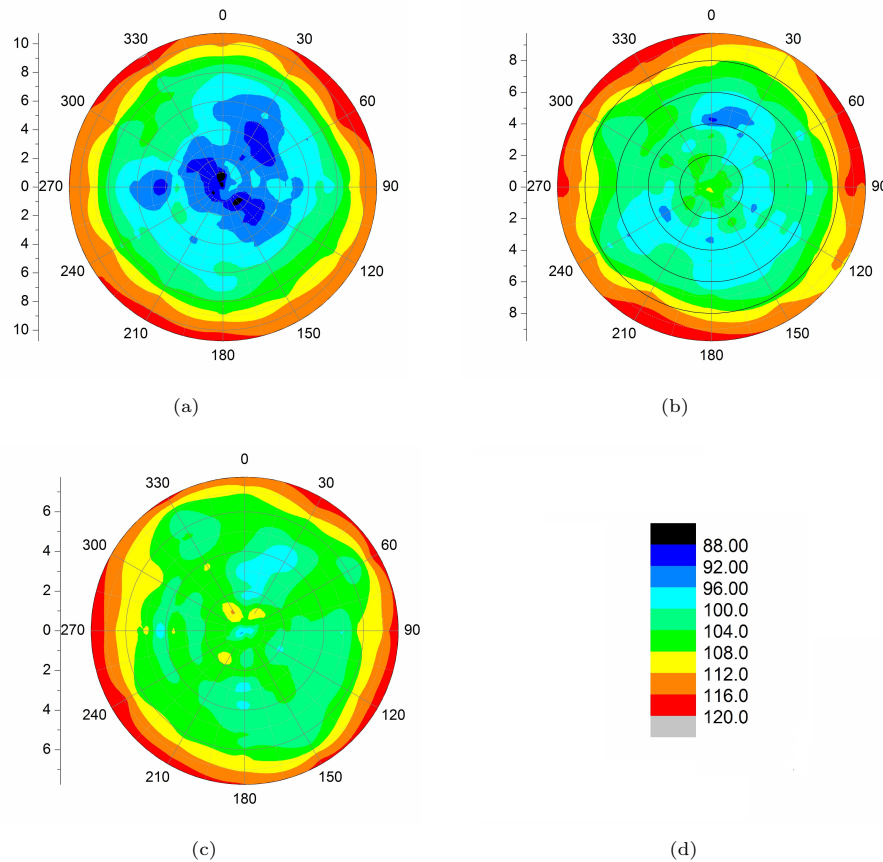


FIGURE 3.6: Color-coded contour maps showing the distribution of microhardness over the cross section of PSW-processed copper rods after (a) one, (b) three, and (c) six passes at room temperature. The color code shown in (c) corresponds to the microhardness levels of the rods.

3.3.2 Mechanical properties

The influence of the microstructure on the mechanical properties of pure Mg was studied in uniaxial tensile tests. The stress-strain curves obtained for pure magnesium before and after three-roll planetary milling are shown in figure 3.7. The as-received material exhibits a typical tensile stress-strain curve that can be found in literature [67, 68] with a yield strength value of 55 MPa and a strain to failure of 18%. After screw rolling the mechanical properties are improved greatly, with an increase in the yield strength (represented by the $\sigma_{0.2}$ proof stress) to 109 MPa and 116 MPa after 1 and 6 passes, respectively. A summary of the tensile properties is presented in a bar diagram in Figure 3.8. After 11 passes of the process employed, pure magnesium is seen to have acquired a remarkably high yield strength of 146 MPa, which is a value in the range of the yield strength levels of magnesium alloys. As an example, the yield strength of extruded AZ31 is about 200 MPa [69, 70], while that of a cast ZM21 alloy is 150 MPa [71, 72].

Concerning the tensile ductility a typical behaviour of materials processed by SPD is observed. From Fig. 3.8 it can be seen that the strain to failure decreases with the number of passes progressively. This is consistent with earlier observations. The strain to failure of the as-received

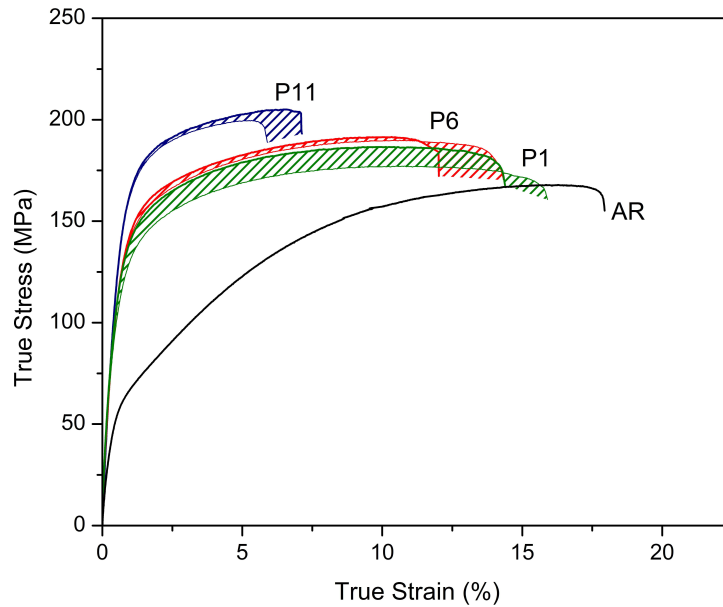


FIGURE 3.7: Tensile stress-strain curves of pure magnesium in the as-received (AR) condition and after 1 (P1), 6 (P6) and 11 (P11) passes of PSW.

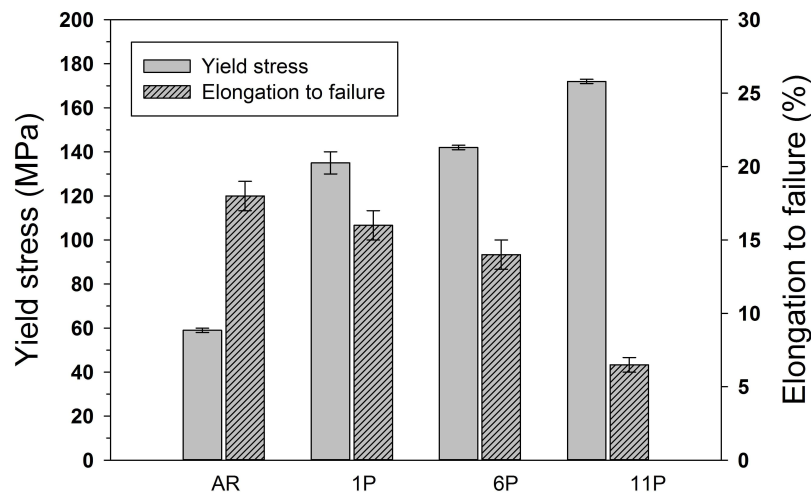


FIGURE 3.8: Summary of the values of the yield strength and strain to failure from tensile curves for as-received (AR) magnesium and after different numbers of PSW passes.

magnesium (18%) diminishes to 15% after the first pass and then decreases incrementally to 13% when the material has experienced 6 passes. After the 11th pass the material (while possessing excellent yield strength of about 146 MPa) shows brittle behaviour, the strain to failure dropping to a level as low as 7%. It is believed that premature failure in this condition is associated with the formation of micro cracks during screw rolling at room temperature during the 11th processing pass. The best performance data for our material are juxtaposed with literature data on SPD processed pure magnesium [3, 73, 74] in Table 3.1.

It should be mentioned that the material processed just once and the material that underwent 6 passes exhibit almost the same yield strength values (109 MPa and 116 MPa), although they

TABLE 3.1: Summary of work on improving the mechanical properties of pure Mg by SPD processing.

Source	Material	Process	Proof stress (MPa)	UTS (MPa)	Hardness (MPa)	Elong. to fail. (%)
This study	Extruded	PSW, 11P	146 (t.)	205 (t.)	-	7
G.D. Fan, 2012 [3]	Extruded	ECAP	145 (t.)	192 (t.)	-	27
J. Li, 2011 [73]	Cast	ECAP	112 (t.)	120 (C.)	-	8
S. Biswas, 2010 [74]	Extruded	ECAP	-	-	719.4	-

(UTS: ultimate tensile strength; (t.): tension; (c.) compression)

differ in grain size quite noticeably (8-15 μm after 1 pass (250°C) vs. 4-5 μm after 6 passes (150°C)). As this difference cannot be rationalized in terms of the grain size only, differences in texture are a natural suspect. Texture analysis presented in the following section sheds some light on this behaviour.

The $\sigma_{0.2}$ proof stress data presented in figure 3.9 as a function of the average grain size d corresponding to various deformation states of the material confirm that the common inverse square root Hall-Petch relation between the yield strength and the average grain size can be seen as fulfilled in a first coarse approximation. However, we would like to emphasize the mentioned fact that the grain size cannot be considered as a sole factor controlling the yield strength, as seen in particular when the data point P1 and P6 are compared.

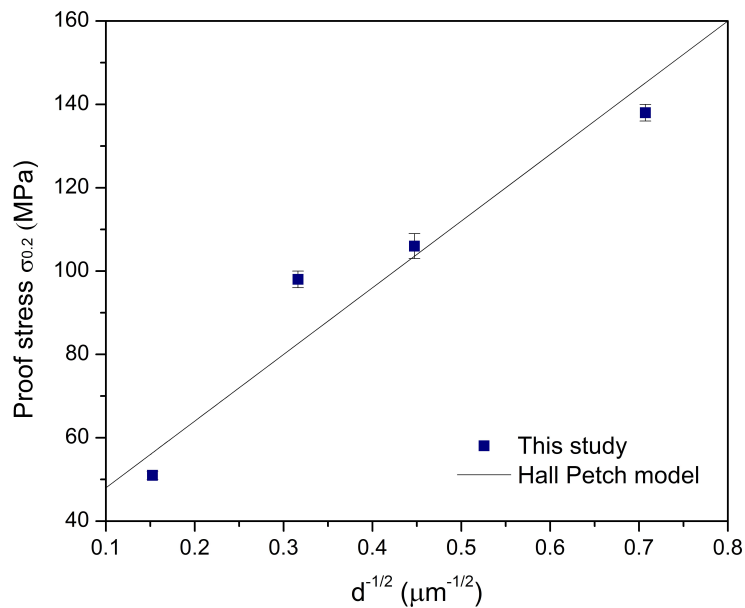


FIGURE 3.9: The Hall-Petch plot for Mg combining the $\sigma_{0.2}$ proof stress data for the as-received and the screw rolling processed samples.

3.3.3 Texture

As mentioned previously, texture analysis was carried out in terms of the ODF obtained from X-ray diffraction data. The ODF was approximated by a function defined in three-dimensional space of grain orientations g and is given by a weighted sum of 1000 standard functions, $f(g, g_i, \epsilon_i)$, corresponding to the texture components for ideal orientations [75]:

$$f(g) = \sum_{i=1}^N W_i f^s(g, g_i, \epsilon_i) \quad (3.1)$$

Here N is the number of the ideal grain orientations, labelled S , the weighting factor W_i is the volume fraction of the i -th orientation, g_i is the vector corresponding to its centre, and ϵ_i is a scatter parameter. Quantitative texture analysis based on the method of components yields the generalised Schmid factor:

$$m_i = \sum_{n=j}^p m_{ij} W_j \quad (3.2)$$

Here m_{ij} is the Schmid factor for the i -th slip system and the j -th texture component with a volume fraction W_j , and p is the number of texture components. The orientation Schmid factors for the basal and prismatic slip, M_b and M_p , are then obtained as an inverse of the respective generalised Schmid factor, m_b and m_p .

Figure 3.10 shows the pole figures taken from the cross-sectional plane normal to the x -direction of rods deformed by three different numbers of screw rolling passes. Six pole figures $\{00.4\}$, $\{10.0\}$, $\{10.1\}$, $\{10.2\}$, $\{10.3\}$, $\{11.0\}$ are presented for each deformed state, as well as for the as-received one. With regard to texture, the Mg rod in the as-received state can be regarded as nearly structureless. With increasing number of passes, and the concomitant decrease in deformation temperature, the formation of an axial prismatic texture, albeit a pretty scattered one, is suggested by the pole figures, especially the $\{00.4\}$, $\{10.0\}$ pole figures. ODF data in figure 3.11, with a value of φ_2 chosen to 40° , also confirm the development of texture with increasing number of passes. As it can be seen in figure 3.11 (a) the material had a relative random texture but after 6 passes the contours of the section were found at the bottom (fig. 3.11 (c)), corresponding to a (110) plane texture, as indicated in the theoretical section diagram in figure 3.11 (f). After 11 passes, the texture is even more pronounced. We note that as the volume fraction of the texture component associated with prismatic slip grows with the number of processing passes, that of the basal texture component declines. However, these variations in texture cannot be considered as very pronounced. Quantitatively, they are reflected in the values of the respective generalised Schmid factors. The information about the characteristic grain orientations and the generalised Schmid factor for the acting slip systems is summarised in

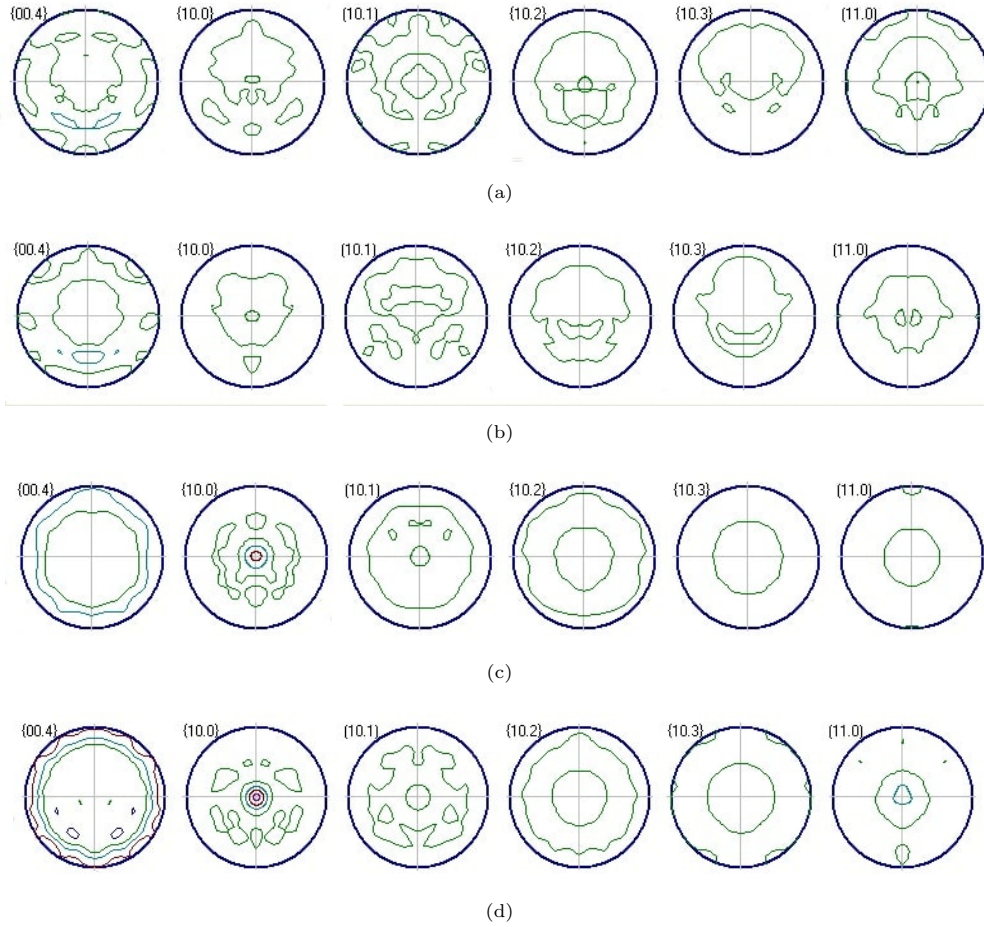


FIGURE 3.10: The X-ray pole figures $\{00.4\}$, $\{10.0\}$, $\{10.1\}$, $\{10.2\}$, $\{10.3\}$ and $\{11.0\}$ of pure magnesium (a) in the as received condition and after (b) 1 pass (c) 6 passes and (d) 11 passes of screw rolling.

Table 3.2. It is seen that with the number of processing passes (and the progressively decreasing processing temperature) the orientation factor for the basal slip goes up, while that for the prismatic slip goes down. This is a direct consequence of the increase of the volume fraction of prismatic texture. However, due to a large volume fraction of the structureless component (in excess of 80%) these variations in the orientation factors are rather mild. The fact that texture does not change that much during the three-roll planetary milling of Mg explains why the Hall-Petch relation seen in figure 3.9 is not violated due to interference of texture effects.

TABLE 3.2: The orientation factors for the different deformation systems in pure magnesium investigated.

	Basal	Prismatic
Initial state	4.909	5.831
After P1	4.898	5.731
After P6	5.607	5.434
After P11	5.933	5.283

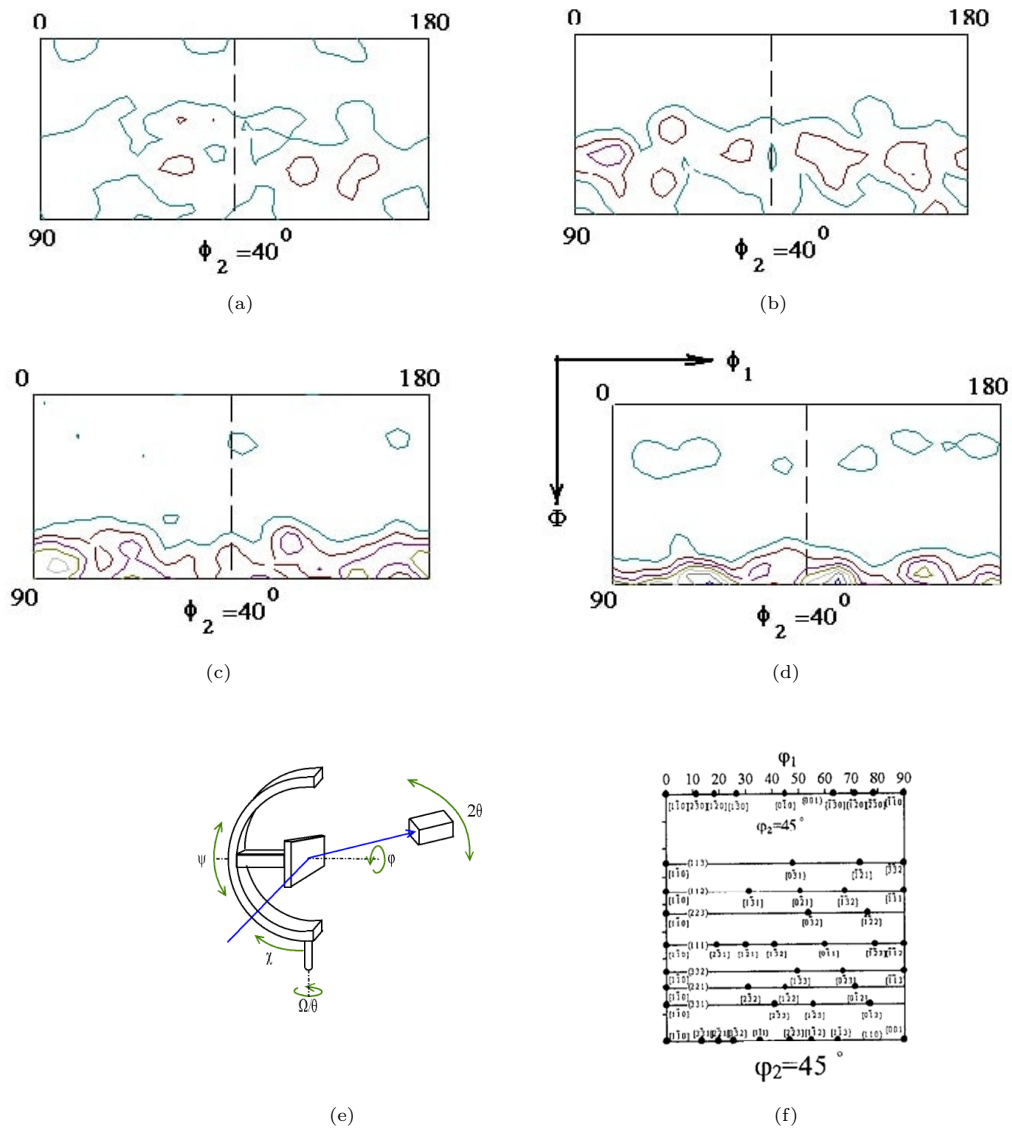


FIGURE 3.11: ODF sections for $\phi_2=40^\circ$ of pure magnesium (a) in the as received condition and after (b) 1 pass (c) 6 passes and (d) 11 passes of screw rolling. (e) Schematic of the XRD technique with Euler angles convention used here. (f) Theoretical texture diagram for $\phi_2=45^\circ$ was used to identify the obtained texture.

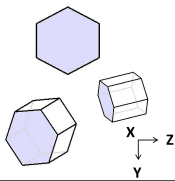
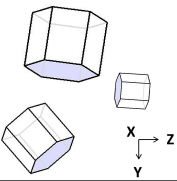
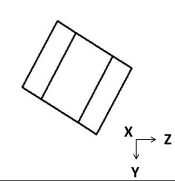
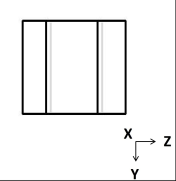
The overall picture of the evolution of the grain size and texture as a result of three-roll planetary milling that has emerged as a result of this study can now be summarized with the help of table 3.3 as follows:

- After the first processing pass (P1), the grain size drops appreciably, from $43 \mu\text{m}$ to $10\text{--}15 \mu\text{m}$, while the orientation factors hardly change. Hence the strengthening observed is largely controlled by grain refinement.
- Between the first and the sixth processing pass (P1 to P6), there is an increase of the orientation factor for basal and a drop of that for prismatic slip, which signifies a growing role of prismatic slip as a deformation mechanism. While this mildly pronounced texture

effect should lead to some decrease in the yield strength, it is outstripped by a more significant effect of grain refinement (from 10-15 μm to 5 μm), so that overall strengthening is seen.

- The passes P7 to P11 produce further grain refinement (from 5 μm to 2 μm) beyond that achieved by the preceding processing steps. Concurrently, the Taylor factor increases, so that the overall effect is that of strengthening.
- The evolution of texture, which is graphically illustrated in Table 3.3, is a result of increased activation of prismatic slip that tends to promote tensile ductility of Mg.
- However, the beneficial effects achieved after six processing steps appear to deteriorate with further passes, so that the processing schedule consisting in conducting just six screw rolling passes with staggered decrements in temperature (down to 150°) was identified as the best option.

TABLE 3.3: Summary of results in terms of texture, average grain size, yield strength and tensile elongation of magnesium in the as received (AR) condition and after 1, 6 and 11 passes of three-roll planetary milling.

	AR	P1	P6	P11
Texture				
Grain size (μm)	43	~10-15	~5	~2
$\sigma_{0.2}$ proof stress (MPa)	55	109	116	146
UTS (MPa)	167	177	191	205
Strain to failure (%)	18	15	13	7

3.4 Conclusion

In summary, three-point roll planetary milling was shown to be a technique well suited for producing grain refinement in magnesium. While the resulting structure is rather heterogeneous after one processing pass, it becomes more homogeneous as the number of passes increases. Grain refinement down to micron scale can be achieved with this technique. The observed texture evolution also plays a key role in the mechanical behaviour of the material, in terms of strength and ductility. The same range of yield strength (represented by the proof stress) of 109 MPa and 116 MPa was obtained after 1 pass and 6 passes respectively, while tensile ductility was significantly different in these two states, which is attributed to a specific combination of grain

size and texture. As the number of passes was further increased, while concurrently dropping the process temperature (ultimately to RT), the yield strength level of the order of about 146 MPa was reached. This value for pure magnesium, as well as the UTS in excess of 200 MPa, is comparable with strength levels for magnesium alloys. Figure 3.12 also shows that PSW technique can be well suited for the fabrication of magnesium bone grafts as the strength levels reached after 6 and 11 passes are similar with that of the cortical bone.

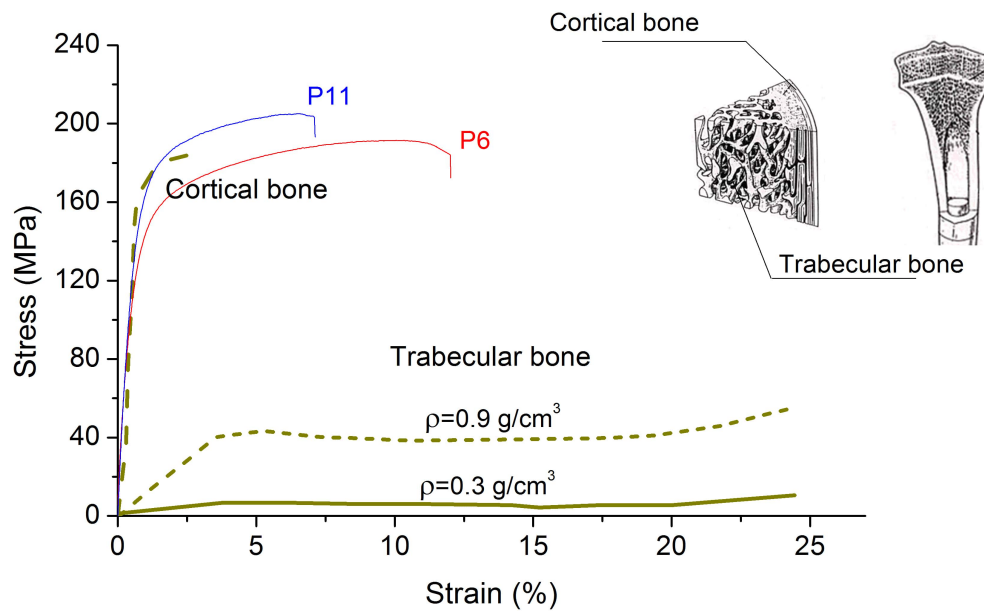


FIGURE 3.12: Stress strain curves of the cortical and trabecular bone as well as of pure magnesium acquired after 6 and 11 passes.

However, although the strain to failure after 11 passes is still higher than the one of the cortical bone, the brittleness of the material acquired as a result of 11 processing steps might be seen as an undesirable by-product. Hence, the optimum processing regime providing a good balance of strength and ductility should be limited to 6-pass screw rolling, with the temperature of the final pass being 150°C.

Overall, we can conclude that substantial grain refinement produced by three-roll planetary milling conducted in multiple steps with staggered reduction in temperature leads to a significant enhancement of strength. The concurrently developing texture associated with a moderate increase of the role of prismatic slip turns out to be conducive to strengthening and simultaneous increase of tensile ductility.

Chapter 4

Thermo-mechanical treatment of WE43 magnesium alloy to reach high strength for biomedical applications

4.1 Introduction

The results of the previous chapter have demonstrated that the PSW process can be used to significantly improve the mechanical behaviour of pure magnesium and of any metallic materials in general. However, in a search for a processing time reduction, the number of passes of screw rolling shall be decreased to its minimum. Six or eleven passes of PSW would be too much time consuming in an industrial context and cannot therefore be employed for the fabrication of implants. In this chapter we propose a new technique to improve the mechanical properties of magnesium and its alloys by considering only one step processing followed by a thermal treatment called ageing. Overall this technique is referred as to thermo-mechanical treatment (TMT) and provides high expectations as the combination of grain refinement, texture development during three roll planetary milling and the formation of hardening precipitates during ageing may lead to high levels of strength. The formation mechanisms of hardening precipitates during ageing are reminded in the literature review (chapter 2).

In this chapter, the attention was focused on magnesium alloys since they present higher mechanical properties than pure magnesium. Among them, AZ31, AZ91 and ZK60 have widely been studied in the last decades and stand for the most common magnesium alloys. However

these alloys are not of great interest when talking about medical applications as the elements they contain (aluminum, zinc or even copper and nickel) turn to be toxic for the human body and may provoke allergies or cancers. The new generation of biodegradable implants has to consider the use of pure magnesium only or non toxic magnesium alloys that could be tolerated by the human body without provoking post surgery reactions. Elements such as earth rare, zirconium, manganese and calcium could be tolerated in the human body and could therefore be introduced in small amount in the structure of implants. Among them, Mg-Y-Nd has received a lot of attention in the last years due to its good corrosion resistance and good biocompatibility. In particular, WE43 (4wt.% Yttrium, 3wt.% Neodymium) is considered as a promising candidate for biomedical applications and has been investigated in several studies involving in-vitro and in-vivo tests. Krause et al. [76] have for example implanted WE43 rods into the cavity of tibiae for a period of 6 months and only a moderate loss of volume was observed, from 0.125 cm³ to 0.082 cm³, showing a slow corrosion rate. Moreover, Witte et al. [18] suggested that the presence of rare earth elements decrease the oxidation rate of magnesium alloys.

4.2 Methods

The material used in this study was a cast WE43 magnesium alloy purchased from Yueyang Yuhua Yejin company (China) with a nominal composition of 4.51% Yttrium, 2.05% Neodymium, 0.31% Zirconium, 0.051% Calcium, 0.0117% Manganese and balance magnesium. The alloy was first homogenized at 525°C for 8h in an air furnace and subsequently pressed through the three roll planetary mill (also called PSW) at 400°C at a speed of 80 mm/sec. No lubricant was used. The processed material was then water quenched and aged at 210°C for 16h. The experimental procedure is illustrated in figure 4.1. Henceforth specimens solution treated at 525°C for 5 hours and water quenched will be referred as to ST ; specimens solution treated at 525°C for 5 hours, water quenched, screw processed at 400°C and quenched will be referred as to ST PSW400°C ; specimens solution treated at 525°C for 5 hours, water quenched, screw processed at 400°C, aged at 210°C for 16h and quenched will be referred as to ST PSW400°C Aged. In a second approach the number of PSW passes was increased up to three and the ageing time was set to different periods of time: 10min, 2h, 8h, 33h, 3 days and 7 days in order to perform a complete study and analyze the influence of each parameter on the strength of the material.

A study of the microstructure was performed in the cross section of the sample in order to investigate the grain size and the presence of twins in the specimens at different stages of their treatment. The sections were previously mounted in epoxy, polished following the ASTM standard [62] and finally etched with a picric acid solution (5mL acetic acid, 6g picric acid, 10mL distilled water, 100 mL ethanol) [63] for 5-15 secondes. The microstructure was then observed in an optical microscope Nikon Eclipse LV140 and the presence and the morphology of the second

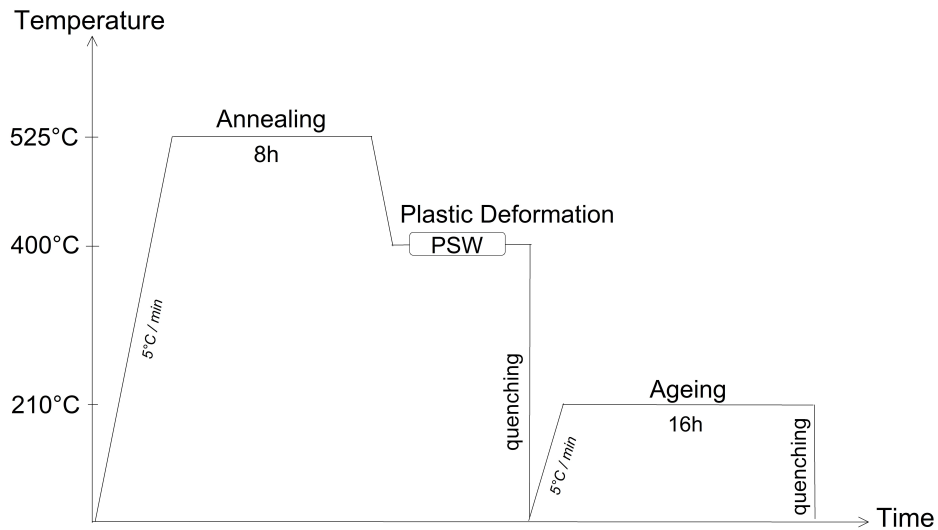


FIGURE 4.1: Schematic illustration of the experimental procedure used in this study.

phase was revealed using the JSM-5600 Scanning Electron Microscope (SEM) equipped with an Energy Dispersive Spectroscopy (EDS). The initial analysis of the phase composition of the material was examined by X-ray diffraction (XRD, D8-Advance; Bruker, Germany).

Texture analysis was carried out using X-ray diffractometer Xpert Pro. Three pole figure, (101), (002) and (100) were obtained with a step of 5° in the radial angle α and the azimuth angle β on a pole figure. The orientation distribution function (ODF) was calculated from the measured pole figures presented as a superposition of large number of standard distributions with equal scatter.

The mechanical properties were characterized by means of tensile tests performed on flat tensile specimens having a gauge length of 18 mm, thickness of 2 mm and width of 4.8 mm. In total 15 specimens machined along the longitudinal axis and from 3 different processed rods were tested in each case. They were machined along the longitudinal axis. The tensile tests were carried out on an Instron 5582 testing system at room temperature at a constant cross-head velocity of 0.5 mm/min. An extensometer with a 16 mm gauge length directly attached to the samples was used to measure strain during the tests.

Microhardness measurements were performed using a Duramin A-300 hardness tester equipped with a diamond pyramidal indenter. For each data point a load force of 1 kg and a holding time of 15 seconds were applied. To achieve the hardness distribution along the diameter of the billet, indentations were made on their radius and their exact position revealed by microscope observation.

In order to study the structure, morphology and phase of the hardening precipitates, transmission electron microscopy JEM-2100F (TEM) was used with accelerating voltage of 200 kV. Thin foil was obtained for the TEM observation after the specimen has been conventionally ion

milled through a FIB SMI3050SE system. Bright field images as well as diffraction pattern were obtained. Indexing of the diffraction patterns was carried out by measuring the lattice parameters (distances and angles) between each spot using the software Gatan Digital Micrograph and by comparing the results to theoretical diffraction patterns observed in different zone axis (the theoretical diffraction patterns can be found in appendix B).

Finally, since materials processed by SPD were reported to present higher corrosion resistance than in the initial conditions owing to formation of an oxide layer playing the role of a protective barrier, it was decided to carry out in vitro tests on processed WE43 to characterize its corrosion behaviour. The samples were immersed into simulated body fluid (SBF) for 90h with a pH of 7.4 and ion concentrations nearly equal to those of human blood plasma. The pH of the solution was monitored using a pH meter (sp-701; Suntex, Taiwan). In addition, potentiodynamic tests were performed using a potentiostat/galvanostat (Model 273, EG Princeton Applied Research) in the SBF at 37°C.

4.3 Results

4.3.1 Initial cast Mg-Y-Nd alloy

The microstructure of the as-cast WE43 alloy is shown in figure 4.2. It consists of solid solution α -Mg matrix (point 1, Fig.4.2(b)) with second phase located at the grain boundaries. An EDS analysis performed on the initial microstructure with three measurement points revealed the phase composition of the alloy (the results are presented in table 4.1). It can be noted that the Mg matrix does not contain a large amount of zirconium as it was found in some previous studies [77]. Y-rich phase appears as the bright and continuous network surrounding the grains (point 2, Fig.4.2 (b)) while the dispersed Nd-Y rich phase can be seen in the form of white precipitates with a size of several microns (point 3, Fig.4.2 (b)) located at the grains boundaries. The composition of these precipitates was previously reported as Mg_2Y [78]. In order to analyze more in details the chemical composition of the alloy, phase identification was carried out by X-Rays diffraction (XRD). Figure 4.3 displays the X-rays diffraction pattern of cast WE43 in which diffraction lines were identified arising from different phases. Alpha-Mg matrix phase was associated with the high peaks while the second phase was associated with the peaks of lower intensities. By comparing the 2-theta values of these peaks with the values from the literature [79], it seems that WE43 is composed of two phases $Mg_{24}Y_5$ and $Mg_{41}Nd_5$.

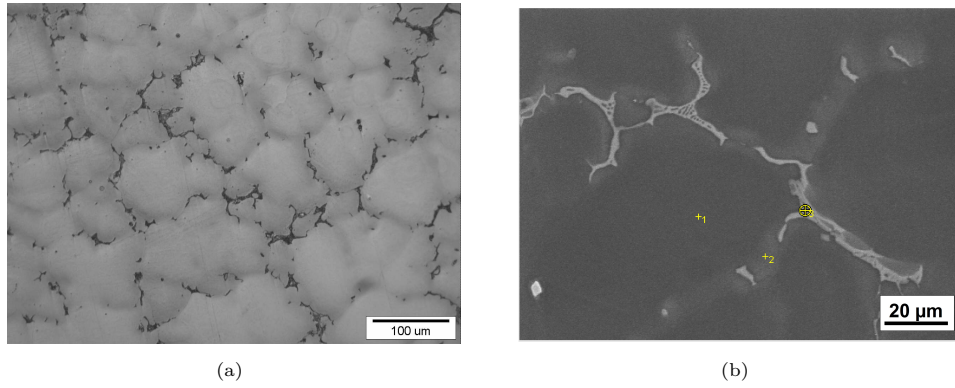


FIGURE 4.2: Microstructure of the cast WE43 (a) at low magnification and (b) at high magnification using SEM technique to clearly reveal the second phase particles.

TABLE 4.1: EDS results of as cast WE43 alloy of figure 4.2.

Point	Mg (at.%)	Y (at.%)	Nd (at.%)	Zr (at.%)	Phase
1	99.3	0.37	0.06	0.27	α -Mg
2	96.3	2.5	0.47	0.23	Y-rich
3	90.78	4.61	4.39	0.22	Nd-Y-rich

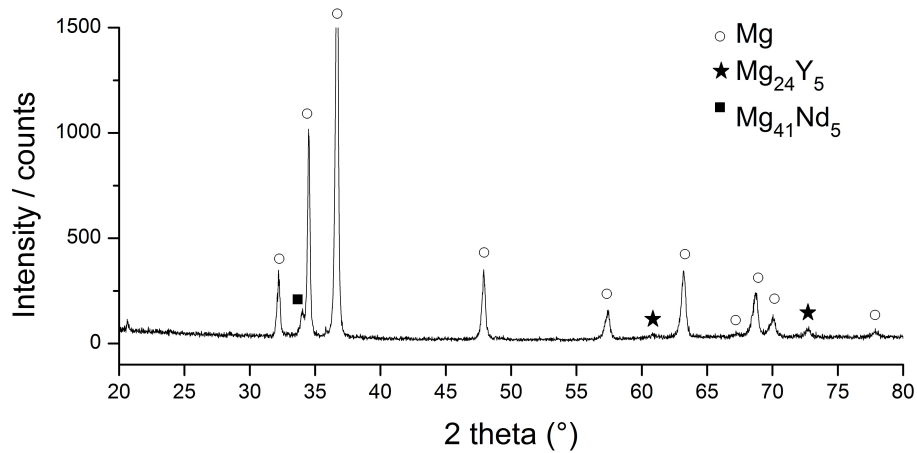


FIGURE 4.3: X-rays diffraction pattern of the cast WE43 and the phases associated with the peaks.

4.3.2 Mechanical properties

The mechanical properties of cast WE43 and TMT processed WE43 magnesium alloy were characterized by the mean of tensile tests and hardness measurements. Figure 4.4 depicts the strain stress curves of WE43 magnesium alloy in its cast condition and after each step of the thermo-mechanical treatment. It can be seen that the initial material exhibits a yield strength value of 140 MPa and a strain to failure of about 8%. After annealing at 525°C for 8h the ductility was greatly improved with an increase of the strain to failure to 15±1%, as a typical

reaction to heat treatment. No change of yield strength was observed. After one pass of screw rolling at 400°C, the mechanical properties of the material remarkably increased as indicated by the arrow on figure 4.4 (PSW effect) with yield strength reaching a value of 220 ± 20 MPa. Concerning the tensile ductility a typical behaviour of materials processed by SPD was observed after one pass processing as the strain to failure decreased to $6.5\pm 2\%$, almost in the same range than the initial material. The scatter band highlights the non homogeneity in the processed billet with the upper tensile curve corresponding to the behaviour of the rim area and the lower curve corresponding to the behaviour of the central area of the billet. Finally, after ageing at 210°C for 16h, WE43 alloy acquired very high yield strength of 280 ± 10 MPa and relatively good ductility with a strain to failure of $5\pm 1.5\%$.

Figure 4.5 illustrates the microhardness distribution of the as cast material and after each step of the thermo-mechanical treatment. No significant change was observed in the hardness after annealing compared to in the initial conditions, with a similar value of about 65 ± 5 Hv, uniformly distributed in the billet. However, after one pass of PSW a clear heterogeneity appeared in the billet as the microhardness increased drastically to ≈ 100 Hv at the periphery of the sample but remained roughly the same at its center. This result is in good accordance with the tensile curves obtained for WE43 after one pass of PSW where a large scatter band was observed, indicating a non homogeneity in the billet. These results also correlate the experiments performed with pure magnesium in chapter 1 in which a clear tendency was shown between the number of passes and the homogenization of the billet. Ageing the alloy at 210°C for 8h resulted in an increase of the microhardness in the central region with values of 88 ± 4 Hv but did not give rise to a further increase at the periphery of the sample, where microhardness remained the highest with values of about ≈ 100 Hv. This result has already been observed in copper processed up to 6 passes by PSW where a saturation in hardness was found at the periphery of the sample [65].

4.3.3 Influence of the number of passes

In order to evaluate the influence of the number of passes on the mechanical properties of WE43, it was chosen here to process the rod sample up to three times. Although this procedure would not be suitable for the fabrication of implants due to its time consumption, this approach brings new information as for the optimum conditions to reach high mechanical strength. As illustrated in figure 4.6 the experimental procedure was very similar to the previous one, with three steps processing (annealing, plastic deformation and ageing). However, the WE43 rod was here subjected to 3 passes of screw rolling then quenched and ageing at 210°C for 16h. After each pass the rod sample was placed inside a furnace and heated at 400°C for 30 min in order to guarantee similar conditions and same temperature processing for the three passes. Tensile

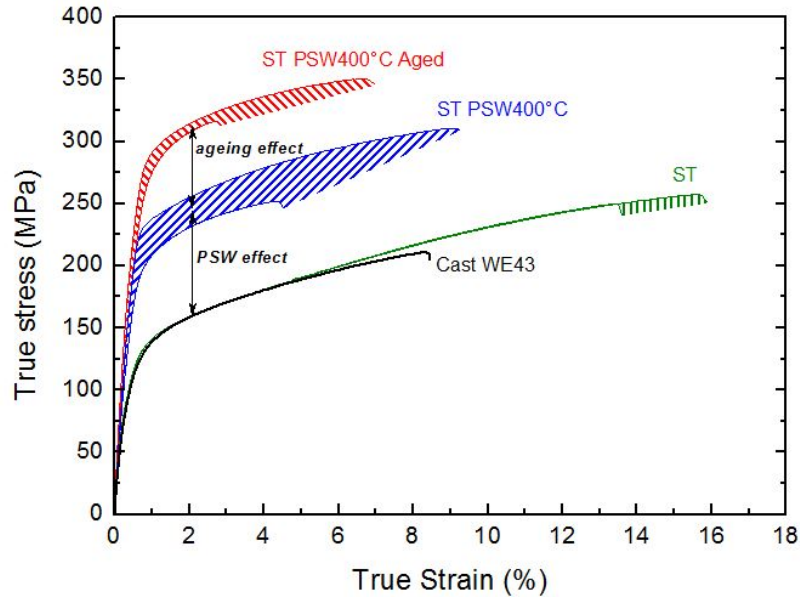


FIGURE 4.4: True stress-strain curves for magnesium WE43 alloy in the cast condition and after each step of the thermo-mechanical treatment. The scatter area refers to the non homogeneity of the samples.

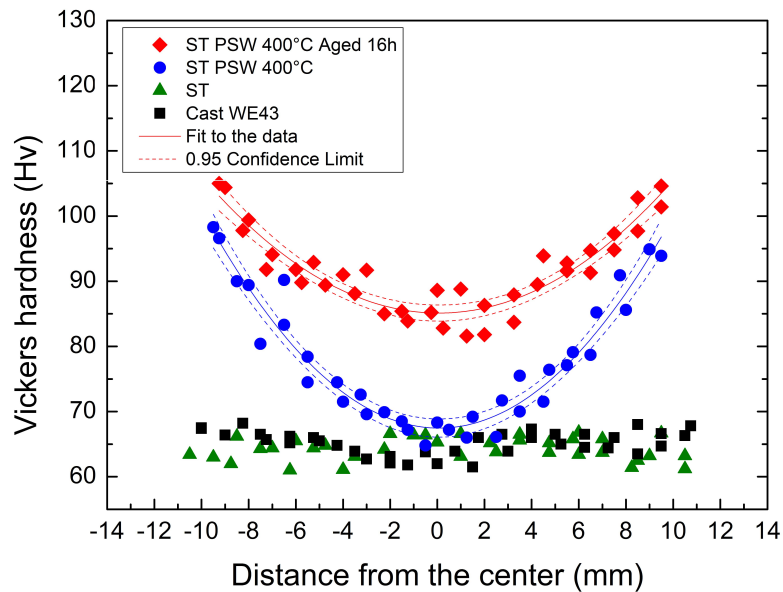


FIGURE 4.5: Vickers hardness distribution versus the distance from the center of the cast, ST, ST PSW400°C and ST PSW400°C Aged WE43 specimens.

tests and hardness measurements were carried out after each pass on aged and non-aged samples. This new experimental procedure only concerns section 4.3.3.

Figure 4.7 depicts the strain-stress curves of WE43 magnesium alloy after 1, 2 and 3 passes of PSW before and after ageing. When the alloy is only subjected to annealing and plastic deformation (fig. 4.7 (a)) it can be seen that the yield strength (YS) increases as a function of number of passes, as already observed in chapter 3. The alloy exhibits a YS of about 207

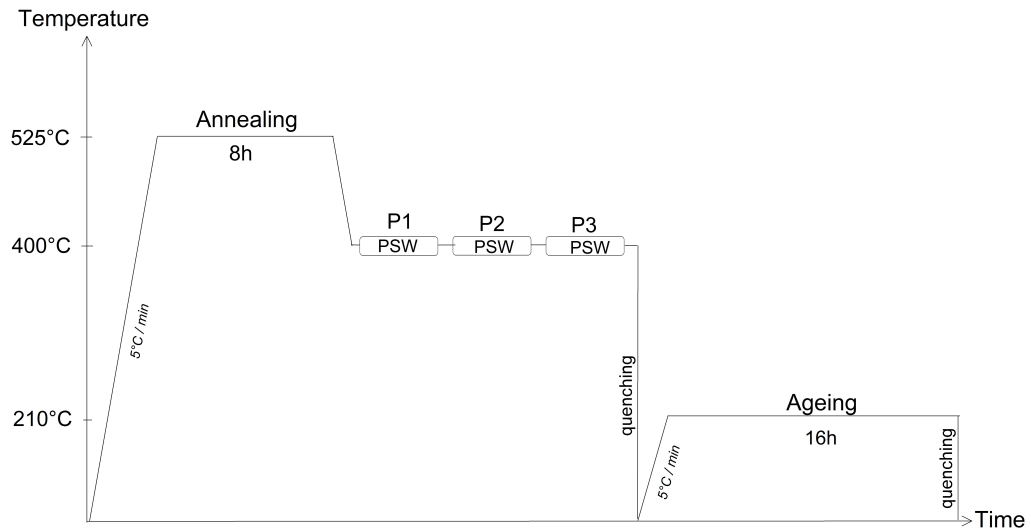


FIGURE 4.6: Modified version of the previous experimental procedure. In this section WE43 alloy was subjected to three passes of PSW process and aged in order to determine how far the strength of the material can be driven.

MPa, 225 MPa and 245 MPa after 1, 2 and 3 passes respectively. Moreover, the strain to failure decreases from about 10% after 1 pass to about 6% after 2 and 3 passes of PSW as a typical behaviour of materials processed by SPD. We would like to make the comment that these values correspond to an average value observed in an area located between the rim area and the central region of the billet. The strength of the alloy after ageing treatment is shown in figure 4.7 (b). While the yield strength of the alloy was greatly improved after ageing the 1-pass sample, it was observed that increasing the number of passes up to 2 and 3 had a moderate effect on the strengthening of the material during ageing treatment. The yield strength in the billet subjected to 2 passes of PSW was quite similar before and after ageing, with values of 225 MPa and 240 MPa respectively. The same trend was observed in the billet processed 3 times.

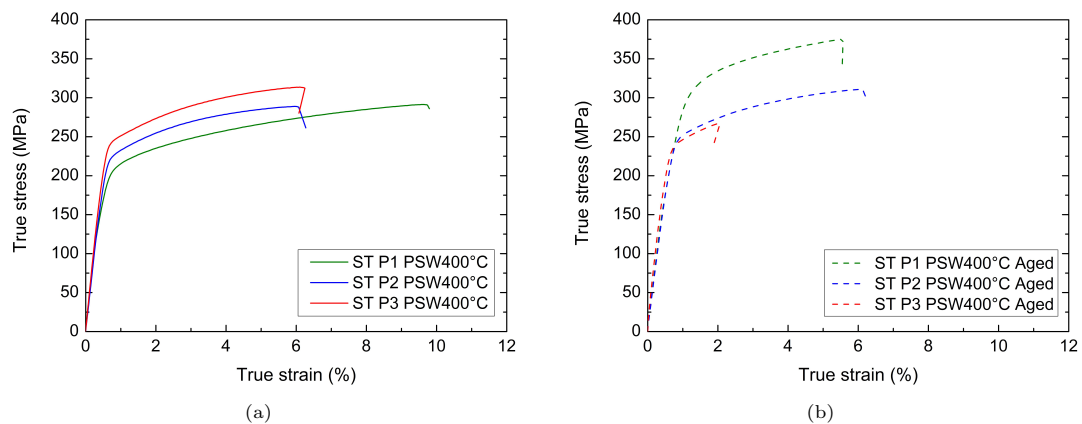


FIGURE 4.7: Tensile strain stress curves of WE43 magnesium alloy after 1, 2 and 3 passes of PSW at 400°C (a) without and (b) with subsequent ageing treatment at 210°C for 16h.

In order to confirm the previous observation, micro-hardness measurement was performed with

samples subjected to 1, 2 and 3 passes of PSW, before and after ageing treatment. The hardness distribution in figure 4.8 (a) confirms that the mechanical properties of the material increases with the number of passes of screw rolling, with a more severe effect observed at the rim area of the samples. However, when the PSW processed samples were aged at 210°C for 16h, it can be seen that the highest hardness values were found after 1 pass, with values of 92 Hv in the central area of the billet. The 3-pass processed and aged sample exhibited much lower values of 77 Hv in the same area which corroborates the previous results of the tensile tests. Therefore it can be concluded that increasing the number of passes of screw rolling leads to an enhancement of strength but a further ageing treatment is not effective in promoting strengthening to the multi-passes processed material. Thus, the best option to reach high mechanical properties seems to consist in performing a thermo-mechanical treatment to WE43 with 1 pass processing only. This is the condition we used for the rest of the study.

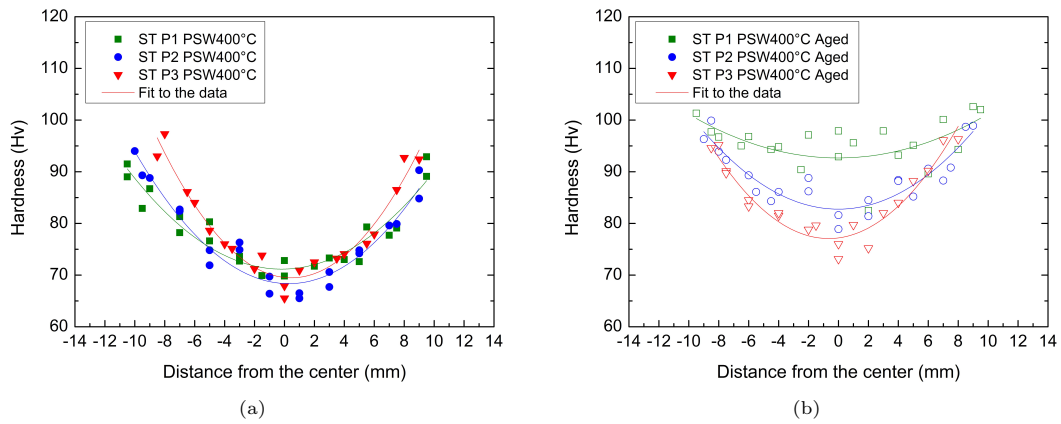


FIGURE 4.8: Hardness distribution in WE43 magnesium alloy after 1, 2 and 3 passes of PSW at 400°C (a) without and (b) with subsequent ageing treatment at 210°C for 16 hours.

4.3.4 Microstructure evolution

4.3.4.1 Grain size evolution

The influence of the microstructure on the mechanical properties of WE43 magnesium alloy was studied by measuring the average grain size of the sample after each step of the thermo-mechanical treatment, ST, ST PSW400°C and ST PSW400°C aged, in order to validate or not the famous Hall-Petch relation. The grain size was determined by averaging all the grain size data measured in 2 mm step along the diameter of the samples by the standard mean lineal intercept method. The grain size of the alloy in the initial cast condition is seen to have a uniform microstructure with a grain size of about 63 μm as shown in figure 4.9. After solution treatment it exhibited a slight grain growth, as the grain size increased to about less than 80 μm uniformly across the section, which is a typical reaction to heat treatment. After one pass of

PSW the billet was found to be non homogeneous through the cross section of the billet although the difference in grain size between the rim area and the center of the sample was not found to be as pronounced as in the case of one pass processed pure magnesium. Indeed, after deformation the average grain size had values of about $73 \mu\text{m}$ at the center and $58 \mu\text{m}$ at the rim area of the sample which correspond to a very slight grain refinement compared to the initial microstructure of the cast WE43 alloy. An additional heat treatment (ageing) at 210°C for 16h resulted in a remarkably high grain growth with grain size reaching more than $110 \mu\text{m}$ at the center of the billet and about $90 \mu\text{m}$ at the edge. It is believe that such a fast and important grain growth occurred due to the release of energy accumulated into the grains during plastic deformation. Therefore, from the results of figure 4.4 and figure 4.9, it can be seen that ST PSW 400°C Aged sample presents very high mechanical properties with 0.2% proof stress value of about 280 MPa and a coarse microstructure with grain size ranging more than $100 \mu\text{m}$, invalidating the common the inverse square root Hall-Petch relation between average grain size and yield strength. Such a coarse microstructure and the very small grain refinement observed after one pass of screw rolling cannot explain the occurrence of high mechanical properties. Therefore, and because the grain size cannot be considered as a sole factor controlling the yield strength, a texture analysis must be carried out to provide additional information about the microstructure evolution during the processing of WE43.

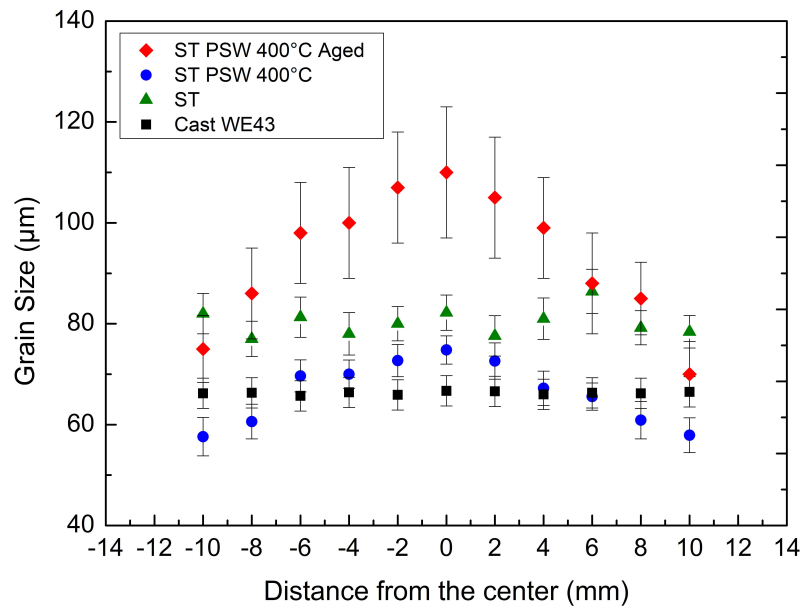


FIGURE 4.9: Grain size evolution versus the distance from the center of the ST, ST PSW 400°C and ST PSW 400°C Aged WE43 specimens

4.3.4.2 Optical images

Figure 4.10 shows the microstructure evolution in ST PSW 400°C Aged specimen, with optical images taken at the center (a), at half the radius (b) and at the rim area of the sample (c). As

previously illustrated by the grain size evolution in the cross section of the billet, coarse grains of about $100\ \mu\text{m}$ were found in the central region of the billet while smaller grains of about $90\ \mu\text{m}$ were observed at the periphery of the specimen (area that receives the highest deformation rate). More interestingly, twins could be seen in the interior of the grains of the aged alloy. They clearly appear in figure 4.10 (a) and in figure (b) and (c) as the black lines inside the grains. These twins are believed to appear during the plastic deformation of the alloy since they were already observed after one pass of PSW (not shown here). A close look at figure 4.10 reveals a clear twin concentration distribution across the billet with a very small twin density in the central region and a high twin density at the periphery of the sample that experienced the highest strain. This result confirms again the significant heterogeneity in the magnesium sample after processing and ageing.

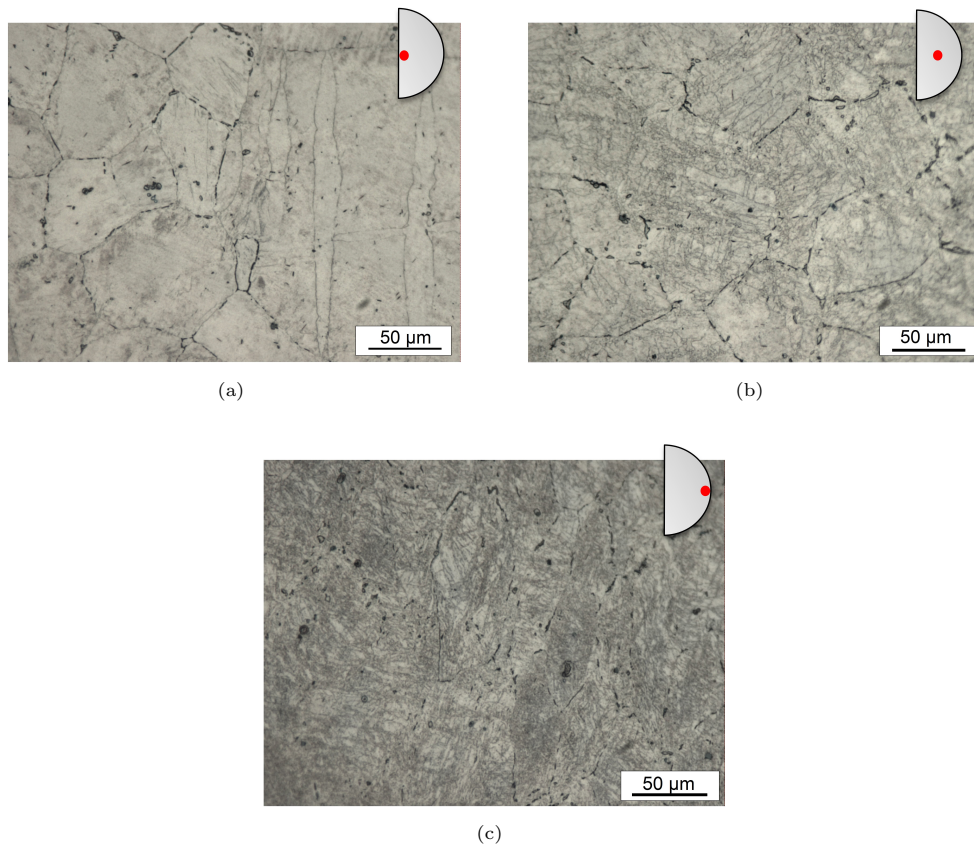


FIGURE 4.10: Optical images of the microstructure of WE43 magnesium alloy after annealing, 1 pass of PSW and ageing taken at different location over the cross section area of the sample (a) in the central region (b) at half radius (c) at the periphery of the sample

4.3.4.3 EBSD images

The microstructure evolution in the ST PSW400°C and ST PSW400°C Aged samples was also analyzed by the mean of Electron Backscatter Diffraction (EBSD). Figure 4.11 (a), (b) and (c)

show the microstructure of the ST PSW400°C sample while figure 4.11 (e) and (f) depict the microstructure of ST PSW400°C Aged sample. All the microstructure analysis was performed in an area located in between the center and the rim part of the billet. Colors on the maps correspond to the texture components as indicated in figure legend 4.11 (d). After deformation by the PSW process it can be seen that the material exhibited a high fraction of high angle grain boundaries (HAGB) as indicated in figure 4.11 (b) where red lines refer to HAGB ($\theta \geq 15^\circ$) and blue lines to LAGB ($\theta \leq 15^\circ$). The misorientation distribution (not shown here) revealed a fraction of HAGB of about 88%, which is comparable with friction-stir-processed (FSP) WE43 [80]. Although the EBSD analysis could not be done in a large scale (only one grain is represented here) it seems that some grains had their basal plane (0001) parallel to the extrusion direction Z, in other words c axis basal plane [0001] perpendicular to the extrusion direction Z, as represented by the green color in figure 4.11 (c). This grain orientation promotes strengthening of the material. Arrows in figure 4.11 (c) also highlight twins introduced during screw rolling of the alloy, as previously mentioned, with a change of color that indicates the occurrence of twins with a crystal orientation such as represented in the figure. After ageing the alloy at 210°C for 16h (ST PSW400°C Aged), no significant variations occurred in the microstructure. Figure 4.11 (d) depicts the distribution of LAGB and HAGB through an area located between the center and the rim of the aged WE43 alloy. It was seen that 89% of the grains had HAGB, in a quite similar way than the processed material ST PSW400°C. Therefore, ageing treatment does not seem to influence the fraction of HAGB, which allows to maintain strength in the last step of the treatment of the alloy due to their faculty to impede dislocation movements. The texture analysis in the same area is shown in figure 4.11 (f). Like in the processed sample, twins appeared in the microstructure as indicated by the tones of blue and white corresponding to (10 $\bar{1}$ 0) and () texture components, respectively. Although EBSD analysis provided precious information regarding the occurrence of twins and the presence of HAGB, no conclusion can be drawn as for a texture development during TMT treatment. A bigger sample area containing more grains should rather be analyzed.

4.3.5 Texture

The texture evolution was examined by an XRD analysis and the results are presented in figure 4.12 where the XRD patterns are shown for, from bottom to top, the WE43 alloy in the cast condition, after annealing (ST), after PSW processing (ST PSW400°C) and after ageing (ST PSW400°C Aged). The analysis was performed with a limited 2θ angle of 20°-60° and (100) prismatic plane, (002) basal plane, (101), (102) and (110) pyramidal planes were visible for all tested specimens. Moreover, only Mg₄₁Nd₅ phase of WE43 alloy could be seen in that range of angle, as previously shown in figure 4.3. It can be observed that as-received cast magnesium alloy had the highest peak intensity on the (101) pyramidal plane which is consistent with the results

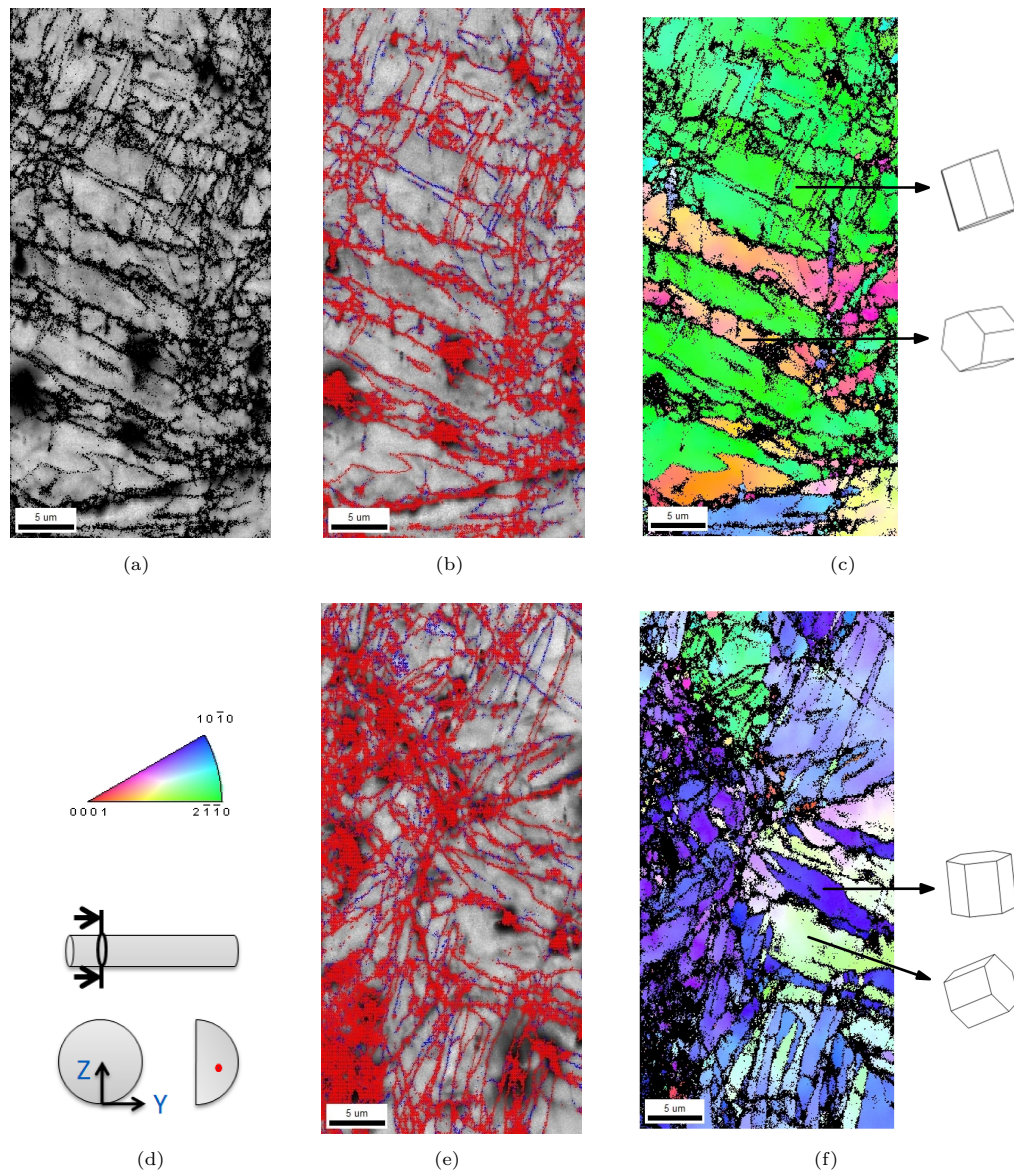


FIGURE 4.11: (a) Microstructure, (b) EBSD map showing the boundaries distribution and (c) EBSD map showing the texture components of WE43 magnesium alloy after annealing and one pass of screw rolling (ST PSW400°C). The color-coded key as well as the sample geometry are indicated in (d). The boundaries distribution and texture components of WE43 alloy after ageing (ST PSW400°C Aged) are illustrated in (e) and (f), respectively.

of K. Yu et al [81] and T. Rzychon [79]. After annealing, the sample was in a super saturated solid solution (SSSS) with the second phase dissolved into the matrix and therefore only the α -Mg peaks appeared in the XRD pattern with peaks of relatively same intensity, resulting in a quite random texture. However, a strong texture development was observed after one pass of PSW process with very high peak intensity on (100) and (101) planes and almost no peak intensity on the (002) basal plane which corresponds to the crystal orientation represented in figure 4.11 (c) (green color) where c axis basal plane [0001] was perpendicular to the extrusion direction Z. This result is consistent with conclusions of chapter 3 in which an increase of volume

fraction of texture component associated with prismatic planes and a decrease of basal texture component were found in pure magnesium processed by screw rolling. The non existence of peaks on basal planes also corroborates the crystal orientation shown in the EBSD image of ST PSW400°C sample, promoting strengthening of the material. Moreover it can be seen that the small peak associated with the second phase $Mg_{41}Nd_5$ appeared again in the XRD pattern indicating a possible precipitation of the second phase from the SSSS due to the decrease of temperature from 525°C to 400°C. Since no significant grain refinement occurred after one pass of PSW process (cf. figure 4.9) and the Hall Petch relation was not fulfilled, it is believed that the big change of texture observed in the ST PSW400°C XRD pattern plays the main role in the increase of strength of the material due to a shift from a random texture to a (101) aligned texture. Finally, after ageing treatment, no significant variations in the XRD pattern was observed with peaks on (100) prismatic and (101) pyramidal planes remaining the ones with highest intensity, although the intensity of (110) peak is almost as high as the one of (100).

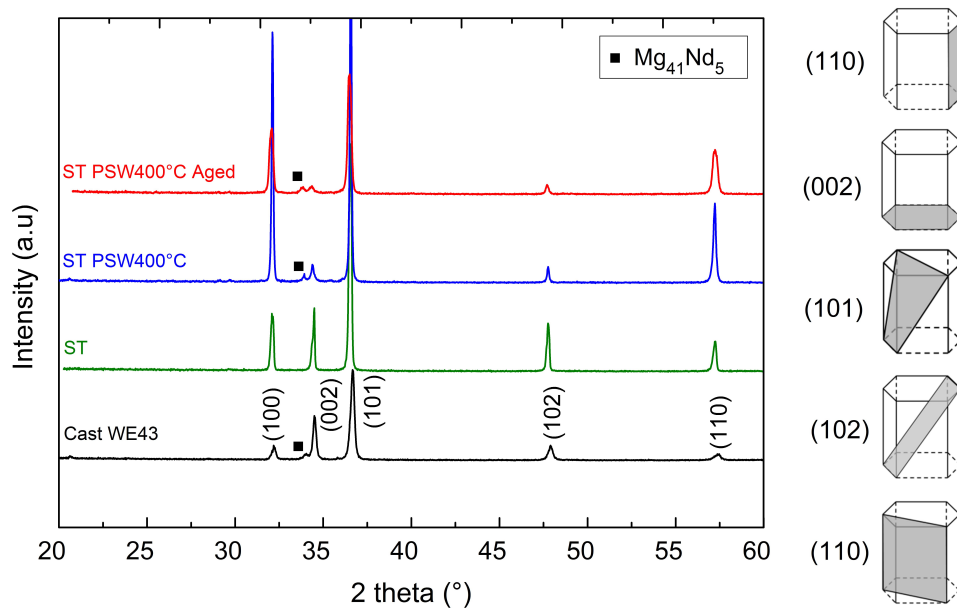


FIGURE 4.12: XRD pattern for, from bottom to top, the WE43 alloy in the cast condition, after solution treatment at 525°C for 5 hours, after one pass of screw processing at 400°C and after ageing at 210° for 16 hours

Figure 4.13 illustrates the evolution of texture during TMT treatment by the mean of ODF maps measured by XRD on the cross section areas of the samples after each step of the treatment and chosen with a value of φ_2 to 50° (ODF data for φ_2 ranging from 0° to 90° is provided in appendix C). As mentioned above, in the cast condition the texture was quite random with no specific preference observed in the ODF data (fig. 4.13 (a)). After annealing treatment, the material started exhibiting a slight change in texture with a small shift of the contour lines to the right hand side of the map, as indicated in figure 4.13 (b). After 1 pass of PSW, a clear texture developed in the billet with all the contour lines located on the right side on the map, suggesting a clear development of texture. This result also confirms the results of the diffraction patterns

of figure 4.12 where a dominant texture was found for (100), (101) and (110) planes with an increase of intensity related to these peaks. It seems therefore that the increase of strength observed in the tensile strain-stress curves after 1 pass of screw rolling (figure 4.4) is not a result of grain refinement but rather of a texture development, with a clear change of crystal orientation between the annealed state and the processed state (1 pass of PSW). After ageing treatment at 210°C, no much difference in the ODF data was observed, indicating a quite similar texture with the processed material. This is also in good agreement with the XRD diffraction patterns.

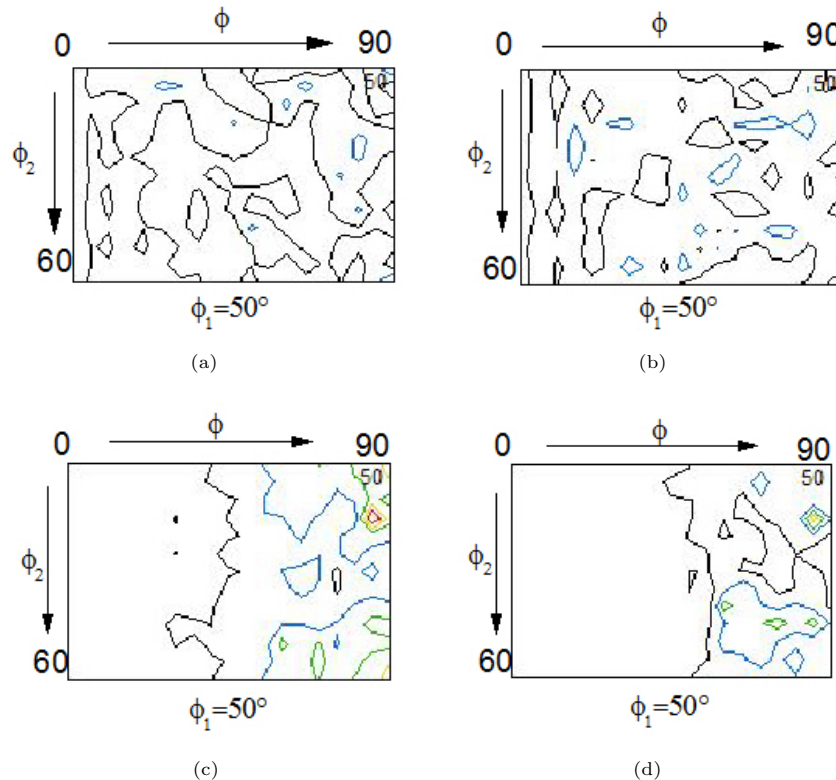


FIGURE 4.13: ODF sections for $\varphi_2=50^\circ$ of (a) cast WE43, (b) solution treated, (c) Solution treated and processed by PSW at 400°C and (d) processed and aged WE43. The Euler convention used here was the same than in figure 3.11

4.3.6 Ageing time and hardening precipitation

4.3.6.1 TEM observations

When high mechanical properties are required, ageing appears to be a very effective method due to the precipitation of second phase particles from the super saturated solid solution (SSSS) at low temperature that helps to impede the dislocation movements. As it is reminded in the chapter 2, Mg-Y-Nd alloys precipitate from the SSSS according to the Polmear sequence of phases $\beta'' \rightarrow \beta' \rightarrow \beta_1 \rightarrow \beta$ with the details of these precipitates summarized in table 4.2.

TABLE 4.2: Details about precipitates in Mg-Y-Nd alloys

Type of precipitates	Shape	Structure	Composition
β''	Platelet	D0 ₁₉	Mg ₃ Y _{0.85} Nd _{0.15}
β'	Disc/globular	centered orthorhombic	Mg ₁₂ YNd
β_1	Plate like	FCC	Mg ₃ RE
β	Rod like	FCC	Mg ₁₄ YNd ₂ /Mg ₅ Nd

In this study, and up to this point, WE43 alloy was aged at 210°C for 16h since this condition was reported to provide best strength to the material. However, in order to analyze the size and shape of the hardening precipitates and their influence on the mechanical properties of WE43, the ageing time was modified in the following section of the study and was ranging from 10 min to 7 days. Transmission Electron Microscopy (TEM) was used to characterize the morphology of the hardening precipitates in function of the ageing time. Figure 4.14 shows the TEM results obtained for the samples processed by PSW and aged for 16h (a), 3 days (b) and 7 days (c).

After 16h at 210°C, the bright field image shows globular-shape fringed regions indicated by arrows with a diameter of about 10 nm. The relative SADP observed in the [01-10] zone axis revealed the spots of the magnesium matrix together with small extra spots located in between (000-2) and (-2110) but also between (0000) and (-2110) and so on. A close look at the SADP image allows to identify 7 extra spots between each magnesium spots, as indicated by arrows. In order to determine the phase of these precipitates a comparison with the data from the literature was made. Barucca et al. [36] found extra spots at $1/2(1, 1, 0, 0)_{\text{Mg}}$ in the SADP of WE43 aged for 8h that can be attributed to β'' phase. Weak diffraction effects around each extra spots were also observed, indicating the presence of β' orthorhombic phase. Accordingly to Barucca et al. these results suggested that both β' and β'' develop in the WE43 alloy aged for 8h at 210°C, with a prevalence of β'' . Mengucci et al. [4] found the same results when the alloy was aged at 210C for 24 hours (cf. figure 2.6 (c) and (d)). Globular phase with a size ranging from 4 nm to 12 nm was observed in the bright image, together with platelets of a thickness of about 2 nm and a length ranging from 5 nm to 25 nm. The authors attributed the globular phase to β' and the platelet to β'' . The associated SADP reveals extra spots at $1/4(1, 1, 0, 0)_{\text{Mg}}$ (β' phase) and at $1/2(1, 1, 0, 0)_{\text{Mg}}$ (β'' phase). Although it is hard to distinguish the exact position of the extra spots in the SADP of processed and aged WE43 for 16h in our case, it can safely be claimed that the phase precipitate observed in the bright field image is β' phase due to the similar globular morphology of the precipitates than in Mengucci et al. study.

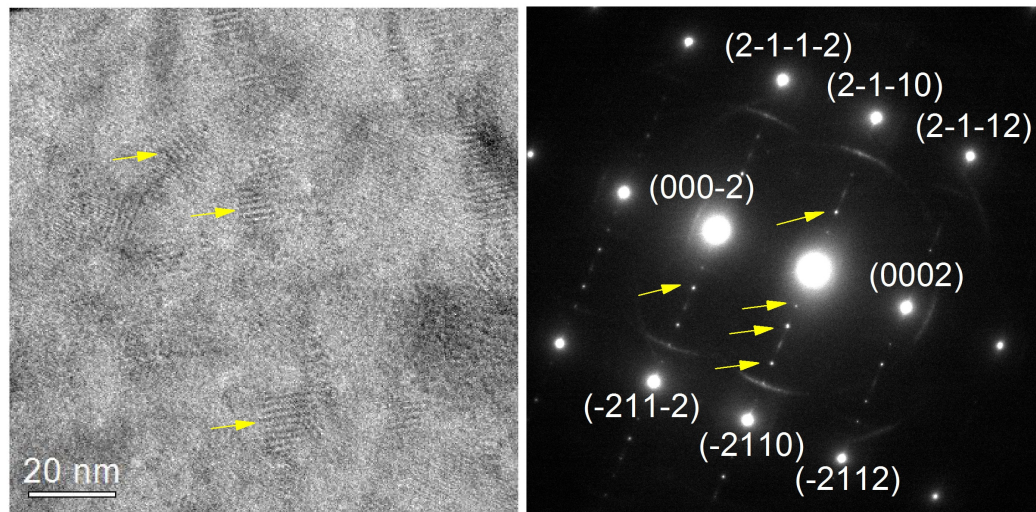
Figure 4.14 (b) shows the formation of hardening precipitates after 3 days ageing observed along [01-10] zone axis. The bright field image revealed plate-like precipitates aligned with (0002) / (-2112) with length of about 40-50 nm dispersed into the Mg matrix as indicated by the arrows. In addition, the same globular fringed precipitates than in the previous case can be observed.

Spots associated to the plate-like precipitates can be seen in the relative SADP. They are located at half the distance of (0002) and (-2112) magnesium spots. At this stage it is not clear either these two kinds of precipitates are β' and β'' phases or β_1 .

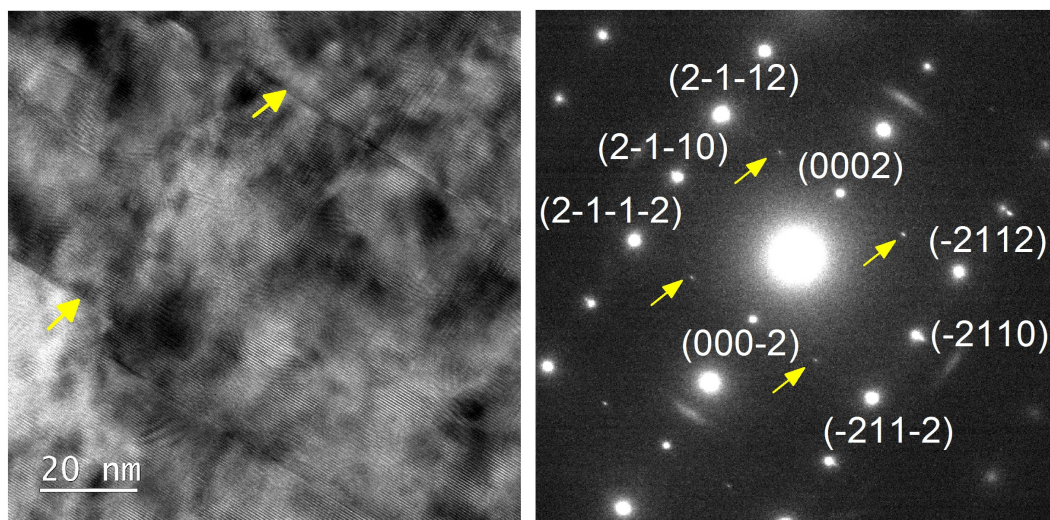
Figure 4.14 (c) reports the results of the observations performed on processed WE43 aged for 7 days at 210°C. Compared with the previous sample (3 days at 210°C) much bigger precipitates can be seen in the bright field image, with a length reaching about 100 nm and a thickness of about 5 nm, indicating a general coarsening during ageing. Also, some globular fringed regions are still visible. In the diffraction pattern of [1-21-3] zone axis they appear as bright extra spots located at half the distance between (0000) and (10-10). According to literature this coarsening cannot be related to the β'' phase and the formation of β_1 phase is proposed as the best explanation.

4.3.6.2 Microhardness measurement as a function of ageing time

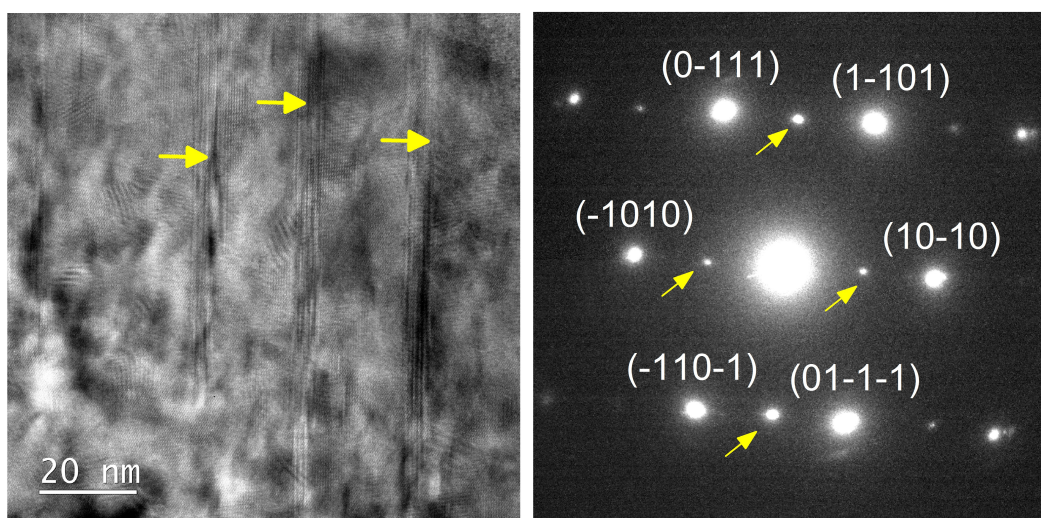
To correlate the thermal treatments with mechanical properties, micro-hardness measurements were made for the samples aged at 210°C for different periods of time as shown in figure 4.15. The figure on the left side (4.15 (a)) depicts the hardness distribution in the samples annealed and processed by PSW and aged for 2h, 16h and 7 days while the figure on the right side (4.15 (b)) illustrates the hardness distribution in the samples aged for 2h, 16h and 7 days (no plastic deformation introduced in the samples). As previously observed, hardness values were not homogeneously distributed over the cross section of the processed samples and it is evident that high values were found at the rim part of the billet, region that received the highest deformation strain. After one pass of screw rolling at 400°C and quenching (ST PSW 400°C), the micro-hardness value in the center of the billet was about 63 Hv. Ageing the material for 2h and 16h resulted in an increase of hardness in its center as it can be seen in figure 4.15 (a) with values reaching 73 Hv and 83 Hv, respectively, but did not lead to higher hardness values at the rim area. Interestingly, application of additional ageing time up to 7 days resulted in a decrease of HV values over the entire cross section of the billet, more pronounced in the center, with values of about 76 Hv. In order to assess the influence of plastic deformation on ageing susceptibilities, the same hardness distribution was measured in samples annealed and aged for the same periods of time. Since the billets did not receive any plastic deformation, the HV values were found to be homogeneous over the cross section of the billets. As before, it can be seen that the HV values increased with increasing ageing time with values of about 63 Hv, 74 Hv and 90 Hv after 8h, 16h and 7 days ageing, respectively. These values correspond in a rough approximation to the values found in the central region of the processed samples, where the screw rolling process had the least influence. When the alloy was aged for 7 days, the same range of HV values was measured in the sample than after 16h. This result was not observed in the processed samples in figure 4.15 (a).



(a)



(b)



(c)

FIGURE 4.14: TEM bright field images and corresponding selected area diffraction pattern (SADP) of processed WE43 alloy after (a) 16 hours ageing (zone axis $[01-10]$), (b) 3 days ageing (zone axis $[01-10]$) and (c) 7 days ageing (zone axis $[1-21-3]$).

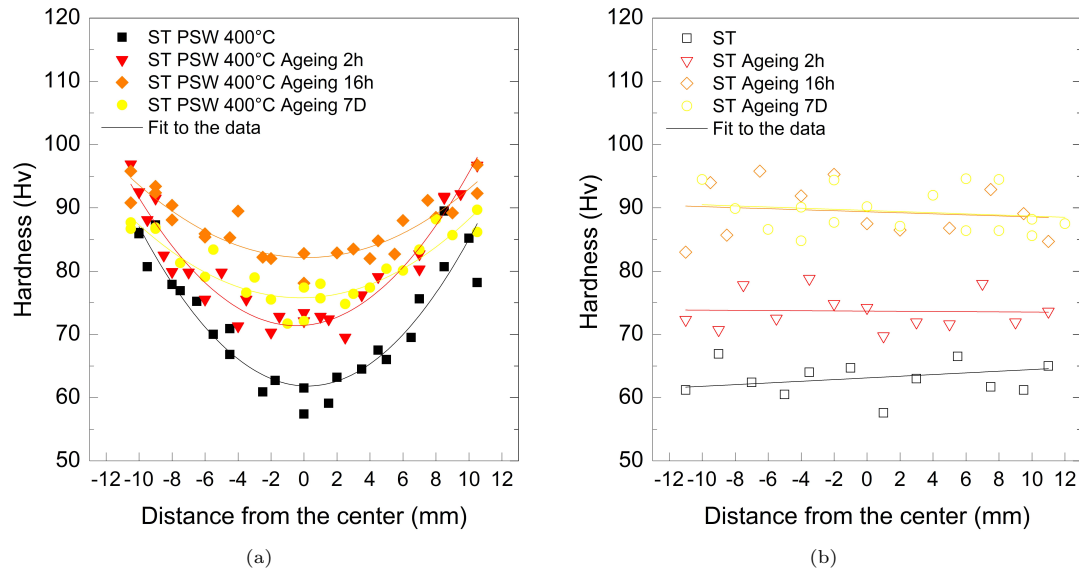


FIGURE 4.15: Hardness evolution over the cross section of WE43 Mg samples after 0h, 2h, 16h and 7 days ageing (a) with and (b) without plastic deformation.

For the sake of clarity and in order to provide a better understanding of the aforementioned decrease of hardness in the interval 16h-7 days, micro-hardness tests were performed after ageing periods ranging from 10 min to 7 days, at a distance of 5 mm from the center corresponding to half the radius of the billet. Figure 4.16 reports the summary of micro-hardness measurements in the processed (ST PSW400°C Aged) and un-processed samples (ST Aged). The curves connecting the experimental points are guidelines drawn to put on view the general trends and to suggest a discussion framework. Data from the literature of a WE43 alloy subjected to a solution treatment at 525°C for 8h followed by quenching and ageing at 210°C for different periods of time (same conditions than our study) [4] were also added in the figure as a way of comparison. First of all it can be seen that the hardness curves exhibited the same trend in the first ageing time interval 0-8h with a constant increase of micro-hardness and values reaching 87 Hv and 82.5 Hv for the processed and un-processed WE43, respectively. Thus, it can be noted that WE43 processed by PSW had higher values of hardness than the un-processed WE43, which is in a good agreement with all the previous conclusions of chapter 3 and observations of chapter 4, considering that the hardness was measured in a distance of 5 mm from the center of the billet. As indicated in figure 4.16, the results obtained here are very close to the ones of Mengucci et al [4]. Therefore, this same increase of hardness in the two samples suggests the development of a similar microstructure during ageing. TEM observations in the post-PSW aged (16h) sample suggested the presence of both platelet β'' phase and globular β' phase which has been reported to provide the best hardness to the material. The maximum hardness value of 87 Hv after processing and 16h ageing seems thus to be the peak hardening condition due to the presence of two kinds of precipitates in the microstructure. It is believed that the transformation β'' to β' occurs in the first stage of ageing, during short period of ageing time or during ageing at lower

temperature. In contrast, starting from 16h ageing the two hardness curves tend to diverge: while the annealed and aged curve (ST Aged) continues to increase for up to 3 days with a hardness peak at 97 Hv, the annealed, processed and aged curve (ST PSW400°C Aged) slowly drops to 80 Hv after 7 days. Therefore, after a long ageing period ($\geq 16\text{h}$) the post-PSW aged WE43 alloy exhibited lower hardness values than the aged one. This decrease of hardness can be associated with an increase of volume fraction of β_1 precipitates observed in the microstructure after 3 days ageing, as mentioned in the literature [82]. Further ageing to 7 days increased the size of β_1 phase precipitate, as seen in figure 4.14 (e), resulting in a decrease of hardness with a final value of 80 Hv. Concerning the annealed and aged sample, it must added that no TEM characterization was performed and therefore no conclusion can be drawn as for the increase of hardness after long ageing period.

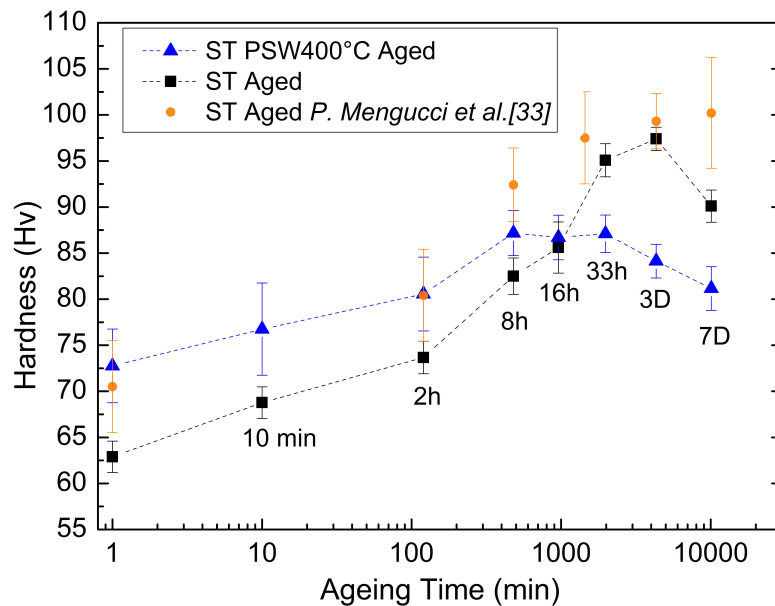


FIGURE 4.16: Vickers hardness as a function of ageing time for solution treated, processed and aged samples (ST PSW400°C Aged) and solution treated and aged samples (ST Aged) subjected to ageing at 210°C. As a way of comparison data from the literature of a WE43 alloy subjected to a solution treatment at 525°C for 8h followed by quenching and ageing at 210°C for different period of time (same conditions than our study) [4] were also added in the figure.

4.3.7 Corrosion behaviour after thermo-mechanical treatment

In addition to grain refinement and texture change, SPD processes cause a redistribution of solutes within the microstructure. Considering that both microstructural features and composition changes can have a large impact on magnesium corrosion [83], it can be expected that the corrosion behaviour of magnesium alloys after SPD, and therefore PSW process, will be modified. However, there is currently no detailed understanding of how plastic deformation affects the corrosion of magnesium. Most of the studies support the idea that ultra fine grained (UFG)

materials present a superior corrosion resistance than coarse structure materials but conflicting findings were reported in the literature. Moreover, the only effect of grain size is hard to isolate due to the introduction of dislocations, segregation and so on during SPD.

In order to assess the corrosion behaviour of the PSW processed and aged WE43 alloy, in-vitro corrosion tests were carried out by the mean of pH evolution and potentiodynamic tests. Figure 4.17 shows the change of pH of SBF solution during immersion of cast WE43 and post-PSW aged WE43 (16h) samples over a period of 96 hours (4 days). Extruded pure magnesium was also immersed into SBF in order to provide comparative data. No much difference was observed between the three samples, with a quite similar pH evolution and a final pH value of about 10 after 96 hours immersion. Interestingly, extruded pure magnesium exhibited a slightly lower corrosion rate, although the difference with the other samples was not significant. It is therefore believed that the initial texture of pure magnesium provided corrosion resistance enhancement to the sample since cast WE43 magnesium alloy was reported to exhibit better corrosion resistance than cast pure magnesium [76], which is not the case here. Moreover, it is worth noting that grain refinement did not occur much in WE43 sample after 1 pass of PSW and post-PSW ageing led to grain growth with grain size of about $100 \mu\text{m}$. It can be concluded that the similar pH evolution and thus similar degradation behaviour of cast WE43 and post-PSW aged WE43 can be explained by the lack of strong SPD mechanisms introduced into the microstructure of WE43 after 1 pass.

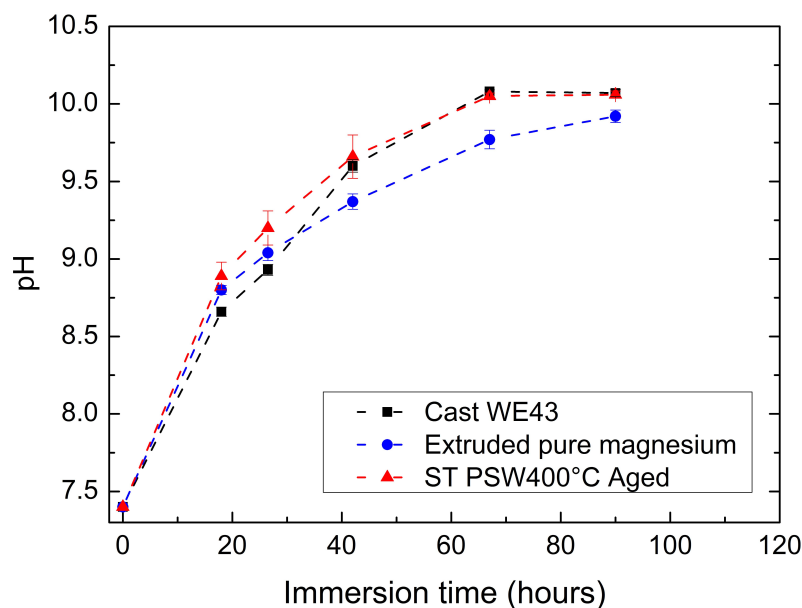


FIGURE 4.17: pH variation as a function of immersion time in SBF of extrude pure magnesium, cast WE43 and PSW-processed WE43.

Electrochemical polarization tests were also conducted to determine the corrosion rate of cast WE43, processed and aged WE43 and extruded pure magnesium, as displayed in figure 4.18. While the three specimens presented almost the same corrosion current density of $I_{\text{corr}}=2\text{-}3 \cdot 10^{-6}$

A/cm², their corrosion potential E_{corr} was found to be slightly different. Cast WE43 had the highest corrosion potential with a value of -2.15 V suggesting a fast rate of cathodic reactions. Post-PSW aged WE43 and extruded pure magnesium had lower values of -2.25 V and -2.3 V, respectively. However, the corrosion rate of metals is usually calculated using the value of the corrosion current density I_{corr} . Since the three specimens exhibited a relatively similar current density, no conclusion can be drawn as for the effect of PSW process on the corrosion behaviour.

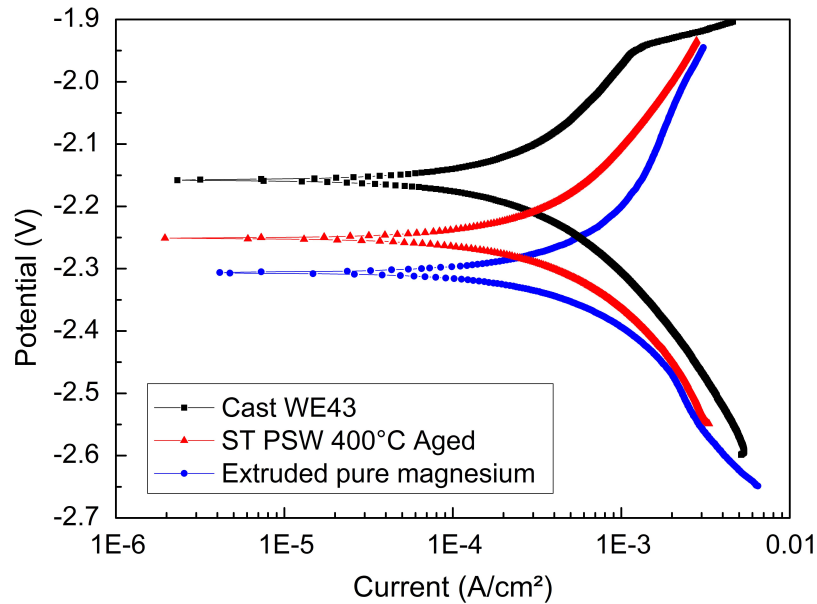


FIGURE 4.18: Sample polarization curves for cast WE43, PSW-processed and aged WE43 and extruded pure magnesium in SBF solution.

4.4 Results and discussion

4.4.1 Microstructure, texture and improved mechanical properties

The results presented in this study have shown the clear advantage of combining a mechanical and thermal treatment to reach high mechanical properties of WE43 magnesium alloy.

After a first pass of screw rolling at 400°C, the yield strength of the material greatly increased from 140 MPa to 220±20 MPa. The observation of the microstructure after processing did not reveal a significant grain refinement with a grain size dropping from 63 μm to only 58 μm at the rim area of the billet. Therefore, the enhancement of mechanical properties cannot be attributed to grain refinement and texture analysis was conducted in the processed material. XRD results showed the clear development of (110) planes perpendicular to the extrusion direction, promoting strengthening effect (figure 4.13).

After ageing the processed alloy for 16 hours at 210°C, another increase of strength was observed, with a yield strength increasing from 220±20 MPa to 280±10 MPa. A huge grain growth also occurred due to the release of energy accumulated into the grains caused by heating, with a grain size reaching about 100 μm. TEM analysis performed on processed and aged WE43 alloy highlighted the presence of globular β' phase of hardening precipitates in the microstructure (figure 4.14 (a)). Although the formation of both β' and β'' was reported in the literature for the same ageing conditions, the presence of β'' phase cannot be confirmed.

4.4.2 Increase of the number of passes of screw rolling and modification of the ageing time

In order to evaluate the effect of both treatments, the number of PSW passes and the ageing time were modified and their influence on the mechanical properties of WE43 magnesium alloy were analyzed.

In a first approach, the alloy was processed up to three times at 400°C and subsequently aged. The tensile tests carried out after processing showed that increasing the number the passes resulted in higher mechanical properties, with a yield strength of about 220 MPa after 1 pass, 240 MPa after 2 passes and 260 MPa after 3 passes (figure 4.7 (a)). These results confirmed the conclusion of chapter 3. However, after ageing the alloy, the strength of the WE43 processed 3 times was lower than that of the WE processed 1 time. No explanation was found to explain this result.

In a second approach, the ageing time was modified and set to different periods of time, ranging from 10 minutes to 7 days, and its effect on WE43 evaluated by hardness measurements. Two observations were made from the hardness curve: a first increase of hardness in the interval 0 - 33 hours and a decrease of hardness in the interval 33h - 7 days. The increase of hardness in the first period of ageing is attributed to the formation of globular β' and platelet β'' phases precipitates, which have been reported to provide the best hardness to WE43. TEM observations of the alloy processed and aged for 16h confirmed this result with the presence of globular β' phase. The decrease of hardness after a long ageing period can be associated with an increase of volume fraction of β_1 precipitates observed in the microstructure after 3 days and 7 days ageing (figure 4.14 (c) to (f)), as mentioned in the literature.

4.4.3 Comparison of thermo-mechanical treated WE43 alloy with only thermal treated WE43 alloy

The beneficial effect of processing WE43 magnesium alloy by screw rolling in addition to the common ageing treatment is presented here.

As mentioned above, it seems that the thermo-mechanical treatment proposed in this study presents a limited efficiency, as suggested by the decrease of hardness after an ageing period of 33 hours. Micro-hardness measurements were therefore performed with only aged alloy (non-processed) in order to evaluate the potential of screw rolling as a supplement treatment. Results showed that carrying a mechanical treatment in addition of ageing was beneficial in the first period of ageing only, with higher hardness values in the interval 0-16 hours (Figure 4.16). For an ageing period of 16 hours, the processed and non-processed samples exhibited the same hardness of about 85 Hv (measured at half the radius of the samples). For longer ageing periods, it was shown that performing a single thermal treatment enabled to reach high mechanical properties.

To analyze more in details the mechanical properties of the two samples after 16h ageing, tensile tests were carried out and the results are presented in figure 4.19. Although the two samples exhibited the same hardness for this specific condition, it was can be seen that the yield strength of the processed and aged alloy was much higher than that of the only aged alloy, with values of 280 MPa and 230 MPa, respectively. Therefore, adding a mechanical treatment to a thermal treatment gives rise to higher mechanical properties, in the condition that the ageing period does not excess 33 hours.

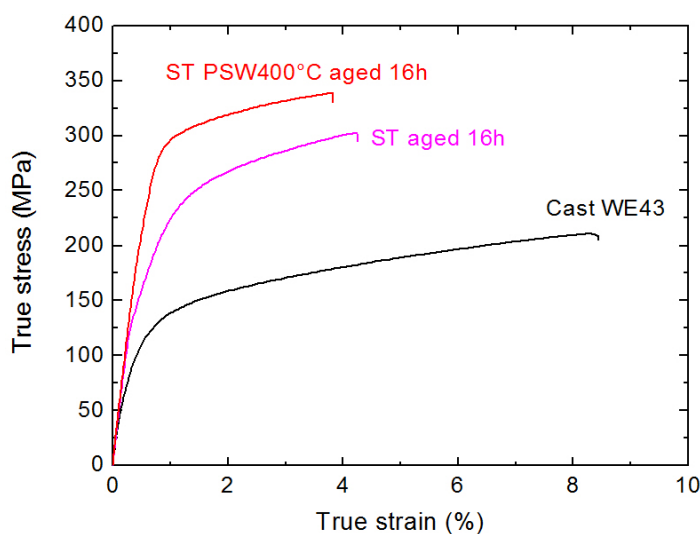


FIGURE 4.19: True stress-strain curves for WE43 magnesium alloy in the cast conditions, after PSW processing and ageing, and after ageing.

4.4.4 Corrosion of the processed WE43 magnesium alloy

Finally, the corrosion behaviour of processed and aged WE43 alloy was assessed by in-vitro corrosion tests. It was found that applying a thermo-mechanical treatment does not have a significant effect on the corrosion rate of the alloy since the electrochemical polarization test and pH evolution did not reveal much difference between cast WE43 and treated WE43. However

it was pointed out that the lack of strong SPD mechanisms introduced into the billet after one pass of PSW, such as grain refinement, was not very relevant for the study.

4.5 Conclusion

In this work, a new thermo-mechanical treatment to improve the mechanical properties of WE43 magnesium alloy has been presented. The combination of one single pass of three roll planetary milling at 400°C and ageing treatment for 16h at 210°C has allowed the production of billets exhibiting an excellent combination of strength and ductility. Analysis of microstructure and texture of the processed and aged billets shows this excellent mechanical behaviour can be attributed to the synergy of a favorable (110) texture developed during screw rolling and to the formation of globular β' phase precipitates during ageing, known to provide good hardness. However, a loss of mechanical properties occurs when the ageing period exceeds 33 hours, owing to the formation of β_1 phase precipitates. Therefore, one will make the conscientious choice of using thermo-mechanical treatment for relatively short periods of ageing. It is believed that the excellent balance of enhanced mechanical properties achieved with WE43 alloy can also be obtained with other Mg alloys.

Chapter 5

Behaviour of dual HA-PLLA coated WE43 magnesium alloy under strain

5.1 Introduction

Despite the benefits of Mg associated with its biocompatibility and biodegradability, its development for biomedical applications has been limited because of its poor corrosion resistance in aqueous solutions, particularly solutions containing chloride ions such as body fluids. It results therefore in a loss of functionality by deterioration of its mechanical properties before the bone has fully healed [1]. Moreover, the increase of pH in the vicinity of the implant and the formation of hydrogen gas cavities might cause serious problems for the patient.

To improve the corrosion resistance of magnesium and control its degradation rate, the most common method consists in applying a coating on the surface of magnesium that could serve as a barrier between the corrosive medium and the metal substrate. The coating can be polymer, ceramic or metal. In addition, the coating should not only serve to delay the initial degradation of Mg but also improve its biocompatibility, enabling enhanced osseointegration between the coated implant and the surrounding tissue. One of the most promising coating materials was reported to be calcium phosphate based, especially hydroxyapatite (HA; $\text{Ca}_{10}(\text{PO}_4)_6(\text{OH})_2$) due to its high bioactivity owing to its similarity to native mineralized tissues. Very good in-vitro and in-vivo results were obtained with such HA coated magnesium implants in terms of cell attachment, proliferation and corrosion rate [17]. Nevertheless, concerns have been raised about this technique since HA exhibits a very brittle behaviour and often displays cracks or pores

under deformation, which result in unfavorable corrosion levels. Others solutions have also been proposed to confer protection to Mg such as the deposition of a polymer layer on its surface. Biodegradable polymers, including PLA, PLLA or PCL for example, have widely been used as coating materials for biomedical applications due to their easy implantation, cheap price and good biocompatibility. However, as any deposition technique, the bonding strength between the substrate and the polymer turns to be very low, in the range of few MPa, resulting in a poor adhesion to magnesium substrate and upcoming risk of delamination during implantation period [53].

Although many coating solutions have been studied with various conclusions, it remains that only few studies have focused their attention on the behaviour of coated magnesium under deformation. Given that most of implants are subjected to loads, either static or repetitive, an excellent combination of strength and ductility is required and therefore the analysis under deformation is a criterion to take into consideration. In this work, a new two-steps coating, wherein HA is coated by conversion method prior to PLLA deposition, is proposed as a strain resistant coating for WE43 magnesium alloy able to provide biocompatibility, good adhesion to the substrate, stability and protection under deformation. In such a way, the cracks formation in HA layer might be reduced and the contact between magnesium and the medium avoided. In parallel, the bonding strength between PLLA and magnesium substrate is expected to be enhanced. The stability of the HA-PLLA composite coating subjected to deformation was investigated by the mean of corrosion test, hydrogen gas release test, tensile test after immersion into simulated body fluid (SBF), cell attachment and proliferation.

5.2 Methods

The material used in this study was the same than the one used in chapter 4, namely cast WE43 magnesium alloy (4.51% Y, 2.05% Nd, 0.31% Zr, 0.051% Ca, 0.0117% Mn and balance Mg) purchased from Yueyang Yuhua Yejin company, China. Dog-bone shape specimens were machined and then annealed at 525°C for 5 hours and air cooled in order to reduce the size of the second phase particles and obtain the most homogeneous possible surface. Hiromoto et al. [84] have indeed showed that the presence of exposed second phase particles could prevent the formation of HA nucleation in these areas and that a pre-treatment to remove any enclosure would be desirable to obtain a more uniform HA coating on Mg alloy. The specimens were then mechanically polished with SiC paper up to 1200 grit, cleaned in ethanol and air dried. The HA layer was then formed on the WE43 substrate by immersing the specimens in a 0.05 M ethylenediaminetetra acetic acid calcium disodium salt hydrate (Ca-EDTA) and 0.05 M potassium dihydrogen phosphate (KH_2PO_4) solution at 90°C for 2h, which pH was prior adjusted to 9.3 with sodium hydroxide (NaOH). This pH value was chosen accordingly to the results

of the experimental procedure presented in Appendix C. This conversion technique procedure was previously reported in the study of Hiromoto et al. [84] and was reported to exhibit very good adhesion to the substrate. The coated samples were then rinsed with distilled water and air cooled. As a second step, polymeric coating was synthesized by mixing PLLA in dichloromethane (DCM) as a solvent in concentration of 10 wt.%. The mixture was stirred for 24h at 37°C in order to obtain a viscous and homogeneous solution. The previously HA coated samples were then immersed in the polymeric solution for 5 minutes in a vacuum chamber at 0.05 MPa in order to promote good interaction between PLLA and rough HA and dip coater as used to deposit the polymer layer at a speed of 300 $\mu\text{m}/\text{sec}$. Finally the specimens were rinsed with ethanol and air dried. Figure 5.1 illustrates the experimental procedure described above. As it can be seen any kind of sample shape or size can be coated with this simple procedure.

A 5% strain deformation was applied to the specimens by using an Instron tensile machine at a speed of 0.3 mm/min. This value was chosen in accordance with the strain to failure of the cortical bone, representing the maximum deformation that can be transferred to the implant. Moreover, no extensometer was used in order to not deteriorate the coated area of the samples during deformation. Then, the two sides of the dog bone shape specimen that were not subjected to deformation were covered with epoxy so that the only strained part of the sample was analyzed. In this study the behaviour of different samples were studied: cast WE43, HA coated WE43, PLLA coated WE43 and dual HA-PLLA coated WE43.

The surface morphology of the specimens was observed by SEM (JSM-5600; JEOL, Japan) and the cross sectional morphology of the coated specimens was analyzed by FESEM (JSM-6330F; JEOL) equipped with a focused ion beam (FIB). The crystalline structure of the HA coating layer was examined by XRD diffraction (XRD, D8 Advance; Bruker, Germany).

In order to evaluate the bonding strength between the HA layer and the substrate, adhesion test was performed using an adhesion tester (RB302 single-column type; RB, Korea). The HA coated WE43, onto which a pre-epoxy coated stud was attached, was heated at 150°C for 1h in an air oven, then fixed to the tester jig and the stud was pulled off vertically until the coating layer failed. The adhesion strength was calculated using the failure area and the recorded maximum pulling force. Five samples were tested and average adhesion strength was calculated.

The corrosion resistance of the specimens was characterized by the mean of in-vitro tests performed in simulated body fluid (SBF). In a first experiment, the specimens were immersed in 80 mL of SBF solution and the pH was monitored at different time intervals over a period of 10 days by a pH meter (sp-701; Suntex, Taiwan), together with the amount of hydrogen gas released. After 10 days immersion, the specimens were taken out of the SBF and their surface morphology observed by SEM to characterize their deterioration state and analyze the corrosion product formation. A second in-vitro test consisted in measuring the amount of magnesium ions

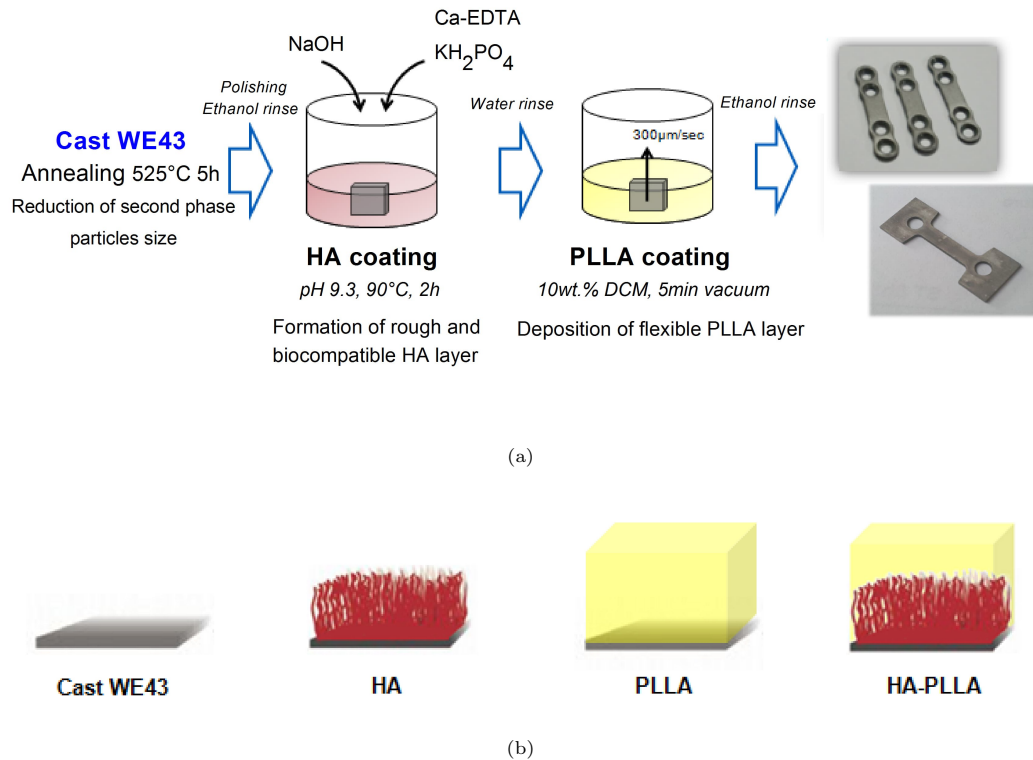


FIGURE 5.1: (a) Experimental procedure of the two steps WE43 strain resistant coating. First HA was formed by conversion technique then PLLA was deposited by deposition technique. As it can be seen all sizes and shapes of specimens can be coated by this simple technique. (b) In this study four different specimens were studied.

present in the SBF solution after 1, 4 and 7 days, revealing the corrosion state of the specimens. In order to determine the Mg ions concentration, the SBF was extracted and analyzed by using an inductively-coupled plasma atomic emission spectrometer (ICP-AES, Optima-4300 DV, PerkinElmer, Wellesley, MA). Five specimens were tested for each condition.

To verify that the composite coated specimens can maintain their mechanical integrity after implantation and under deformation, tensile test was performed on dog bone shape specimens after their immersion into SBF for 10 days. Their strength was evaluated by Instron 5582 testing system at a cross head velocity of 0.5 mm/min and compared to that of cast WE43, HA coated WE43 and PLLA coated WE43 samples.

To assess the biocompatibility of the fabricated specimens, in vitro cell tests were carried out. Preosteoblast cell line (MC3T3-E1) was used to evaluate the cell response, in terms of cell attachment and proliferation. Alpha-minimum essential medium (Welgene Co., Korea) with addition of 10% fetal bovine serum and 1% penicillinstreptomycin was used as the cell culture medium and the cells were cultured in a humidified incubator in air atmosphere containing 5% CO₂ at 37°C. After culturing for 2 days and 3 days with a density of 1.5×10^4 cells/mL, the

attached cells were observed by SEM (JSM-5600, JEOL) and confocal laser scanning microscopy (CLSM, LSM 510 NLO, Germany), respectively. Prior to the SEM observations, the samples were fixed with 2.5% glutaraldehyde for 10 min, dehydrated in graded ethanol (70, 90, 95, and 100% ethanol in sequence), immersed in hexamethyldisilazane for 10 min and dried in air. For the CLSM examination, the cultured cells were dyed with Alexa Fluor 546 phalloidin (Eugene) and ProLong Gold antifade reagent with 40,6-diamidino-2-phenylindole (Eugene). Cell proliferation was determined after 3 days of culturing using a Cyquant cell proliferation assay kit (C7026; Invitrogen). Before measurements, the cells that adhered to the samples were detached and suspended in a fluorescent dye solution. The DNA level of the detached cells was measured using a multiple plate reader (Victor3; PerkinElmer) at 480/535 nm wavelength. The measured fluorescence values were converted to the DNA content using a DNA standard curve. In this assay kit, the DNA level was directly proportional to the number of living cells.

5.3 Results

5.3.1 Composition and adhesion strength of HA coating

First, the properties of only HA coating were characterized in terms of composition, shape and attachment to the substrate. Given that HA layer plays an important role as interlayer between PLLA and WE43, with the role of improving adhesion of PLLA to the substrate and preventing its delamination during implantation, its properties needed to be assessed.

To confirm the presence of HA crystals, the coating layer formed after conversion technique was analyzed by XRD, as shown in figure 5.2 (a). The diffraction pattern of cast WE43 Mg alloy substrate prior to conversion treatment is shown at the bottom of the figure. After treatment, it can be seen that the diffraction pattern of the coated material displayed diffraction lines (filled stars) along with the one of WE43. By comparing the 2-theta values of these diffraction lines with the values from the literature, they were identified arising from HA structure. In particular, the peak intensity of (002) plane of HA, at $2\theta=26^\circ$, was higher than the others, suggesting that (002) plane of HA was oriented on WE43 in the same way than on pure magnesium [85].

The morphology of the HA crystals formed on WE43 was observed by FESEM (figure 5.2 (b)). Densely packed dome-shape precipitates with diameters of 1-2 μm were observed, with thin and long needle crystals of few nanometers growing from each dome in the radial direction. This morphology is quite similar with the cauliflowers morphology of HA observed after treatment of pure magnesium [1] and even more with the morphology of HA formed on AZ31 after 4 hours [84]. The formation of macro-dome precipitates and nano-needles is believed to provide good roughness to the coating layer.

The bonding strength between HA layer and WE43 substrate was characterized by the mean of adhesion test. As depicted in figure 5.2 (c), the HA coating layer was detached from the substrate after that a tensile strength of about 16 MPa was applied, which is in the range of other HA-based coating. It is worth noting that the literature data juxtaposed with our result in figure 5.2 (d) only concern coated pure magnesium. No data about the adhesion of HA-based coated magnesium alloys was found.

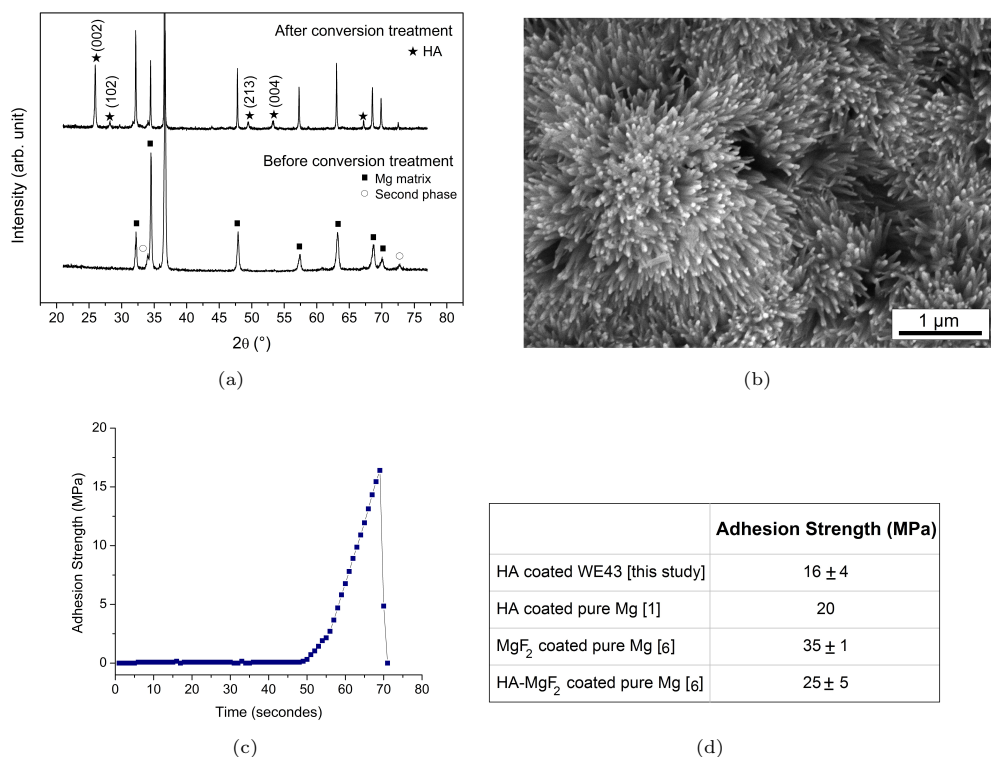


FIGURE 5.2: Characterization of the different properties of the HA coating layer. (a) XRD diffraction patterns of calcium-phosphate coated WE43 Mg alloy before (bottom) and after (top) conversion treatment. (b) FE-SEM image of the HA coating layer formed on WE43 Mg alloy after conversion treatment for 2h, in a solution of a pH of 9.3. (c) Adhesion test curve performed on HA coated WE43. (d) Literature data [1, 5] juxtaposed with our result of adhesion strength.

5.3.2 Morphology of the composite coating

After that the phosphate calcium coating layer was formed on WE43 Mg alloy, a post-conversion treatment was carried out in order to create a composite coating layer with improved properties. This post-conversion treatment consisted in depositing PLLA polymer layer by dip coating technique.

Figure 5.3 presents SEM images of WE43 magnesium alloy in the cast condition, after annealing, coated with HA, PLLA and dual HA-PLLA. As it can be seen in figure 5.3 (a) the initial microstructure of the alloy consisted of coarse grains with yttrium and neodymium second phase

particles located at the grain boundaries. After annealing at high temperature (just because melting point) the second phase was totally dissolved in the Mg matrix giving the alloy a uniform and smooth microstructure as shown in figure 5.3 (b). This homogeneous surface enabled the formation of HA coating without defect or heterogeneity on WE43 alloy substrate. The morphology of HA was similar to the one reported in the literature [1, 84] with needle like shape crystals (figure 5.3 (c)). When PLLA layer only was deposited on WE43 substrate, a homogeneous and opaque layer was observed, without any sign of cracks or porosity. In a same way, dual HA-PLLA coating exhibited a uniform and dense morphology.

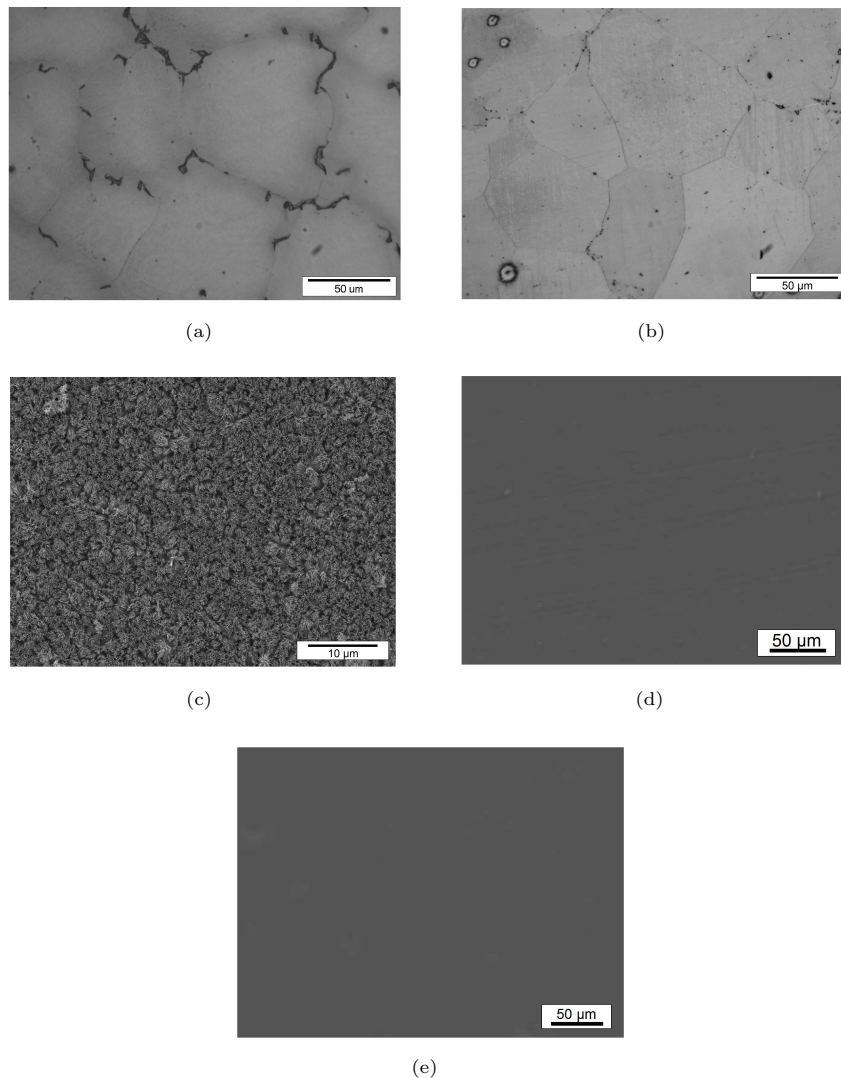


FIGURE 5.3: SEM images of (a) the microstructure of WE43 magnesium alloy in the cast conditions, (b) after annealing at 525°C for 5h, (c) HA coated WE43, (d) PLLA coated WE43 and (e) dual HA-PLLA coated WE43.

The thickness of each coating layer was estimated according to the cross section views generated by FIB. After 2h immersion in aqueous solution, HA layer was formed with a thickness of about 4 μm which is comparable with the results of Hiromoto et al. [84] who reported the formation

of a $3.7 \mu\text{m}$ thick HA layer on AZ31 substrate after 4h treatment. Nevertheless, the thickness obtained here is much higher than in the case of HA coated pure magnesium where a layer of $1 \mu\text{m}$ was formed after 2h immersion, suggesting a fast reaction rate in the case of WE43. Moreover it can be seen that HA was relatively well bonded to the substrate without significant gap between them or defects. The thickness of PLLA layer coated on WE43 is shown in figure 5.4 (b). As previously observed, the polymer layer did not present any porosity and was deposited with a thickness of about $7 \mu\text{m}$ on the substrate in order to make a fair comparison with the dual HA-PLLA coating. In that latter case, figure 5.4 (c) and (d) give a detailed view of the composite formed by HA ceramic layer and a PLLA polymer layer of the same thickness of about $3.5 \mu\text{m}$. It can be seen that PLLA was well infiltrated into the HA needles owing to a suitable viscosity of PLLA and the use of a vacuum system during second coating, assuring a good bonding between the two coating layers. Contrary to figure 5.4 (a) more gap was observed between HA and WE43 Mg substrate, highlighting the fact that the ceramic layer was not always well bonded to magnesium, resulting in a slightly less adhesion strength than HA coated pure magnesium, where pure magnesium was perfectly converted to HA.

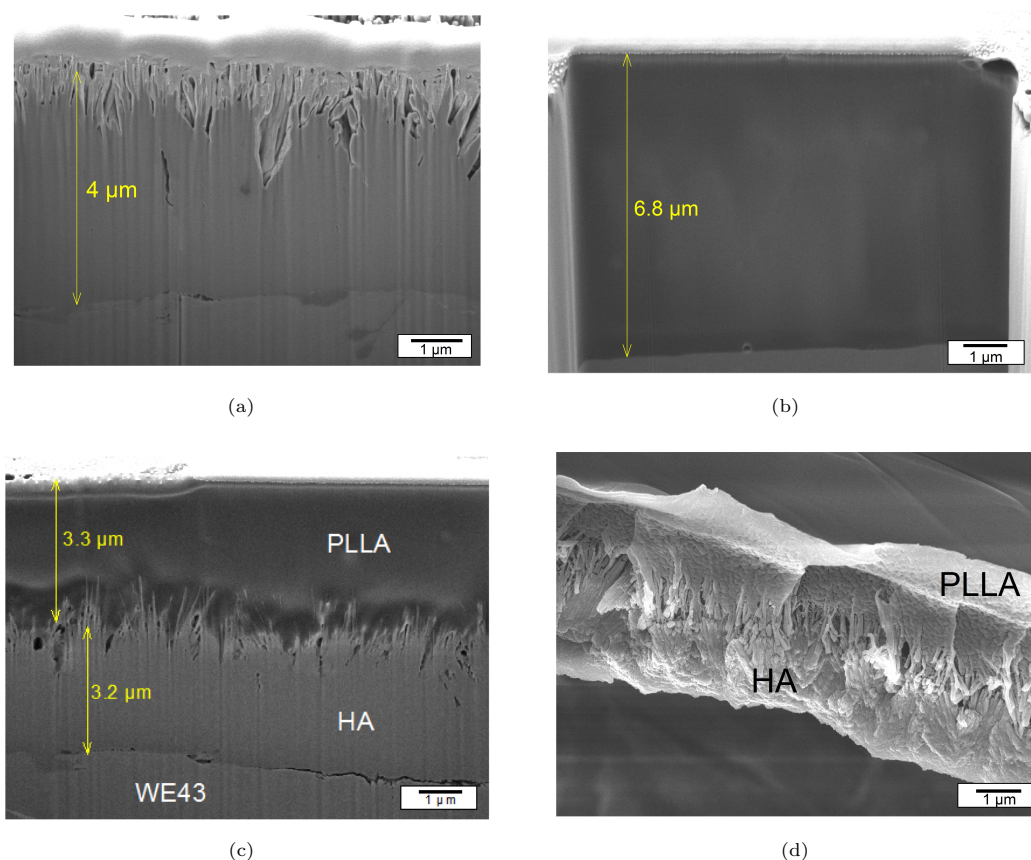


FIGURE 5.4: Cross section views taken by FIB of the (a) HA coated WE43, (b) PLLA coated WE43 and (c) dual HA-PLLA coated WE43. (d) FE-SEM image of scraped-off dual HA-PLLA coating showing the good adhesion between HA and PLLA.

5.3.3 Coating morphologies after application of strain

In order to study the behaviour of coated WE43 magnesium alloy in real cases application, the specimens were deformed to a tensile strain of 5%. SEM images taken after application of strain are presented in figure 5.5. While cast WE43 did not show any apparent microstructural changes (fig. 5.5 (a)), the HA coating layer exhibited multiple cracks perpendicular to the tensile direction, with length of more than $50\ \mu\text{m}$. Some parts of the coating also detached from the substrate, exposing magnesium to the outer environment. Thus it is clear that HA cannot sustain protection to magnesium when deformation is applied to the implant due to its brittle behaviour. It is believed that lower levels of strain result in the same way in cracks formation and damages in the coating layer. Observations of PLLA coated WE43 sample subjected to strain did not reveal the presence of cracks or defects in the coating layer and seemed to maintain a quite good adhesion to the substrate. When a HA interlayer was added between PLLA and the Mg alloy, the formation of cracks in the HA could not be avoided, as depicted in figure 5.5 (d). However, a close look at the picture reveals that the crack did not open up to the surface, preventing the infiltration of the liquid solution inside it.

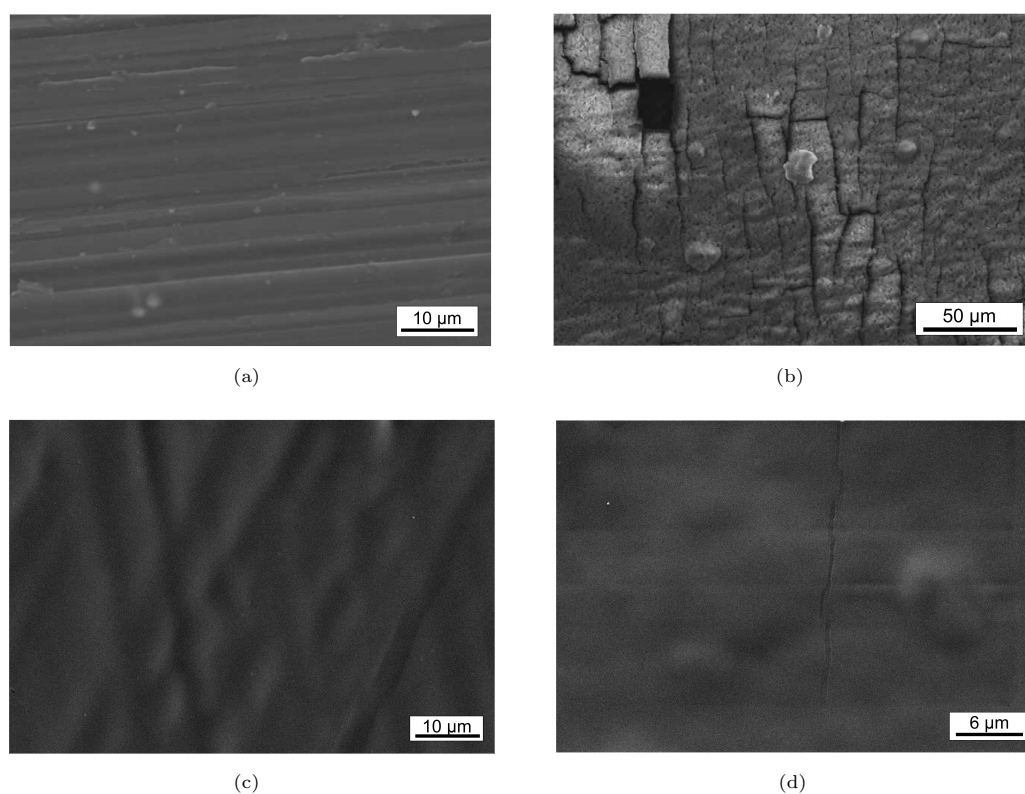


FIGURE 5.5: SEM images of (a) polished cast WE43, (b) HA coated WE43, (c) PLLA coated WE43 and (d) dual HA-PLLA coated WE43 after application of 5% strain.

5.3.4 Electrochemical response and potentiodynamic polarization curves

Polarization experiments were conducted in SBF solution (pH=7.4) to differentiate the electrochemical response as a function of the different coatings subjected to strain. Figure 5.6 shows anodic polarization curves for cast WE43 sample obtained in SBF overlaid with polarization curves of the three coated WE43 samples. As it can be seen, cast WE43 presented a typical behaviour with a corrosion potential E_{corr} of -1.9 V and a corrosion current density $\log(i_{\text{corr}})$ of -5.7 A/cm². Although cracks and delamination occurred in the HA layer after deformation, the corrosion resistance of the structure was improved with an increase of corrosion potential and current density. PLLA coated WE43 also shows the same trend with values of E_{corr} of -1.6 V and a current density of $\log(i_{\text{corr}})$ of -9.9 A/cm². It must be noted here that this result refers to the electrochemical response of the polymer layer only. The application of deformation to the coating did not affect its shape or morphology and no delamination of the coating could be observed due to the sample preparation for the experiment. Therefore the polarization curve of PLLA coated WE43 sample under strain was found to be the same than PLLA coated WE43 without deformation, which provides good corrosion protection. Finally, HA-PLLA coated WE43 specimen showed the best corrosion behaviour with low current density of $\log(i_{\text{corr}})$ of -11.4 A/cm².

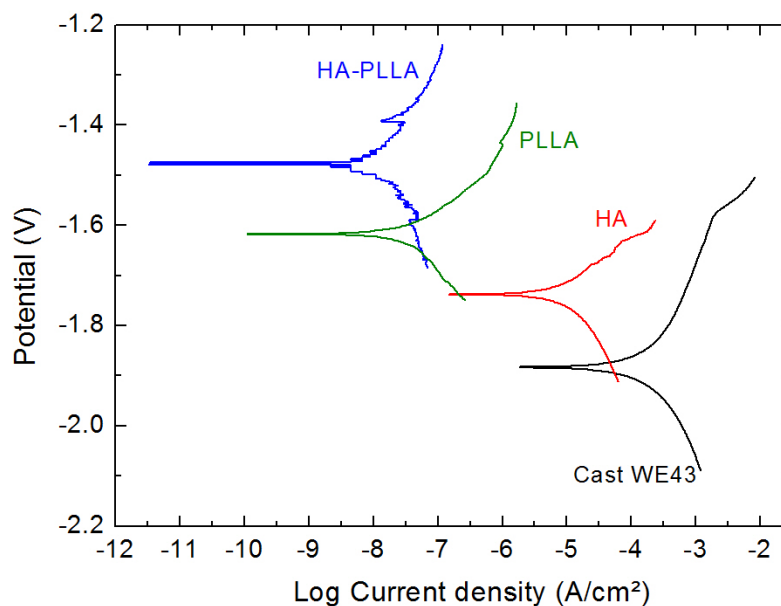


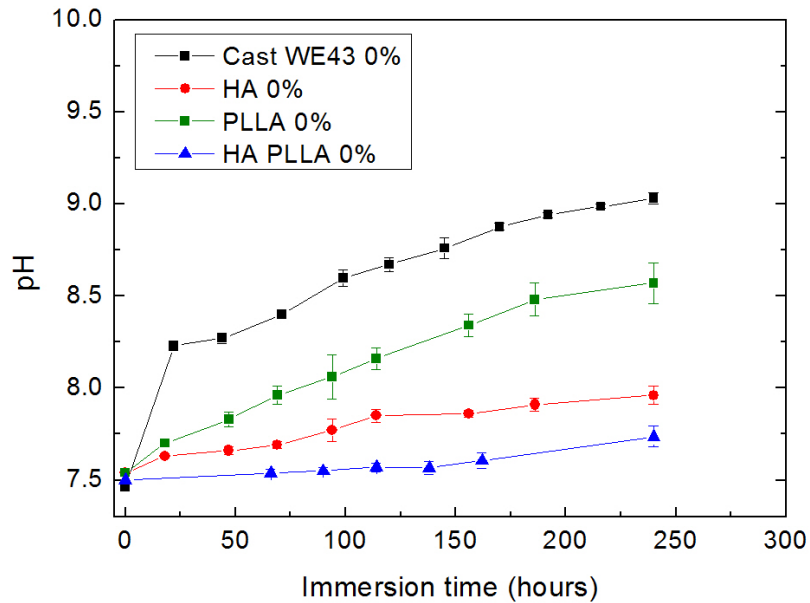
FIGURE 5.6: Polarization curves for cast WE43, HA coated WE43, PLLA coated WE43 and HA-PLLA coated WE43 subjected to 5% strain, obtained in SBF solution with a pH of 7.4.

5.3.5 In vitro corrosion test

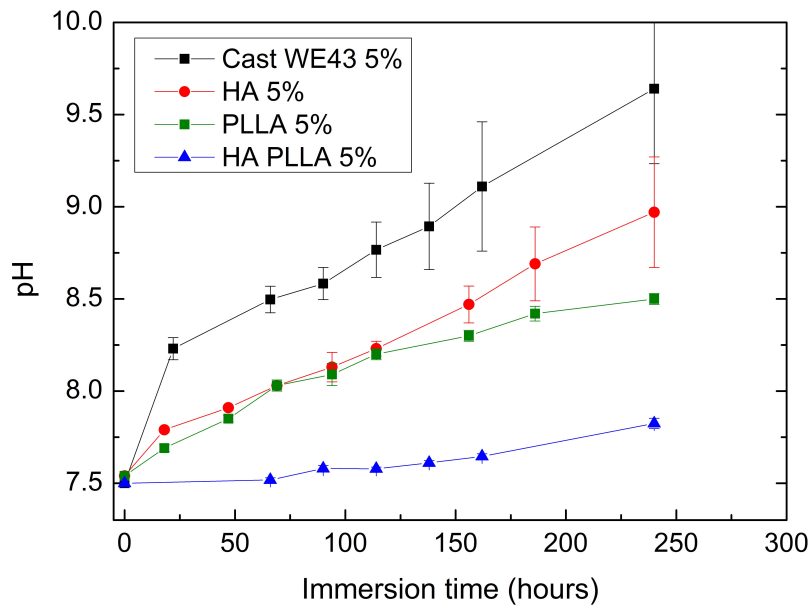
5.3.5.1 pH evolution

The corrosion resistance of cast WE43, HA coated WE43, PLLA coated WE43 and dual HA-PLLA coated WE43 was evaluated by immersing the specimens into SBF for 10 days and by monitoring the pH of the solution over the entire period. The results are presented in figure 5.7 where the pH evolution as a function of immersion time was measured for non-strained (a) and strained specimens (b). Without deformation, it can be seen that all coated-WE43 samples showed better resistance than untreated cast WE43 for which the pH of the solution increased dramatically in the first hours of immersion to reach a final value of 9 after 240 hours. This pH increase, associated to the release of hydroxide ions OH^- during corrosion, was reported to be inappropriate for cells growth and proliferation [46]. In particular, dual HA-PLLA coating provided good protection to the substrate with a very low pH increase over the immersion period. Although no strain was applied to the sample, it can be seen that the pH of the solution with PLLA coated WE43 sample increased linearly until reaching a value slightly higher than 8.5 after 240 hours immersion. This result is attributed to the very low adhesion of polymers to metallic surfaces, previously mentioned. Although PLLA layer maintained a good adhesion to WE43 under deformation in dry (air) conditions (fig. 5.5 (c)), it was observed that the PLLA layer entirely detached from WE43 when immersed into SBF, causing the exposure of magnesium to the liquid solution and its early corrosion.

After applying a 5% tensile strain to the specimens, the corrosion rate of cast WE43 was faster than before, with a final pH value of about 9.7 (figure 5.7 (b)). More interestingly, while HA coating provided good protection to WE43 when strain was not applied, a fast and important pH increase was observed under deformation, suggesting the exposure of Mg to the SBF solution and its subsequent corrosion. Also, it can be seen that the corrosion of HA coated WE43 occurred at a very fast rate since high pH values were measured already after 24 hours. This can be explained by the early contact of Mg with SBF due to the presence of cracks and delaminated areas, previously detected by SEM in the strained ceramic layer before immersion. In the case of PLLA coated WE43 sample, the pH evolution was very similar to that of the non-strained sample due to the detachment of the coating layer that also occurred under deformation. The best performance under tensile strain conditions was achieved with the HA-PLLA composite coated WE43 that almost did not undergo corrosion. The coating exhibited good resistance to strain and good stability in simulated body fluid, with almost no pH change. It must be noted that after 150 hours immersion, small defects appeared at the sharp angles of the edges on the samples, leading to a small increase of the pH, leading to an increase of the pH of the solution.



(a)



(b)

FIGURE 5.7: pH evolution as a function of immersion time in SBF of cast WE43, HA coated WE43, PLLA coated WE43 and HA-PLLA coated WE43 in the case of (a) before deformation and (b) after application of 5% tensile strain deformation.

5.3.5.2 Hydrogen H_2 gas release

The amount of hydrogen H_2 gas released during the immersion of the specimens into 80 mL SBF was also monitored over the same period of 10 days to evaluate the risks of hydrogen gas pockets formation. Figure 5.8 depicts the H_2 gas evolution as a function of the immersion time, of the non-strained (fig. 5.8 (a)) and 5% strained magnesium alloy specimens (fig. 5.8 (b)). Before deformation, it can be seen that the amount of hydrogen gas released from cast WE43 sample

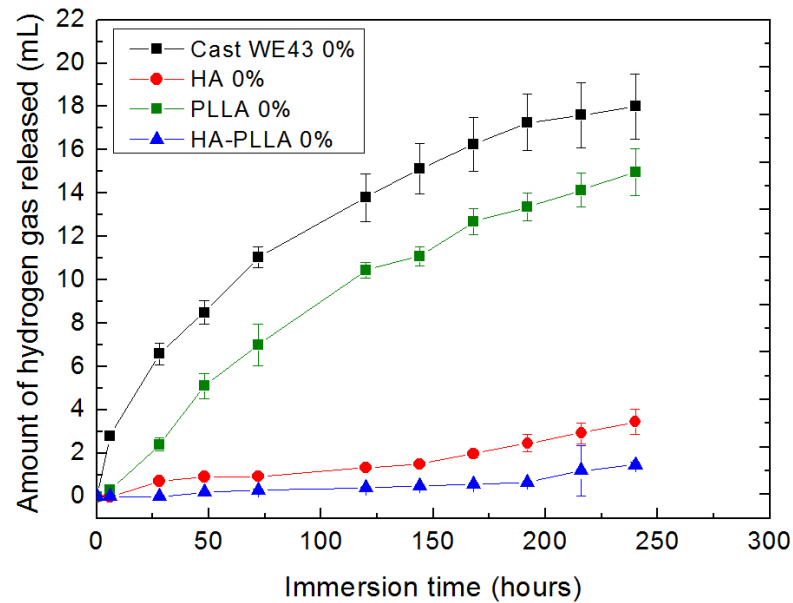
increased tremendously, already reaching 11 mL after 72 hours. After 240 hours of immersion (10 days) no saturation was observed and a value of about 19 mL of hydrogen gas was measured which might cause the formation of gas bubbles and severe damages if implanted into the body. PLLA coated WE43 did not prevent the release of hydrogen gas, with values of 15 mL after 10 days, due to the detachment of the layer from the substrate and the exposure of magnesium to the SBF. However, in the case of HA coated WE43 and HA-PLLA coated WE43, the amount of H₂ gas released was severely reduced, less than 3 mL, owing to a good protection provided by the ceramic layer and the composite layer.

After deformation, the hydrogen gas evolution for cast WE43 and PLLA coated WE43 was relatively similar than before deformation. However, in the case of HA coated WE43 sample subjected to deformation, high amount of gas was released with a value of 12 mL after 10 days immersion. This value of almost half the amount of the gas released from cast WE43 is too high and might lead to the formation of gas bubble under the skin. This result is also in good agreement with the previous results that showed an increase of pH for HA coated WE43 subjected to strain, suggesting the occurrence of corrosion and the non-efficiency of HA coating under strain. Finally, it can be seen that HA-PLLA coated WE43 can provide safe conditions for the human body with almost no release of hydrogen gas (2 mL) after 10 days.

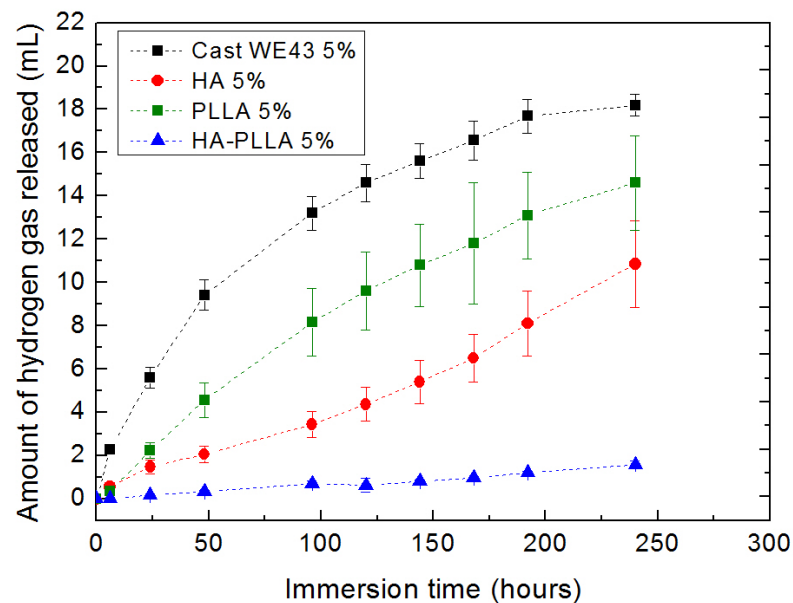
5.3.5.3 Mg ions concentration

The Mg ions concentration in the SBF solution was also measured after 1, 4 and 7 days of immersion into SBF to further characterize the corrosion state of the specimens. Figure 5.9 (a) displays the Mg ions concentration released from the non-strained specimens while figure 5.9 (b) displays the Mg ions concentration released from the 5% strained specimens. As expected, the fast corrosion rate of cast WE43 and the detachment of PLLA coating layer from the substrate led to high concentrations of Mg ions in the 15 mL SBF used for the experiment, with values reaching about 800 ppm and 600 ppm, respectively (figure 5.9 (a)). Surprisingly, a moderate quantity of Mg ions was released from HA coated WE43 sample after 7 days, with a value of about 300 ppm, although no much corrosion seemed to occur over the period of immersion, according to the pH test. As a comparison, the Mg ions concentration in SBF with immersed MgF₂-HA coated pure magnesium sample was of about 100 ppm after 3 days in SBF [5]. HA-PLLA coating provided good protection to WE43 with only 150 ppm of Mg ions measured in the SBF after 7 days.

When a 5% tensile strain was applied to the specimens, the Mg ions concentration released from HA coated WE43 sample reached the same level of ≈ 700 ppm than the one released from PLLA coated WE43, indicating a severe degradation of HA coating and an important quantity of magnesium present in the media. This result confirms the pH increase illustrated in figure 5.9.



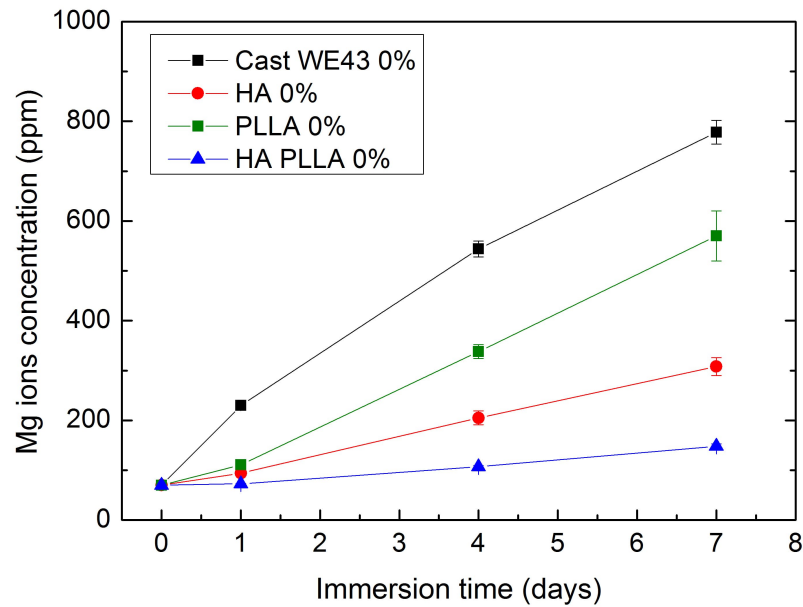
(a)



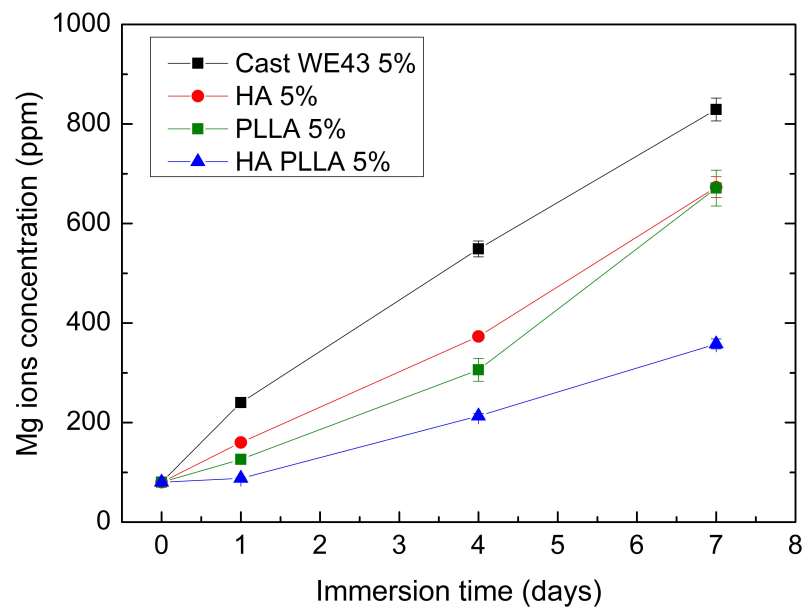
(b)

FIGURE 5.8: Hydrogen gas evolution during immersion into SBF of cast WE43, HA coated WE43, PLLA coated WE43 and HA-PLLA coated WE43 (a) before deformation and (b) after application of 5% tensile strain deformation.

In the case of dual HA-PLLA coated WE43, a level of 360 ppm was measured in the solution after 7 days, which is believed to be come from the small defects appearing at the sharp angles of the edges of the specimen after some period of time, as mentioned in the previous paragraph. Nevertheless, this concentration is quite similar with that of HA coated WE43 without strain, known for providing good corrosion resistance to the material.



(a)



(b)

FIGURE 5.9: Magnesium ions concentration in SBF solution as a function of immersion time of cast WE43, HA coated WE43, PLLA coated WE43 and HA-PLLA coated WE43 in the case of (a) 0% tensile strain and (b) 5% tensile strain.

5.3.5.4 Surface morphology after 10 days into SBF

After 10 days immersion into SBF, the specimens subjected to 5% strain were taken out of the solution and their surface morphology analyzed by SEM. Without any protection, the surface of cast WE43 was severely corroded with the presence of corrosion pits and multiple cracks (figure 5.10 (a)). A fast degradation rate was observed since the sample started crumbling after few days, causing a fast increase of pH and the release of magnesium particles in the solution. The

application of HA coating on the surface of the alloy did not show much efficiency under tensile strain conditions due to the brittle behaviour of HA. Figure 5.10 (b) reveals the damaged HA coating layer after 10 days immersion into SBF solution. As it can be seen the coating layer was severely cracked and magnesium was not protected in some areas of a size of hundreds of microns, explaining the high Mg ions concentration found in the solution. Moreover, the local exposure of magnesium led to localized corrosion pits, sometimes very deep and able to reach the width of the specimen, as shown in figure 5.10 (c), responsible of the release of OH^- ions and the associated increase of pH. In the same way, deposition of a PLLA layer on WE43 did not provide protection to the sample. As illustrated in figure 5.10 (d), corroded magnesium was found under the polymer layer that peeled off during immersion into simulated fluid. The surface morphology of dual HA-PLLA coated WE43 subjected to 5% strain and immersed for 10 days is displayed in figure 5.10 (e) and (f). As it can be seen, no detachment of the PLLA layer occurred, suggesting a good adhesion to HA, and no major degradation of the sample was detected. It is worth noting that the small defects observed at the edge of the dog bone shape specimen (left-hand side of figure 5.10 (e)) sometimes led to localized corrosion pits, explaining the moderate amount of Mg ions found in the solution after several days. At higher magnification (fig. 5.10 (f)), only small cracks of a length of tens of microns were spotted in the polymer layer.

5.3.6 Mechanical stability

Given that an implant should sustain mechanical integrity over the bone healing period, the combination of strength and strain of cast WE43 and coated WE43 specimens after 10 days immersion into SBF was evaluated by the mean of tensile tests. Figure 5.11 presents the toughness results of each specimen, before and after deformation (the values of the tensile strength are also given in figure 5.12 as a complementary information). While the toughness of cast WE43 after 10 days immersion into SBF was about 274 MJ.cm^{-3} it can be seen that the three kind of coatings, namely HA, PLLA and HA-PLLA, helped the alloy to reach even higher toughness values, especially in the case of PLLA coating as the tensile toughness increased up to $\approx 340 \text{ MJ.cm}^{-3}$. It seems therefore that the peeling of the polymer layer previously observed does not severely affect the mechanical properties of the structure. This can be explained by the fact that corrosion occurred uniformly over the surface of the sample, resulting in superficial defects only.

When the coated specimens received a 5% strain deformation before immersion into SBF, the results were significantly different. The mechanical properties of cast WE43 dropped significantly with a toughness value of 57 MJ.cm^{-3} , which seems too weak to be aimed at load bearing applications. The formation of pits and cracks in HA coated WE43 after deformation and immersion for 10 days into SBF resulted in very poor mechanical properties with a tensile toughness of about 31 MJ.cm^{-3} . Deep corrosion pits, such as illustrated in figure 5.10 (c) represent

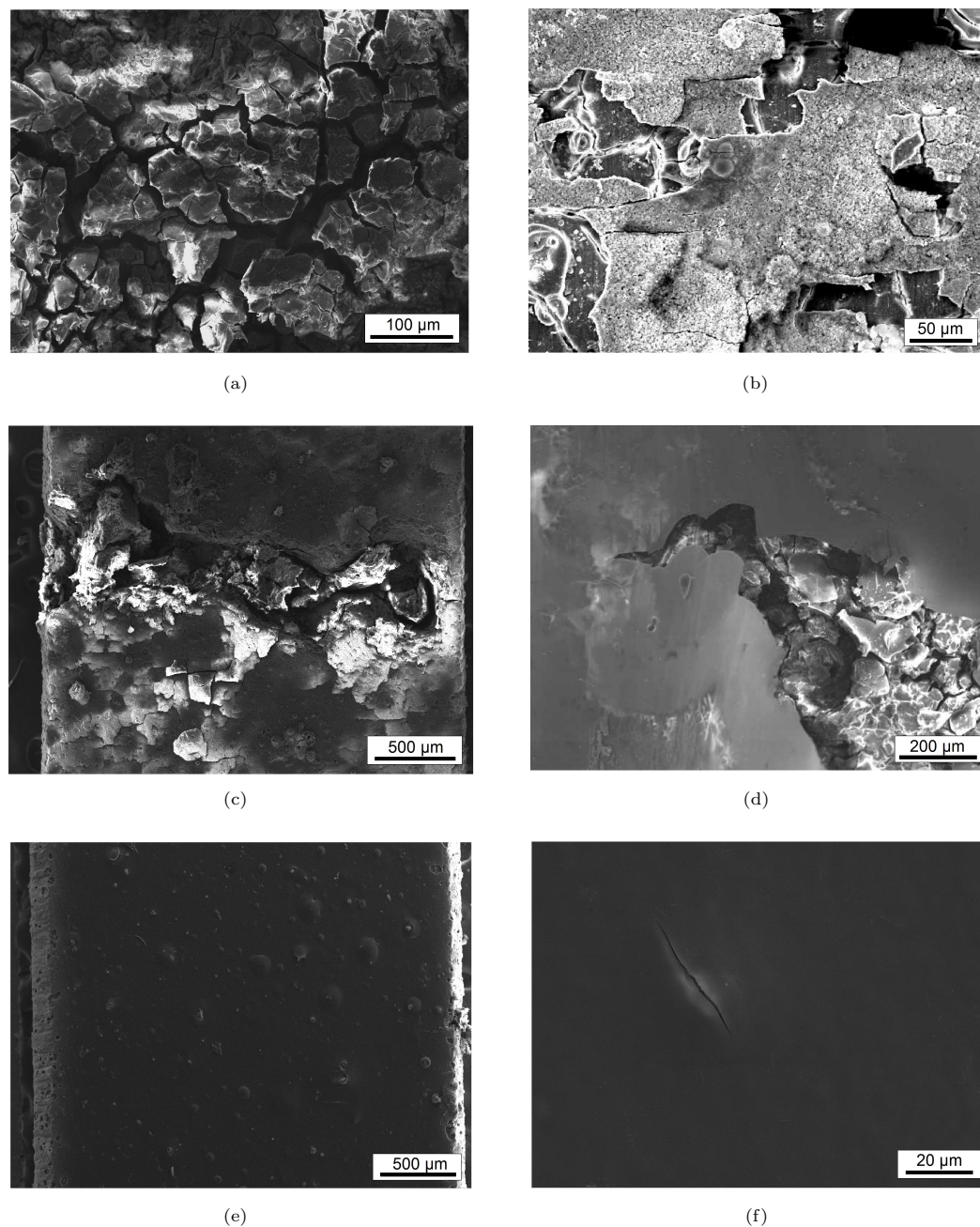


FIGURE 5.10: SEM images showing the surface morphology of (a) cast WE43, (b) HA coated WE43 at high magnification and (c) low magnification, (d) PLLA coated WE43 and (e) dual HA-PLLA coated WE43 at low magnification and (f) high magnification, after deformation and 10 days immersion into SBF.

important structural defects that initiate premature failure due to stress concentration located at these areas, and therefore to very low tensile properties. After deformation, PLLA coated WE43 sample showed a very good mechanical behaviour after immersion, with a tensile toughness of $\approx 195 \text{ MJ.cm}^{-3}$, a value of more than three times the toughness of cast WE43 in the same conditions. Like in the unstrained conditions, the absence of severe defects or corrosion pits after peeling of the polymer layer did not lead to high loss of mechanical integrity. Nevertheless the best

mechanical performance under tensile deformation was reached with HA-PLLA composite coated WE43 sample that exhibited a tensile toughness of $\approx 217 \text{ MJ.cm}^{-3}$ after 10 days immersion. More interestingly, this value was very similar to the one dual HA-PLLA coated alloy before deformation, suggesting the good stability of the coating under deformation.

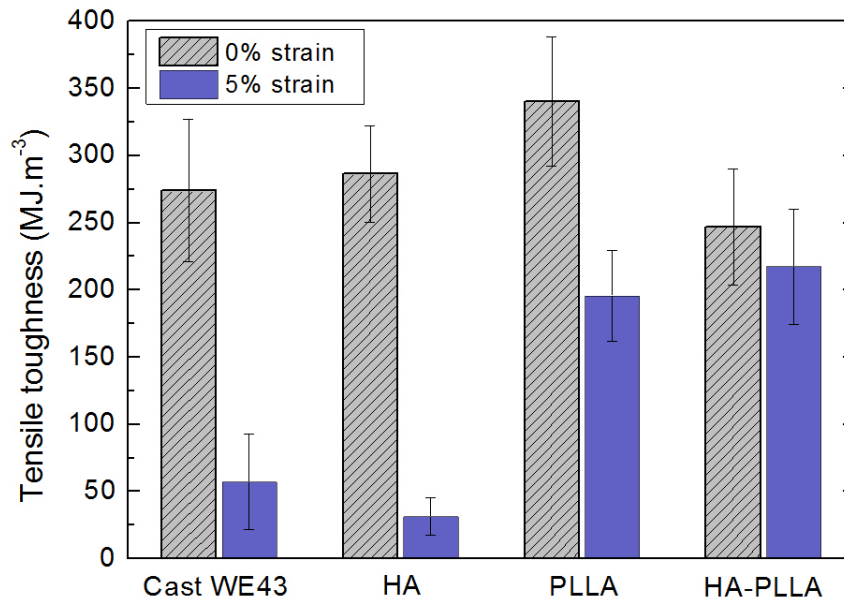


FIGURE 5.11: Tensile toughness measured after 10 days immersion into SBF of cast WE43, HA coated WE43, PLLA coated WE43 and dual HA-PLLA coated WE43, before and after application of 5% strain deformation.

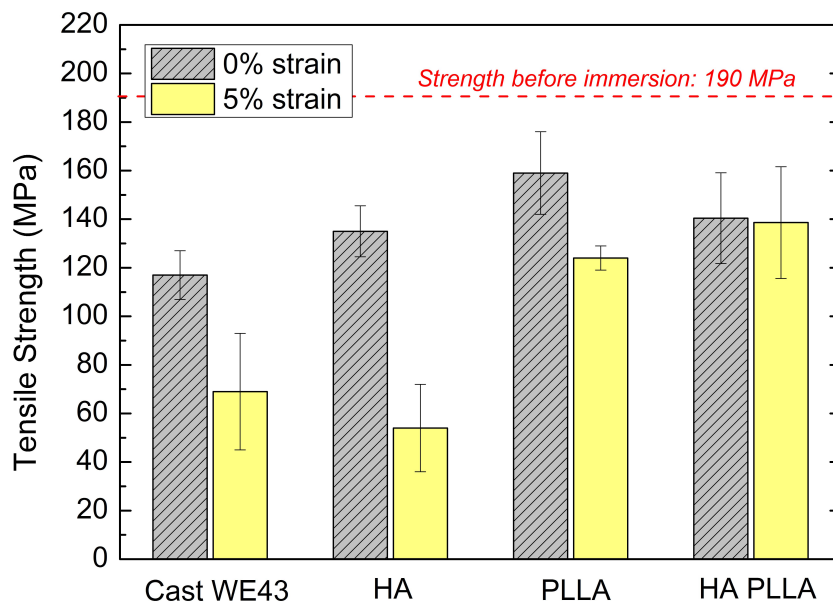


FIGURE 5.12: Tensile strength measured after 10 days immersion into SBF of cast WE43, HA coated WE43, PLLA coated WE43 and dual HA-PLLA coated WE43, before and after application of 5% strain deformation.

5.3.7 In-vitro cell responses

5.3.7.1 Cell attachment observed by optical microscope

In-vitro cell tests were performed using MC3T3 preosteoblast cells to evaluate the biological properties of cast WE43 and coated WE43 specimens, including cells attachment and proliferation. SEM images of the MC3T3 cells that were cultured for 2 days on cast WE43, HA coated WE43, PLLA coated WE43 and dual HA-PLLA coated WE43 samples in the non-strained and strained conditions are shown in figure 5.13. As it can be seen only few cells were attached to the corroded surface of cast WE43, in both non-strained (a) and strained (b) conditions. However, the cytocompatibility of WE43 magnesium alloy was greatly improved by coating its surface, with good cell responses on HA coated WE43 (c), PLLA coated WE43 (e) and dual HA-PLLA coated WE43 (g). Multiple cells were attached on all coating layers and spread with an active cytoskeletal extension. From the SEM images the three different kinds of coating seemed to show a good cytocompatibility and no conclusion can be drawn as for the best cell attachment conditions.

However, when a 5% strain was applied, a loss of biological response was observed with the HA coated WE43 sample due to corroded state of the sample after 2 days immersion into SBF. Cracks, release of Mg ions in the medium, increase of pH and eventually release of hydrogen gas did not provide suitable environment to the cells, resulting in very small amount of cells attached to the calcium phosphate based layer. Moreover, the few cells found on the surface of the sample did not spread well, as illustrated in figure 5.13 (d), suggesting a low affinity for the substrate. In the case of PLLA coated WE43, the cell response also decreased when tensile strain was applied to the sample. Fewer cells attached to the coating layer and their filopodia was not well spread but rather very close to the nuclei, as appearing in figure 5.13 (f). Although no peeling of the polymer layer was observed in the specimen due to the short period of immersion in the cell medium (2 days), several cracks of a length of hundreds of microns were spotted in the coating layer, exposing magnesium to the medium and resulting in the subsequent occurrence of corrosion. In contrast, HA-PLLA coating exhibited minor damages after 2 days immersion into the medium, resulting in a good cell attachment with multiple cells observed on its surface. The cells were well spread and maintained an active cytoskeletal-shape extension, like in the non-strained conditions.

5.3.7.2 Cell attachment observed by con-focal microscope

The cells morphology and their affinity to the different specimens subjected to tensile strain were also studied by confocal laser scanning microscopy (CLSM) after 3 days culturing and the results presented in figure 5.14. First, it can be seen that no cells were found on the surface of

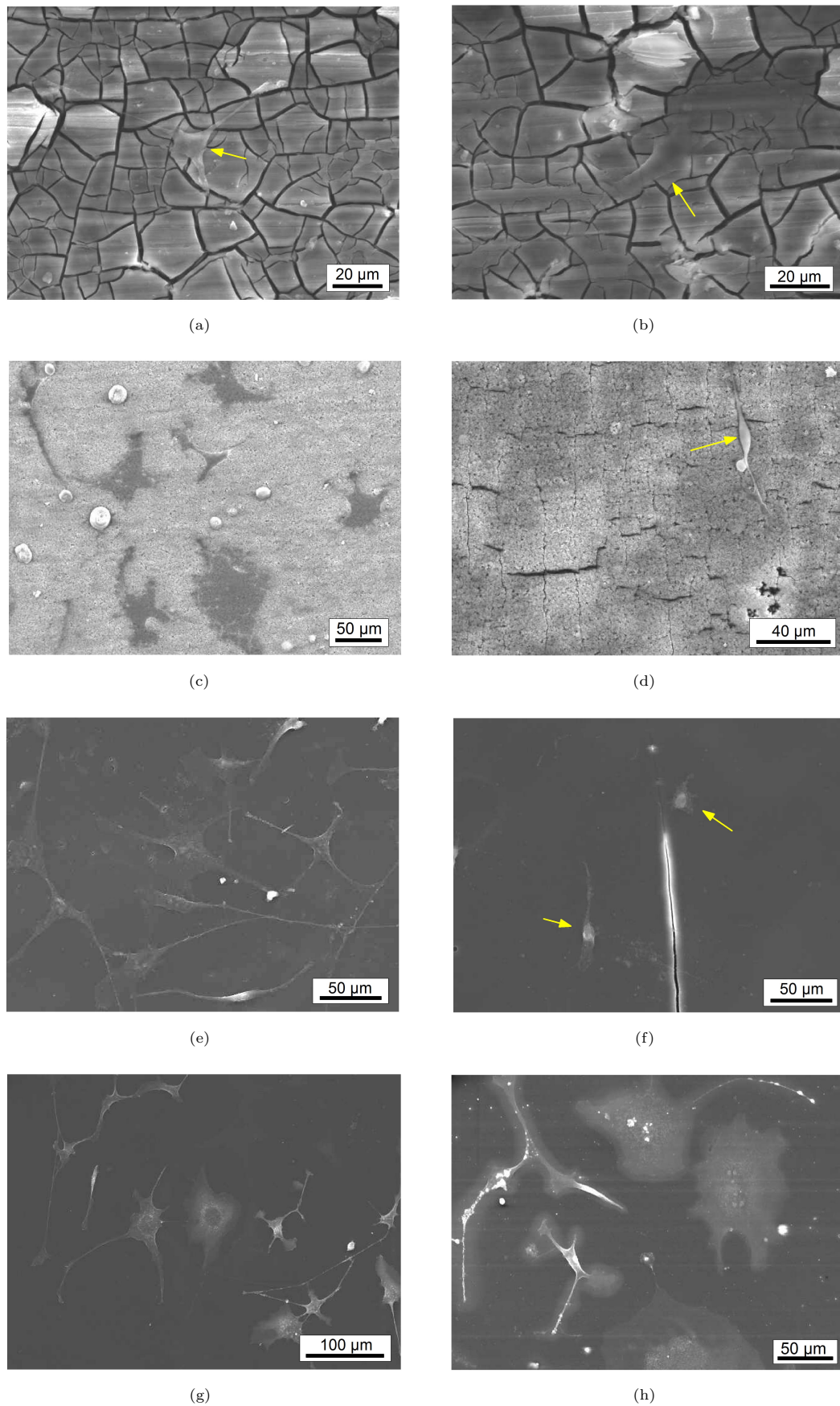


FIGURE 5.13: SEM images of the MC3T3 osteoblast cells that were cultured for 2 days on (a) cast WE43, (b) 5% strained cast WE43, (c) HA coated WE43, (d) 5% strained HA coated WE43, (e) PLLA coated WE43, (f) 5% strained PLLA coated WE43, (g) HA-PLLA coated WE43 and (h) 5% strained HA-PLLA coated WE43.

cast WE43 (a) after 3 days immersed in the cell medium. The morphology of the cells attached to HA coated WE43 (b) also confirms the previous SEM observation of a poor affinity for the damaged ceramic coating, with few cells observed and poor extension of the filopodia (red part). This result was very similar in the case of PLLA coated WE43 (c). However, the CLSM image of dual HA-PLLA coated WE43 in figure 5.14 (d) indicates a good cytocompatibility with the sample, especially in reference with the large extension of the cell filopodia around the nuclei, most of the time in a circular shape, that promotes adhesion with the substrate, linking the cells to it (figure 5.14 (f)). Therefore, it can be concluded that HA-PLLA coating can maintain a good biocompatibility under deformation.

5.3.7.3 Cell proliferation

In figure 5.15, the cells proliferation was assessed by quantifying the DNA levels of the cells cultured for 3 days on cast WE43 and coated WE43 specimens. The DNA amount of untreated WE43 magnesium alloy was very low, close to $0.002 \mu\text{g}$ and $0.0015 \mu\text{g}$, in the non-strained and strained conditions, respectively. However, it can be seen that the ability of the cells to proliferate was greatly improved when the alloy was coated, especially in the case of HA coating with DNA values reaching $0.008 \mu\text{g}$. The proliferation levels of PLLA coated WE43 and HA-PLLA coated WE43 were reasonably similar to each other, in the range of $0.055 \mu\text{g}$. The application of 5% strain led to a severe overall decrease of DNA levels, as a consequence of the loss of the biological response of the deformed samples, previously highlighted with the cell attachment tests. The most dramatic decrease of cell proliferation was observed for HA coated WE43 as the DNA amount dropped from $0.008 \mu\text{g}$ to $0.0032 \mu\text{g}$. In the case of PLLA coating the loss was less pronounced, with DNA values decreasing from $0.0055 \mu\text{g}$ to about $0.0028 \mu\text{g}$. It seems therefore that after 3 days culturing, the PLLA layer did not detach from the substrate, in which such case the DNA levels would have been more lower. In the case of HA-PLLA coating, the application of tensile strain did not severely affect the cell proliferation since the decrease of DNA values was limited, from $0.0055 \mu\text{g}$ in the non-strained conditions to $0.004 \mu\text{g}$ in the strained conditions. These results indicate that the application of dual HA-PLLA coating enabled to improve the in-vitro cellular response of WE43, as compared to when HA and PLLA were used as single coating layers.

5.4 Discussion

In this study the effect of the presence of a HA layer between PLLA and WE43 on the corrosion resistance, biocompatibility and stability of the coating under deformation has been investigated.

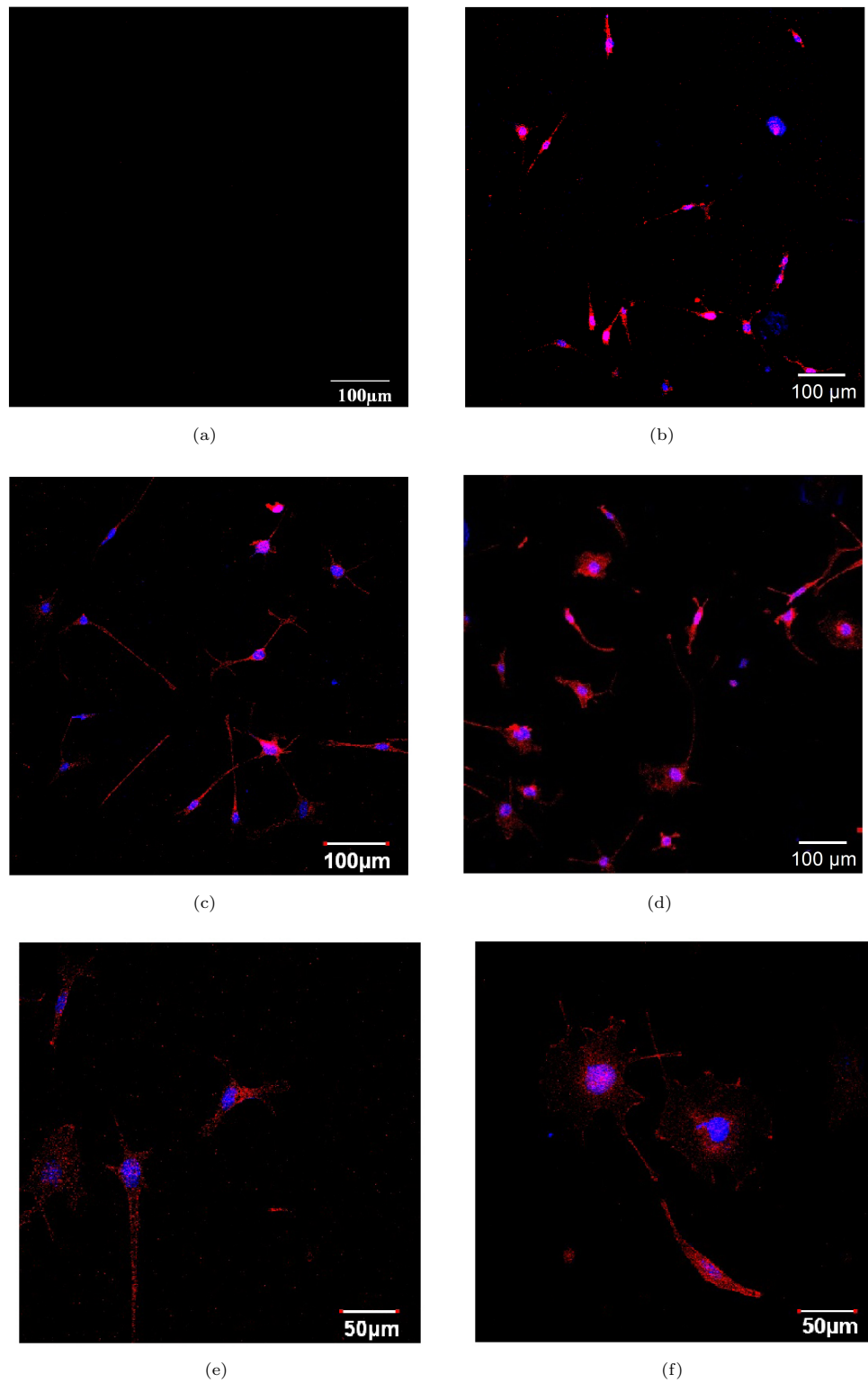


FIGURE 5.14: CLSM images of the MC3T3 osteoblast cells that were cultured for 3 days on 5%strained (a) cast WE43, (b) HA coated WE43, (c) PLLA coated WE43 and (d) HA-PLLA coated WE43. High magnification of the filopodia in the case of PLLA coated WE43 and HA-PLLA coated WE43 can be seen in (e) and (f), respectively.

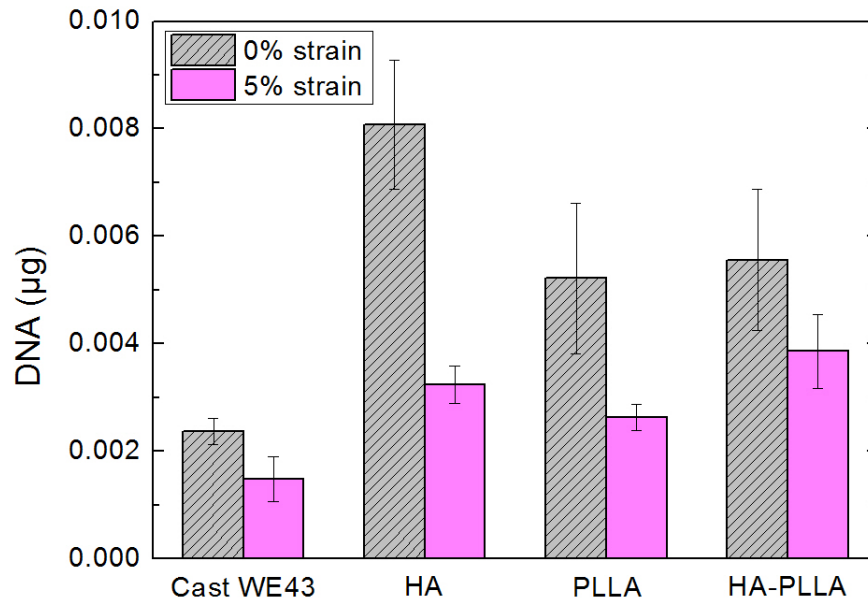


FIGURE 5.15: DNA levels of the MC3T3 osteoblast cells that were cultured for 3 days on the cast WE43, HA coated WE43, PLLA coated WE43 and HA-PLLA coated WE43 specimens, after and before application of 5% strain.

A first treatment of WE43 magnesium alloy in aqueous solution containing calcium and phosphate sources resulted in the formation of a needle-like shape HA layer with a thickness of about 3-4 μm . Unlike previous results reported in the literature, the layer exhibited no defect and was formed uniformly over the surface of the alloy. Annealing the material at high temperature prior to treatment was found to be a necessary condition to obtain such result. The adhesion strength of the HA layer to the substrate was about 16 MPa which fulfils the requirements of coatings deposition for bio-implants. As a second treatment, a PLLA layer was deposited on HA by dip coating technique, with a suitable viscosity for the polymer to infiltrate well between the HA needles, providing good bonding between the two layers of a total thickness of 7-8 μm .

It was first found that the composite coating conferred good corrosion resistance to WE43 under deformation over a period of 10 days. While HA and PLLA single coatings experienced damages such as cracks, delamination or detachment when immersed into simulated body fluid, dual HA-PLLA coating sustained a good morphology with no major defects. Although cracks appeared in the HA interlayer, PLLA served as a barrier and largely inhibited the penetration of SBF into the cracks and its subsequent contact with magnesium substrate. Therefore, the in-vitro corrosion tests revealed no sign of significant corrosion with dual coating, with reduced pH increase, hydrogen gas and less Mg ions released in the media compared to HA and PLLA single coatings. Moreover, since the polymer layer did not detach from the substrate when used as part of a composite coating, it can safely be assumed that HA helped to improve the bonding strength between PLLA and WE43.

The mechanical integrity of dual HA PLLA coated WE43 was preserved after 10 days of immersion in simulated body fluid due to the good stability of the coating layer under deformation. While HA coated WE43 sample experienced premature failure owing to the presence of corrosion pits in the structure, no loss of mechanical properties of composite coated WE43 occurred after the application of strain.

An other relevant effect of using HA-PLLA coating for bio-implants is the cells response improvement. Due to the good stability of dual coating under deformation, a good biocompatibility was observed during in-vitro cell tests, owing to the exposure of PLLA layer to the cell medium. Cells attached well to the coating with a flattened shape and very good extension of filopodia, suggesting their good adhesion to the substrate. Although HA single coating showed a better bioactivity in non-strained conditions, due to its similar composition with that of the bone, the application of deformation severely affected the cellular response, as a consequence of the presence of cracks and the occurrence of bio-corrosion that did not provide suitable environment for the cells. In the same way, the formation of cracks in PLLA layer during the first days of immersion into cell medium resulted in fewer cells attached to the implant, combined with a not good extension of their filopodia. Cells proliferation test confirmed these results as the highest DNA levels after deformation was measured for composite coated sample after 3 days culturing.

However, the work achieved in this study presents the limitation of possible occurrence of corrosion with exposure time in solution. While PLLA layer serves as a barrier between the cracked HA layer and the medium 5.16 (a), it can happen that a cracks propagation from the HA layer to the PLLA layer occurs, as shown in fig 5.16 (b). As a consequence, the damaged ceramic layer can be exposed to the medium (c), resulting in a possible loss of performance. Nevertheless, the results presented in this study have shown the clear advantage of using hydroxyapatite as an interlayer to improve the adhesion of PLLA to the substrate. A reduction in HA layer thickness might optimise the concept of this study.

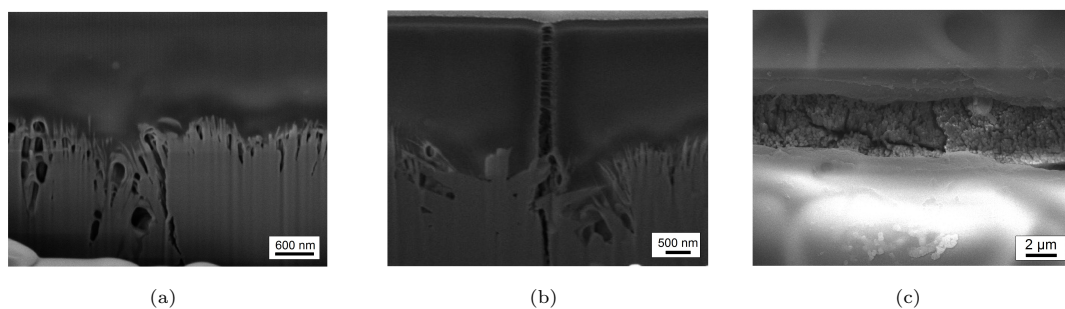


FIGURE 5.16: Cross section of HA-PLLA coated WE43 subjected to 5% strain (before immersion) when (a) PLLA acts as a protective layer, (b) when a crack propagation occurs from HA layer to PLLA layer. After immersion in SBF for several days, (c) the crack in PLLA has opened up and the damaged HA layer was exposed to the medium.

5.5 Conclusion

In this work a new two-steps coating technique involving a conversion process to form hydroxyapatite in conjunction with a deposition technique to apply poly-L-lactid acid was presented to fabricate a strain resistant composite coating for WE43 magnesium alloy. The combination of a ceramic layer and a flexible polymer layer has allowed the cancellation of the drawbacks associated with these two materials, namely a brittle behaviour and a low bonding strength to the substrate.

In-vitro tests showed that the composite coating provided good corrosion resistance to the magnesium substrate and sustained a good biocompatibility when the alloy was subjected to deformation. Analysis of the morphology of the coating after several days of immersion in body fluid-like solution revealed its good stability with no major defects or damages observed in the layer coating, enabling the implant to maintain enough strength for load bearing applications.

Chapter 6

Conclusion and future work

6.1 Conclusion

The work presented in this thesis was aimed at developing a magnesium-based implant structure that fulfills the two main requirements necessary to the development of such biodegradable devices, namely good mechanical properties and a low corrosion rate together with a good compatibility.

Firstly, the deformation mechanisms in HCP metals and the different SPD techniques usually employed to strengthen magnesium were reviewed in chapter 2. These techniques are often based on Hall-Petch relation that predicts an increase of strength as an inverse function of the grain size. However, due to the poor formability of magnesium attributed to a reduced number of available slip systems, deformation of magnesium by common SPD techniques such as ECAP must be carried out at high temperatures. Moreover, the mechanical anisotropy and the development of texture that promotes dislocation glide on basal planes and that dominates grain refinement can lead to a softening effect which is not a desirable effect. Finally most of SPD techniques are not suitable for industry scale production.

This is why a new SPD process referred as to three roll planetary milling, or PSW or even screw rolling, was introduced in chapter 3. This technique consists in processing the material at a very high speed and has flexibility with regard to the workpiece dimensions and rate of deformation, making it amenable to large scale production. It was also found that this technique is well suited for producing grain refinement up to 2-3 microns in the case of pure magnesium and that the associated texture evolution plays a key role in the mechanical behaviour of the material, in terms of strength and ductility. While the resulting structure is rather heterogeneous after one processing pass, it becomes more homogeneous as the number of passes increases. Also, the same range of yield strength of 109 MPa and 116 MPa was obtained after 1 pass and 6 passes of three

roll planetary milling respectively, while tensile ductility was significantly different in these two states, which is attributed to a special combination of grain size and texture. Deformation of pure magnesium at room temperature was achieved after 11 passes without cracks and without using any secondary device like back pressure. At this stage a yield strength level of the order of about 146 MPa and a UTS value in excess of 200 MPa were reached for pure magnesium, which is comparable with strength levels for magnesium alloys and that of the cortical bone. Chapter 3 has highlighted thus the potential of using the PSW process as a suitable process for the production of magnesium bone graft implants.

The rest of the study focused on WE43 yttrium-neodymium magnesium alloy, a promising candidate material for biomedical applications owing to its non toxicity and relatively low corrosion rate. In chapter 4, a new technique combining the three roll planetary process and an ageing treatment was developed to improve its mechanical properties and make it suitable for load bearing applications. After one pass of screw rolling no significant grain refinement occurred and a heterogeneous microstructure was observed. The strength enhancement from 140 MPa to 220 MPa was attributed to the development of a strong texture with (110) plane perpendicular to the extrusion direction. Interestingly, processing the alloy several times at the same temperature of 400°C does not give rise to a strength improvement and only a staggered reduction of the temperature between each pass, like in chapter 3, seems to be beneficial for the mechanical properties of the processed material. Another increase of strength was observed after thermal treatment at 210°C due to the formation of hardening precipitates that block the dislocations movement. The hardness measurements revealed that the strength of WE43 increases in the first stage of ageing with the formation of β' and β'' phase precipitates. Moreover the hardness of the processed and aged alloy was higher than that of the only aged alloy during that period, demonstrating the beneficial effect of screw rolling. After an ageing period of 16h, a loss of mechanical properties occurs with the development of β_1 precipitates.

Although it is claimed that SPD-processed materials exhibit higher corrosion resistance, no significant change in the corrosion behaviour of screw processed WE43 magnesium alloy was detected. A biocompatible surface coating aimed at reducing its corrosion rate was therefore proposed in chapter 5. Unlike the numerous coating solutions that have been proposed in the literature, the coating structure developed in this study was specifically design to resist to deformation and sustain protection under 5% strain, accordingly to the strain to failure of the cortical bone. It consisted in a HA ceramic - PLLA polymer composite coating fabricated by a two steps technique in which HA was formed by immersion in aqueous solution and PLLA deposited by dip coating technique. The combination of a ceramic layer and a flexible polymer layer allows the cancellation of the drawbacks associated with these two materials, namely a brittle behaviour and a low bonding strength to the substrate, with no defect or delamination of the coating observed when the sample was subjected to deformation and immersed into simulated

body fluid. The composite coating provides good corrosion resistance with no pH increase and few magnesium ions present in the solution. Moreover, the good stability of the coating under deformation enables the implant to maintain enough strength for its use for load bearing applications. Finally, a good cell response was observed, suggesting a good biocompatibility of the strained coated WE43 owing to the non damaged PLLA layer exposed to the outer environment.

6.2 Future work

In this thesis, new solutions to improve the mechanical properties of magnesium-based implants and reduce their corrosion rate under deformation were proposed, but some open questions remains. Here are presented the possible future directions of research and investigations.

The work carried out in chapter 4 proposes a new technique to improve the mechanical properties of WE43 magnesium alloy by combining a mechanical and thermal treatment. The results obtained with this technique were then compared with the ones obtained with a only thermal treatment, commonly encountered in the industrial environment. Nevertheless there are few aspects that are not entirely understood, for example, the hardness evolution in the two different magnesium samples presented in figure 4.16. The experimental results showed that the PSW process was efficient in improving the mechanical properties of WE43 in the first period of ageing only. After a long period of time the non-processed and aged sample exhibited the highest hardness values, suggesting the limited effectiveness of PSW process. Since the formation of hardening precipitates over the ageing period of 7 days was only analyzed in the processed and aged sample, the difference in hardness between the two kinds of samples is not entirely understood. TEM images revealing the phase precipitates formed in the aged sample would have brought useful information regarding the relationship between the hardness and the ageing time and between the two different samples.

Results presented at the end of chapter 4 showed that the effect of plastic deformation on the corrosion behaviour of WE43 was very limited due to the small microstructure changes and poor grain refinement observed in the alloy after one pass of screw rolling. Therefore, it would be more relevant to perform corrosion tests with pure magnesium after 11 passes of screw rolling, like obtained chapter 3. It is believed that the important grain refinement occurring after 11 passes severely impacts the relative anodic and cathodic reaction kinetics and leads to changes in the corrosion behaviour of the material, as proposed by D. Orlov [43]. In addition, no post-processing ageing treatment was carried out in the case of pure magnesium which prevents the risks of interference in the correlation of processing and corrosion behaviour.

Regarding the work presented in chapter 5, the composite coating used two layers of ceramic and polymer of the same thickness of about 3-4 microns. A limited efficiency was noticed after

a long period of time due to a possible crack propagation from the hydroxyapatite layer to the poly-L-lactid acid layer, promoting penetration of the simulated body fluid and early corrosion. Changing the design of the composite coating by reducing the thickness of HA would offer more stability and would sustain protection for a longer period of time as the ceramic layer would play the role of an interlayer rather than a dual layer. J.H. Jo et al. [5] have indeed highlighted the beneficial effect of a thin interlayer between the substrate and the coating layer.

Appendix A

Complete ODF data obtained in chapter 3

A.1 As received pure magnesium

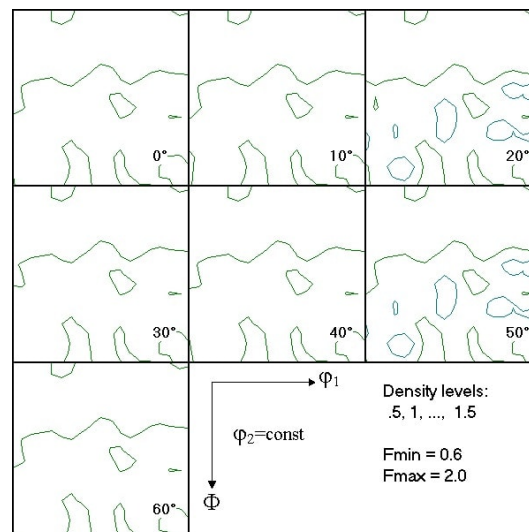


FIGURE A.1: ODF sections of pure magnesium in the as received conditions for $\varphi_2=0^\circ$ to $\varphi_2=60^\circ$.

A.2 Processed pure magnesium after 1 pass of PSW

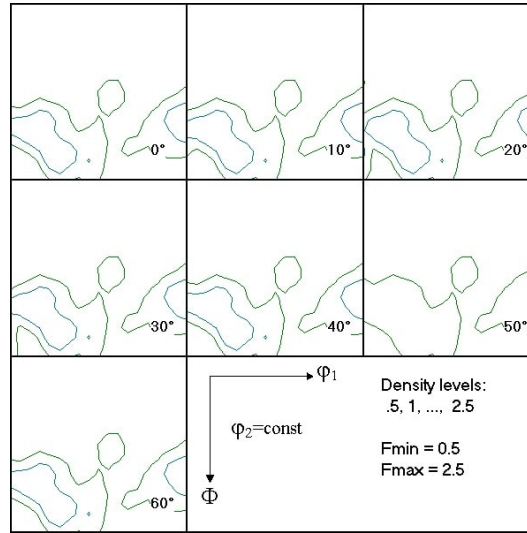


FIGURE A.2: ODF sections of pure magnesium after 1 pass of PSW for $\varphi_2=0^\circ$ to $\varphi_2=60^\circ$.

TABLE A.1: Summary of the ODF angles of processed pure magnesium after 1 pass of PSW.

number	φ_1	ϕ	φ_2	W	number	φ_1	ϕ	φ_2	W
1	3	64	0	0.001	12	86	61	30	0.0145
2	25	53	0	0.0045	13	113	65	30	0.0085
3	56	64	0	0.012	14	136	63	30	0.0145
4	91	65	0	0.0175	15	174	82	30	0.0085
5	147	65	0	0.0165	16	13	60	45	0.011
6	121	88	0	0.0025	17	69	62	45	0.004
7	157	88	0	0.0025	18	100	60	45	0.003
8	168	60	0	0.0115	19	156	71	45	0.0105
9	45	63	15	0.0095	20	165	90	45	0.0035
10	13	63	30	0.009	21				0.8255
11	23	76	30	0.01					

A.3 Processed pure magnesium after 6 passes of PSW

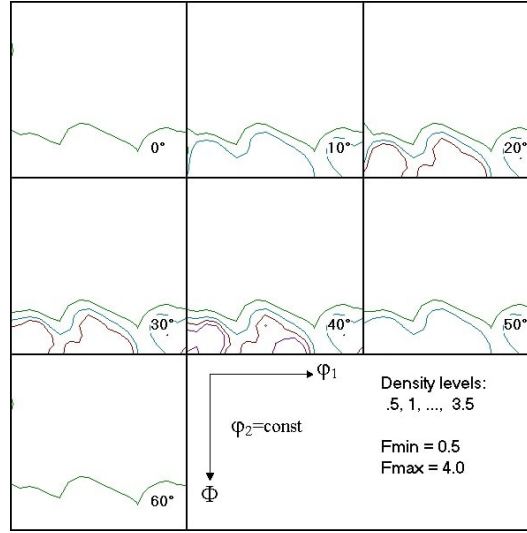


FIGURE A.3: ODF sections of pure magnesium after 6 passes of PSW for $\varphi_2=0^\circ$ to $\varphi_2=60^\circ$.

TABLE A.2: Summary of the ODF angles of processed pure magnesium after 6 passes of PSW.

number	φ_1	ϕ	φ_2	W	number	φ_1	ϕ	φ_2	W
1	11	70	0	0.004762	12	110	85	30	0.003636
2	100	61	0	0.003636	13	143	89	30	0.003636
3	100	90	0	0.003636	14	189	81	30	0.003636
4	143	83	0	0.003636	15	178	81	30	0.003636
5	174	84	0	0.003636	16	10	81	35	0.003636
6	15	90	10	0.003636	17	13	88	45	0.003636
7	51	81	10	0.003636	18	46	90	45	0.003636
8	74	82	10	0.003636	19	115	73	45	0.003636
9	110	85	10	0.003636	20	147	89	45	0.003636
10	53	88	30	0.003636	21	179	81	45	0.003636
11	78	78	30	0.003636	22				0.826

A.4 Processed pure magnesium after 11 passes of PSW

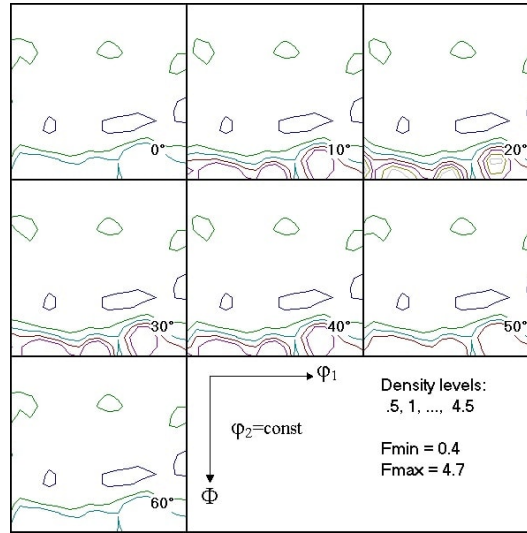


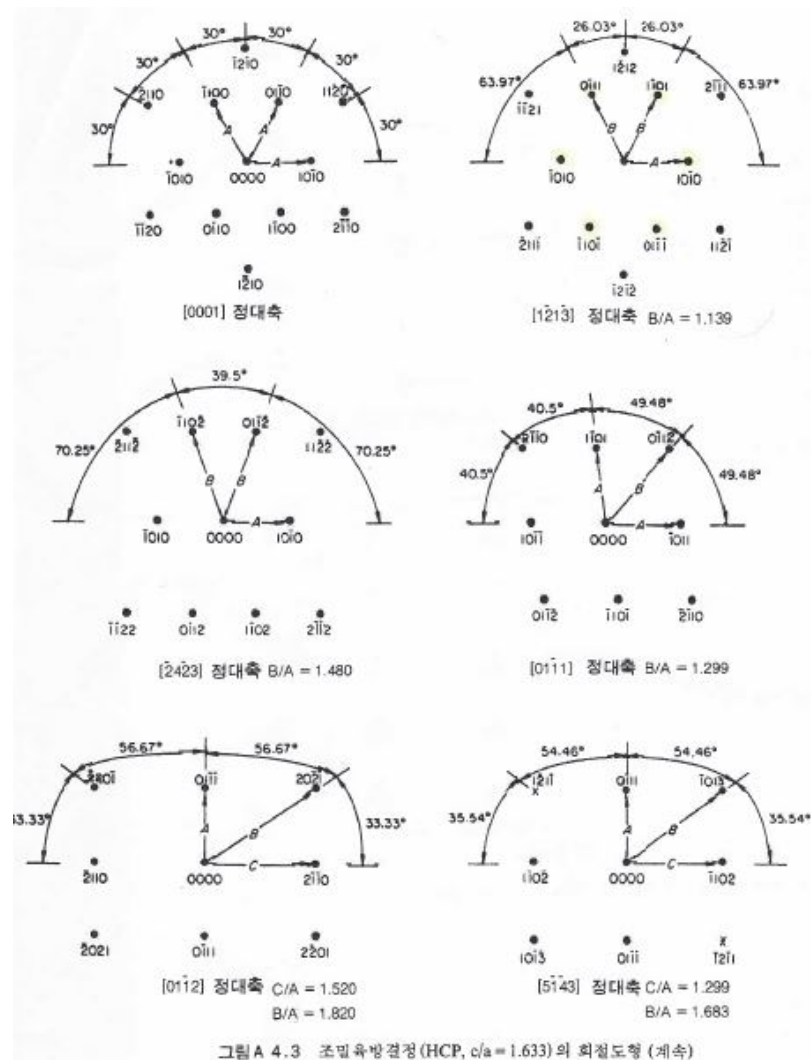
FIGURE A.4: ODF sections of pure magnesium after 11 passes of PSW for $\varphi_2=0^\circ$ to $\varphi_2=60^\circ$.

TABLE A.3: Summary of the ODF angles of processed pure magnesium after 11 passes of PSW.

number	φ_1	ϕ	φ_2	W	number	φ_1	ϕ	φ_2	W
1	157	84	0	0.010526	11	15	89	30	0.011579
2	136	88	0	0.010526	12	44	89	30	0.012632
3	70	89	0	0.007368	13	67	81	30	0.010526
4	85	56	0	0.005263	14	124	90	30	0.012632
5	96	89	0	0.005263	15	157	86	30	0.011579
6	18	87	15	0.013158	16	49	88	45	0.012105
7	53	88	15	0.014737	17	142	84	45	0.012105
8	121	81	15	0.012105	18	177	89	45	0.012105
9	160	77	15	0.012105	19	104	89	45	0.007895
10	104	89	20	0.010526	20				0.795

Appendix B

Theoretical diffraction pattern representation of magnesium



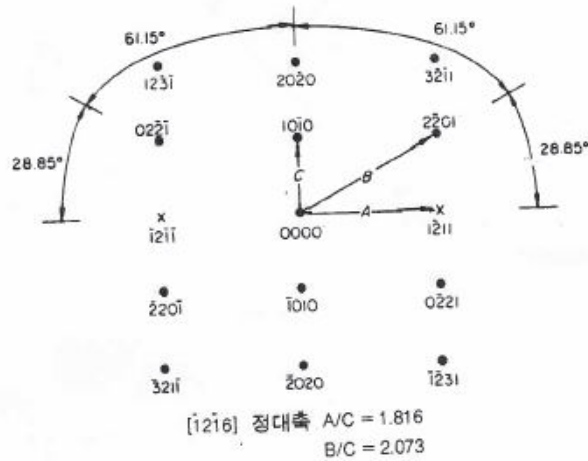
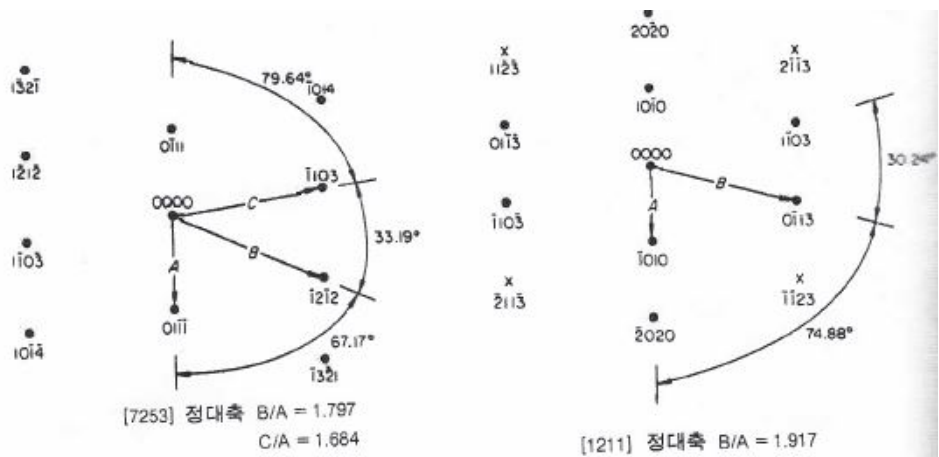
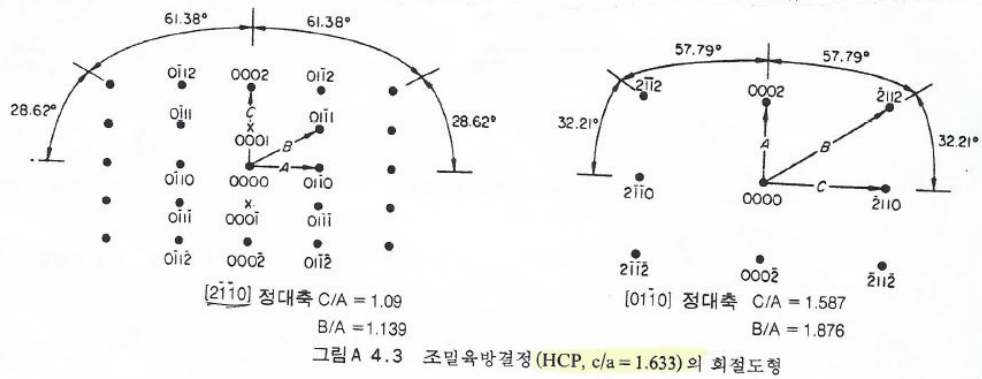


그림 A4.3 조밀육방결정 (HCP, $c/a = 1.633$) 의 회절도형 (계속)

Appendix C

Complete ODF data obtained in chapter 4

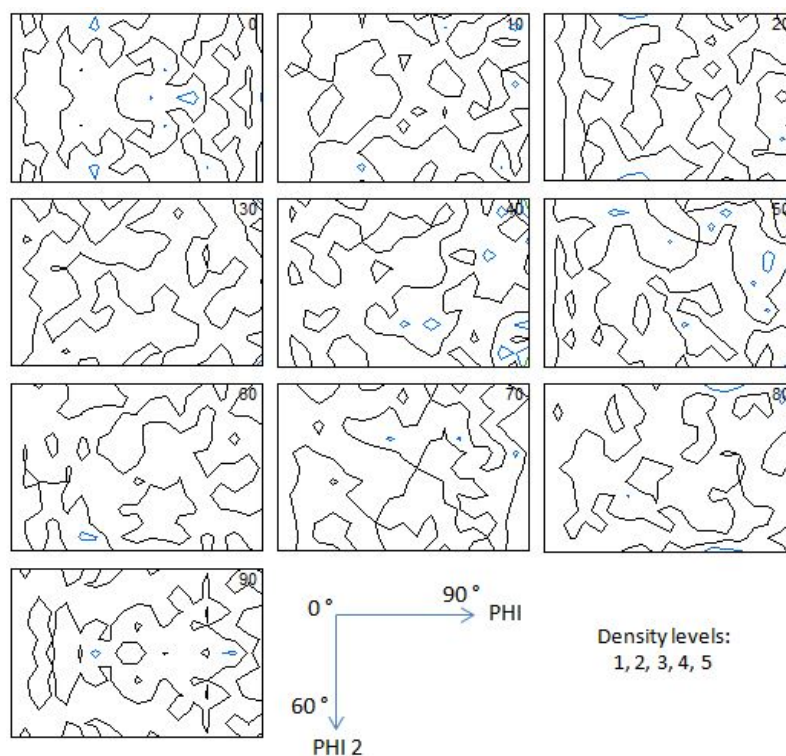


FIGURE C.1: ODF sections of cast WE43 magnesium alloy for $\varphi_1=0^\circ$ to $\varphi_1=90^\circ$.

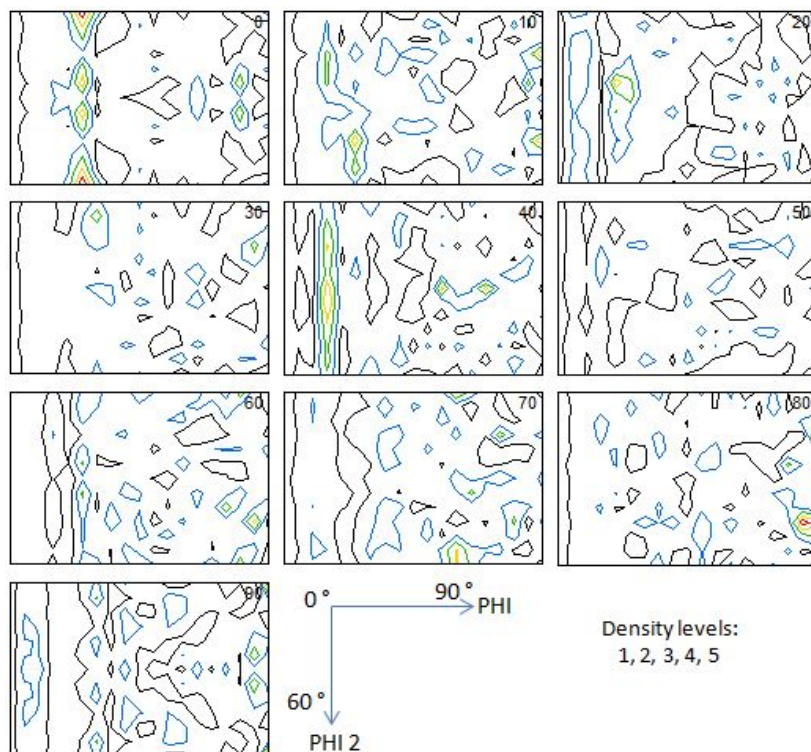


FIGURE C.2: ODF sections of WE43 magnesium alloy after annealing at 525°C for 5h, for $\varphi_1=0^\circ$ to $\varphi_1=90^\circ$.

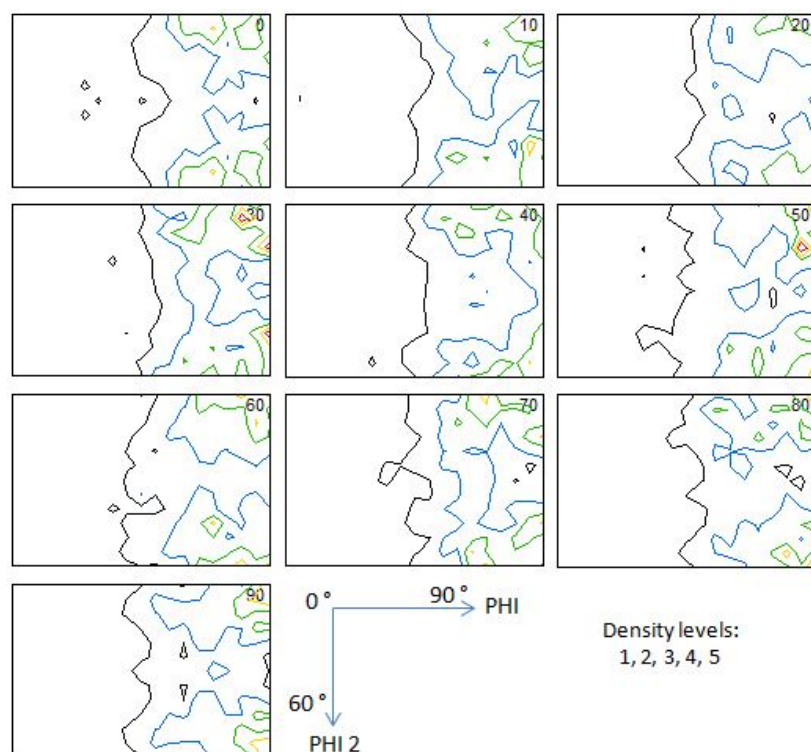


FIGURE C.3: ODF sections of WE43 magnesium alloy after 1 pass of PSW, for $\varphi_1=0^\circ$ to $\varphi_1=90^\circ$.

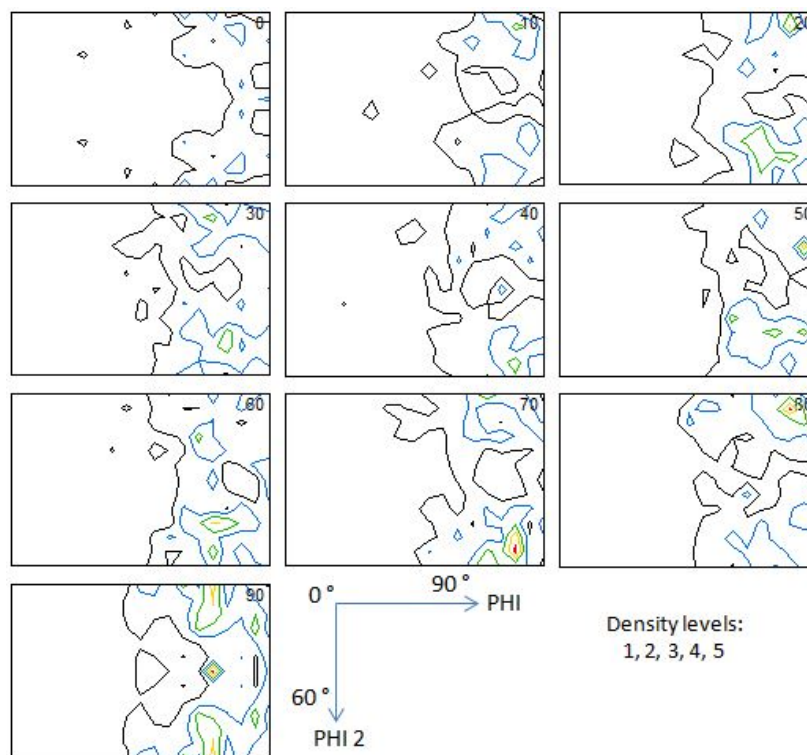


FIGURE C.4: ODF sections of WE43 magnesium alloy after processing and ageing treatment at 210°C for 16 hours, for $\varphi_1=0^\circ$ to $\varphi_1=90^\circ$.

Bibliography

- [1] S. Kim, J. Jo, M. Lee, M. Kang, H. Kim, Y. Estrin, J. Lee, J. Lee, and Y. Koh. Hydroxyapatite-coated magnesium implants with improved in vitro and in vivo biocorrosion, biocompatibility, and bone response. *J Biomed Mater Res Part A*, 102A:429–441, 2014.
- [2] M.Z. Bian. *Plastic Deformation Behavior of Magnesium Single Crystals*. Seoul National University, 2013.
- [3] G.D. Fan, M.Y. Zheng, X.S. Hu, K. Wu, and I.S. Golovin. Improved mechanical property and internal friction of pure mg processed by ecap. *Materials Science and Engineering A*, 556:588–594, 2012.
- [4] P. Mengucci, G. Barucca, G. Riontino, D. Lussana, M. Massazza, R. Ferragut, and E. Hassan Aly. Structure evolution of a we43 magnesium alloy submitted to different thermal treatments. *Materials Science and Engineering A*, 479:37–44, 2008.
- [5] J.H. Jo, B.G. Kang, K.S. Shin, H.E. Kim, B.D. Hahn, D.S. Park, and Y.H. Koh. Hydroxyapatite coating on magnesium with mgf2 interlayer for enhanced corrosion resistance and biocompatibility. *J Mater Sci: Mater Med*, 22:2437–2447, 2011.
- [6] M. P. Staiger, A. M. Pietak, J. Huadmaia, and G. Dias. Magnesium and its alloys as orthopedic biomaterials: A review. *Biomaterials*, 27:1728–1734, 2006.
- [7] M. Moravej and D. Mantovani. Biodegradable metals for cardiovascular stent application: Interests and new opportunities. *International Journal of Molecular Sciences*, 2011. URL www.mdpi.com/journal/ijms.
- [8] M. Avedesian and H. Baker, editors. *General Mechanical Behavior*. ASM International, 1999.
- [9] M.H. Yoo, J.R. Morris, K.M. Ho, and S.R. Agnew. Non basal deformation modes of hcp metals and alloys: role of dislocation source and mobility. *Metall. Mater. Transf. A*, 23A: 813–822, 2002.

- [10] Y. Estrin and A. Vinogradov. Extreme grain refinement by severe plastic deformation: a wealth of challenging science. *Acta Materialia*, 61:782–817, 2013.
- [11] E. Zhang, D. Yin, L. Xu, L. Yang, and K. Yang. Microstructure, mechanical and corrosion properties and biocompatibility of mgznmn alloys for biomedical application. *Materials Science and Engineering C*, 29:987–993, 2009.
- [12] F. Witte. The history of biodegradable magnesium implants: A review. *Acta Biomaterialia*, 6:1680–1692, 2010.
- [13] N. T. Kirkland. Magnesium biomaterials: past, present and future. *Corrosion Engineering, Science Technology*, 47:322–328, 2012.
- [14] A. Hruby and N. M. McKeown. *Chapter 36 Magnesium and Metabolic Syndrome: The Role of Magnesium in Health and Disease*. Elsevier, 2012.
- [15] B.B. Buldum, A. Sik, and I. Ozkul. Investigation of magnesium alloys machinability. *International Journal of Electronics: mechanical and mechatronics engineering*, 2:261–268.
- [16] Committee on benchmarking the technology and application of lightweighting. *Application*. 2012.
- [17] S.V. Dorozhkin. Calcium orthophosphate coatings on magnesium and its biodegradable alloys. *Acta Materialia*, 10:2919–2934, 2014.
- [18] F. Witte, V. Kaese, H. Haferkamp, E. Switzer, A. Meyer-Lindenberg, C.J. Wirth, and H. Windhagen. In vivo corrosion of four magnesium alloys and the associated bone response. *Biomaterials*, 26:3557–3563, 2005.
- [19] Y. Torres, P. Trueba, J. Pavon, I. Montealegre, and J. A. Rodriguez-Ortiz. Designing, processing and characterisation of titanium cylinders with graded porosity: An alternative to stress-shielding solutions. *Materials and Design*, 63:316–324, 2014.
- [20] S. Ramakrishna, J. Mayer, E. Wintermantel, and K. Leong. Biomedical applications of polymer-composite materials: a review. *Composites Science and Technology*, 61:1189–1224, 2001.
- [21] M. Erinc, W.H. Sillekens, R.G.T.M. Mannens, and R.J. Werkhoven. Applicability of existing magnesium alloys as biomedical implant materials. *Magnesium Technology*, pages 209–214, 2009.
- [22] S.E. Henderson, K. Verdelis, S. Maiti, S. Pal, W.L. Chung, D. Chou, P.N. Kumta, and A.J. Almarza. Magnesium alloys as a biomaterial for degradable craniofacial screws. *Acta Materialia*, 10:2323–2332, 2014.

- [23] L.M. Reis de Vasconcellos, D.O. Leite, F. Nascimento de Oliveira, Y.R. Carvalho, and C.A.A. Cairo. Evaluation of bone ingrowth into porous titanium implant: histomorphometric analysis in rabbits. *Braz. Oral. Res.*, 24:399–405, 2010.
- [24] F.E. Hauser and P.R. Landon and J.E. Dorn. Deformation and fracture mechanisms of polycrystalline magnesium at low temperatures. *Transactions of the ASM*, 48:986, 1956.
- [25] W.R. Hibbard and E.C. Burke. Plastic deformation of magnesium single crystals. *T. Metall. Soc. AIME*, 194:295, 1952.
- [26] R. Von Mises. Mechanik der plastischen Formänderung von Kristallen. *Ztschr. f. angew. Math. und Mech.*, 8:307, 1928.
- [27] B.P. Zhang, L. Geng, L.J. Huang, X.X. Zhang, and C.C. Dong. Enhanced mechanical properties in fine-grained Mg_{1.0}Zn_{0.5}Ca alloys prepared by extrusion at different temperatures. *Scripta Materialia*, 63:1024–1027, 2010.
- [28] W.J. Kim, C.W. An, Y.S. Kim, and S.I. Hong. Mechanical properties and microstructures of an AZ61 Mg alloy produced by equal channel angular pressing. *Scripta Materialia*, 47:39–44, 2002.
- [29] U.F. Kocks and H. Mecking. Kinetics of flow and strain-hardening. *Acta Metallurgica*, 29:1865–1875, 1981.
- [30] F.B. Prinz and A.S. Argon. The evolution of plastic resistance in large strain plastic flow of single phase subgrain forming metals. *Acta Metallurgica*, 32:1021–1028, 1984.
- [31] Y. Estrin, L.S. Toth, A. Molinari, and Y. Brechet. A dislocation based model for all hardening stages in large strain deformation. *Acta Materialia*, 46:5509–5522, 1998.
- [32] J. Koike, T. Kobayashi, T. Mukai, H. Watanabe, M. Suzuki, K. Maruyama, and K. Higashi. The activity of non-basal slip systems and dynamic recovery at room temperature in fine-grained AZ31B magnesium alloys. *Acta Materialia*, 51:2055–2065, 2003.
- [33] V.V. Latysh, I.P. Semenova, G.H. Salimgareeva, I.V. Kandarov, Y.T. Zhu, T.C. Lowe, and R.Z. Valiev. Microstructure and properties of Ti rods produced by multi-step SPD. *Materials Science Forum*, 503-504:763–768, 2006.
- [34] R. Xin, B. Song, K. Zeng, G. Huang, and Q. Liu. Effect of aging precipitation on mechanical anisotropy of an extruded Mg₂Y alloy. *Materials and Design*, 34:384–388, 2012.
- [35] C. Antion, P. Donnadieu, F. Perrard, A. Deschamps, C. Tassin, and A. Pisch. Hardening precipitation in a Mg₄Y₃RE alloy. *Acta Materialia*, 51:5335–5348, 2003.

- [36] G. Barucca, R. Ferragut, F. Fiori, D. Lussana, P. Mengucci, F. Moia, and G. Riontino. Formation and evolution of the hardening precipitates in a mgzyd alloy. *Acta Materialia*, 59:4151–4158, 2011.
- [37] E. Zhang, D. Yin, L. Xu, L. Yang, and K. Yang. Microstructure, mechanical and corrosion properties and biocompatibility of mgznmn alloys for biomedical application. *Materials Science and Engineering C*, 29:987–993, 2009.
- [38] P.R. Cha, H.S Han, G.F. Yang, Y.C. Kim, K.H. Hong, S.C Lee, J.Y. Jung, and H.K. Seok. Biodegradability engineering of biodegradable mg alloys: Tailoring the electrochemical properties and microstructure of constituent phases. *Scientific Reports*, 3:2367, 2013.
- [39] F. Witte, J. Fischer, J. Nellesen, C. Vogt, T. Donath, and F. Beckmann. In vivo corrosion and corrosion protection of magnesium alloy lae442. *Acta Materialia*, 6:1792–1799, 2010.
- [40] J. Kuhlmann, I. Bartsch, E. Willbold, S. Schuchardt, O. Holz, N. Hort, D. Hoche, W.R. Heineman, and F. Witte. Fast escape of hydrogen from gas cavities around corroding magnesium implants. *Acta Materialia*, 9:8714–8721, 2013.
- [41] T. Kraus, S.F. Fischerauer, A.C. Hanzi, P.J. Uggowitzer, J.F. Löffler, and A.M. Weinberg. Magnesium alloys for temporary implants in osteosynthesis: In vivo studies of their degradation and interaction with bone. *Acta Materialia*, 8:1230–1238, 2012.
- [42] J.X. Yang, Y.P Jiao, F.Z. Cui, I.S. Lee, Q.S. Yin, and Y. Zhang. Modification of degradation behavior of magnesium alloy by ibad coating of calcium phosphate. *Surface and Coatings Technology*, 202:5733–5736, 2008.
- [43] D. Orlov, K.D. Ralston, N. Birbilis, and Y. Estrin. Enhanced corrosion resistance of mg alloy zk60 after processing by integrated extrusion and equal channel angular pressing. *Acta Materialia*, 59:6176–6186, 2011.
- [44] J. Jiang and A. Ma. *Bulk ultrafine-grained magnesium alloys by SPD processing: technique, microstructure and properties*. InTech, 2011.
- [45] D. Song, A.B. Ma, J.H. Jiang, P.H. Lin, D.H. Yang, and J.F. Fan. Corrosion behaviour of bulk ultra fine grained az91d magnesium alloy fabricated by equal channel angular pressing. *Corrosion Science*, 53:362–373, 2011.
- [46] H. Hornberger, S. Virtanen, and A.R. Boccaccini. Biomedical coatings on magnesium alloys a review. *Acta Biomaterialia*, 8:2442–2455, 2012.
- [47] J. Li, Y. Song, S. Zhang, C. Zhao, F. Zhang, X. Zhang, L. Cao, Q. Fan, and T. Tang. In vitro responses of human bone marrow stromal cells to a fluoridated hydroxyapatite coated biodegradable mg-zn alloy. *Biomaterials*, 31:5782–5788, 2010.

- [48] M. Razavi, M. Fathi, O. Savabi, D. Vashae, and L. Tayebi. In vivo assessments of bioabsorbable az91 magnesium implants coated with nanostructured fluoridated hydroxyapatite by mao/epd technique for biomedical applications. *Materials Science and Engineering C*, 48:21–27, 2015.
- [49] A.K. Khanra, H.C. Jung, S.H. Yu, K.S. Hong, and K.S. Shin. Microstructure and mechanical properties of mghap composites. *Bulletin Materials Science*, 33:43–47, 2010.
- [50] B.D. Ratner. volume 9. 2012.
- [51] Z. Zhang, O. Ortiz, R. Goyal, and J. Kohn. *Chapter 13 Biodegradable polymers*. 2014.
- [52] H.M. Wong, K.W.K. Yeung, K.O. Lam, V. Tam, P.K. Chu, K.D.K. Luk, and K.M.C. Cheung. A biodegradable polymer-based coating to control the performance of magnesium alloy orthopaedic implants. *Biomaterials*, 31:2084–2096, 2010.
- [53] L. Xu and A. Yamamoto. Characteristics and cytocompatibility of biodegradable polymer film on magnesium by spin coating. *Colloids and Surfaces B: Biointerfaces*, 93:67–74, 2012.
- [54] A. Zomorodian, M.P. Garcia, T.M. Silva, J.C.S. Fernandes, M.H. Fernandes, and M.F. Montemor. Corrosion resistance of a composite polymeric coating applied on biodegradable az31 magnesium alloy. *Acta Materialia*, 9:8660–8670, 2013.
- [55] Y.M. Hwang, H.H. Hsu, and G.Y. Tzou. Study of psw rolling process using stream functions. *Journal of Materials Processing Technology*, 80:341–344, 1998.
- [56] T. Winterfeldt. Erhhung der prozesstransparenz beim planetenschrgwalzen am beispiel der kupferrohrherstellung. *Cuvillier-Verlag Göttingen*, 2008.
- [57] N.V. Lopatin and S.P. Galkin. Mathematical modeling of radial-shear rolling of the vt6 titanium alloy under conditions of formation of a globulat structure. *Russian Journal of Non-Ferrous Metals*, 52:442–447, 2011.
- [58] E.A. Kharitonov. Temperature field in blank during radial shear rolling. *Steel in Translation*, 40:12–16, 2010.
- [59] S.P. Galkin. Regulating radial-shear and screw rolling on the basis of the metal trajectory. *Steel in Translation*, 34:57–60, 2004.
- [60] C.K. Shih, C. Hung, and R.Q. Hsu. The finite element analysis on planetary rolling process. *Journal of Materials Processing Technology*, 113:115–123, 2001.
- [61] J.K. Lee, K.B. Han, K.W. Kim, J.W. Choe, J.H. Kim, and H.Y. Cho. Finite element analysis of copper tube rolling process using the planetary rolling mill. *Journal of the Korean Society of Marine Engineering*, 34:303–309, 2010.

- [62] *Standard Guide for Preparation of Metallographic Specimens*. .
- [63] G.V. Voort. *Buehler Tech-notes*, 4, 2004.
- [64] *Standard Test Methods for Determining Average Grain Size*. .
- [65] Y. Wang, A. Molotnikov, M. Diez, R. Lapovok, H.E. Kim, J.T. Wang, and Y. Estrin. Gradient structure produced by three roll planetary milling: numerical simulation and microstructural observations. *Science and Engineering A*, 639:165–172, 2015.
- [66] X. Molodova, G. Gottstein, M. Winning, and R.J. Hellmig. Thermal stability of ecap processed pure copper. *Materials Science and Engineering A*, 460-461:204–213, 2007.
- [67] K.S. Tun and M. Gupta. Improving mechanical properties of magnesium using nano-yttria reinforcement and microwave assisted powder metallurgy method. *Composites Science and Technology*, 67:2657–2664, 2007.
- [68] C.H. Caceres and J.R. Griffiths. Grain size hardening and mg-zn solid solutions. *Metallurgical and Materials Transactions*, 42A:1950–1959, 2011.
- [69] C.J. Bettles and M.A. Gibson. Current wrought magnesium alloys: strengths and weaknesses. *Journal of Metals*, pages 46–49, 2005.
- [70] H.C. Chen and T.S. Lui. Wiley-TMS, 2013.
- [71] M. Thirumurugan. Improved ductility in zm21 magnesium-aluminium macrocomposite produced by co-extrusion. *Journal of Materials Processing Technology*, 211:1637–1642, 2011.
- [72] Q. Ge. The processing of ultrafine-grained mg tubes for biodegradable stents. *Acta Materialia*, 9:8604–8610, 2013.
- [73] J. Li, W. Xu, X. Wu, H. Ding, and K. Xia. Effects of grain size on compressive behaviour in ultrafine grained pure mg processed by equal channel angular pressing at room temperature. *Materials Science and Engineering A*, 528:5993–5998, 2011.
- [74] S. Biswas. Room temperature equal channel angular extrusion of pure magnesium. *Acta Materialia*, 58:3247–3261, 2010.
- [75] T.I. Savyolova and S.F. Kourtasov. Orientation distribution function restoration by orientations grid. *Materials Science Forum*, 495-497:301–306, 2005.
- [76] A. Krause, N. Hoh, D. Bormann, C. Krause, F. Bach, H. Windhagen, and A. Meyer-Lindenberg. Degradation behaviour and mechanical properties of magnesium implants in rabbit tibiae. *J Mater Sci*, 45:624–632, 2010.

- [77] G. Ben-Hamu, D. Eliezer, K.S. Shin, and S. Cohen. The relation between microstructure and corrosion behavior of mg-y-re-zr alloys. *Journal of Alloys and Compounds*, 431:269–276, 2007.
- [78] S.R. Agnew, R.P. Mulay, F.J. Polesak, C.A. Calhoun, J.J. Bhattacharyya, and B. Clausen. In situ neutron diffraction and polycrystal plasticity modeling of a mg-y-nd-zr alloy: effects of precipitation on individual deformation mechanisms. *Acta Materialia*, 61:3769–3780, 2013.
- [79] T. Rzychon and A. Kielbus. Microstructure of we43 casting magnesium alloy. *Journal of Achievements in Materials and Manufacturing Engineering*, 21:issue 1, 2006.
- [80] N. Kumar, D. Choudhuri, R. Banerjee, and R.S. Mishra. Strength and ductility optimization of mg-y-nd-zr alloy by microstructural design. *International Journal of Plasticity*, 2014.
- [81] K.Yu, W. Li, R. Wang, B. Wang, and C. Li. Effect of t5 and t6 tempers on a hot rolled we43 magnesium alloy. *Materials Transactions*, 49:1818–1821, 2008.
- [82] S. Kandalam, P. Agrawal, G.S. Avadhani, S. Kumar, and S. Suwas. Precipitation response of the magnesium alloy we43 in strained and unstrained conditions. *Journal of Alloys and Compounds*, 623:317–323, 2015.
- [83] N. Birbilis, K. Meyer, B.C. Muddle, and S.P. Lynch. In situ measurement of corrosion on the nanoscale. *Corrosion Science*, 51:1569–1572, 2009.
- [84] S. Hiromoto and M. Tomozawa. Hydroxyapatite coating of az31 magnesium alloy by a solution treatment and its corrosion behavior in nacl solution. *Surface and Coatings Technology*, 205:4711–4719, 2011.
- [85] M. Tomozawa and S. Hiromoto. *Acta Materialia*, 59:355–363, 2011.